UNIVERSITY OF SOUTHAMPTON

FACULTY OF ENGINEERING, SCIENCE & MATHEMATICS

Optoelectronics Research Centre

Femtosecond laser writing in transparent materials

by

Weijia Yang

Thesis for the degree of Doctor of Philosophy

September 2008

UNIVERSITY OF SOUTHAMPTON

ABSTRACT

FACULTY OF ENGINEERING, SCIENCE & MATHEMATICS

OPTOELECTRONICS RESEARCH CENTRE

Doctor of Philosophy

Femtosecond laser writing in transparent materials

by Weijia Yang

Optical waveguides (type-I), with perfect mode matching to the standard single-mode fibre and with an overall insertion loss of ~1 dB, have been demonstrated in high index bismuth borate glass by femtosecond laser direct writing. Broadening of the transmitted light source by as much as 500 nm was demonstrated through a waveguide with a length of 1.8 cm. Finally, passive waveguide components such as Y-splitters and directional couplers have also been fabricated using this writing technique.

Self-assembled, sub-wavelength periodic structures (type-II) are induced in fused silica by a tightly focused, linearly polarized, femtosecond laser beam. Two different types of periodic structures, the main one with period (Λ_E) in the direction of the laser beam polarization and the second with period (Λ_k) in the direction of the light propagation, are identified from the cross-sectional images of the modified regions using scanning electron microscopy. The period Λ_E is proportional to the wavelength of the writing laser and the period Λ_k in the head of the modified region remains approximately the wavelength of light in fused silica.

A new phenomenon in ultrafast laser processing of transparent optical materials, in particular silica glass, manifested as a change in material modification by reversing the writing direction, is observed. The effect resembles writing with a quill pen and is interpreted in terms of new physical effect - anisotropic trapping of electron plasma by a tilted front of the ultrashort laser pulse. Different types of modifications are induced in fused silica by controlling the pulse front tilt.

Birefringent modification is demonstrated in the chalcogenide glass by femtosecond laser direct writing. The optical axis of the birefringent region is not determined by the laser polarization direction. It is observed that the information on the direction of writing can be recorded and be rewritable in the chalcogenide glass.

Finally, a unique non-reciprocal photosensitivity is identified for the lithium niobate crystal for ultrafast laser direct writing. Therefore, in a non-centrosymmetric medium, modification of the material can be different when light propagates in opposite directions.

Contents

Declaration of authorship

I, Weijia Yang
declare that the thesis entitled
Femtosecond laser writing in transparent materials
and the work presented in the thesis are both my own, and have been generated by me as the result of my own original research. I confirm that:

- this work was done wholly or mainly while in candidature for a research degree at this University;
- where any part of this thesis has previously been submitted for a degree or any other qualification at this University or any other institution, this has been clearly stated;
- where I have consulted the published work of others, this is always clearly attributed;
- where I have quoted from the work of others, the source is always given. With the exception of such quotations, this thesis is entirely my own work;
- I have acknowledged all main sources of help;
- where the thesis is based on work done by myself jointly with others, I have made clear exactly what was done by others and what I have contributed myself;
- parts of this work have been published (See *List of Publication*)

Weijia Yang

September 2008

Nomenclature

Symbols

B	Magnetic flux density
D	Electric flux density
E	Electric field
H	Magnetic field
P	Induced polarization

γ	Keldysh parameter
ε_0	Electric permittivity in free space
μ_0	Magnetic permeability in free space
E_g	Bandgap energy of the material
n	Refractive index
n_0	Linear refractive index
n_2	Nonlinear refractive index
I	Laser intensity
P_{cr}	Critical power for the self focousing
ϕ	Phase
ω_0	Angular frequency
ω_p	Plasma frequency
σ_m	Multiphoton absorption coefficient
E	Amplitude of the laser electric field
N_e	Electron density
N_{cr}	Critical plasma density
w_0	Spatial radius of the Gaussian intensity beam profile at $1/e^2$
e	Charge of the electron
E_p	Pulse energy
V	Normalized frequency of the waveguide
Δn	Refractive index change
n_{eff}	Effective refractive index of the waveguide
α	Propagation loss of the waveguide
Λ_E	Period of the nanograting along the polarization of the laser beam
Λ_k	Period of the nanograting along the laser propagation direction
κ	Thermal conductivity
D	Thermal diffusivity
c_p	Heat capacity
ρ	Mass density
f	Pulse repetition rate
L_D	Thermal diffusion length
T	Temperature
J	Heat current

Acronyms

LC	Liquid crystal
CW	Continuous wave
DIC	Differential interference contrast
SEM	Scanning electron microscopy
FWHM	Full width half maximum
GVD	Group velocity dispersion
IR	Infrared
NA	Numerical aperture
OSA	Optical spectrum analyser
QPM	Quantitative phase microscopy
SPM	Self phase modulation
UV	Ultraviolet
BZH7	Bismuth borate glass sample
CCD	Charged coupled device
MPI	Multiphoton ionization
MFD	Mode field diameter
BPM	Beam propagation method

List of figures

List of tables

Acknowledgements

Now that my student days are coming to an end, I would like to thank everyone who helped me throughout my thesis work. In particular I would like to thank my supervisor Prof. Peter Kazansky for his technical support and guidance and for showing me the discipline needed to be a dedicated scientist.

I would also like to thank the excellent team members I have worked with over the years. I thank Dr. Erica Bricchi, the most important person in my initial stage of PhD study, who dedicated an enormous amount of time and effort guiding me into the ultrafast field and assisting me in setting up the laser processing lab. I thank Dr. Costantino Corbari for assisting me in the waveguide poling and many inspiring discussions. I thank Dr. Alan Arai and his team in IMRA America for sharing their ultrafast fibre laser system and processing the fused silica. I thank Dr. Yauhiko Shimotsuma for his measurement of pulse front tilt. I thank Prof. Yuri Svirko for his help in lithium niobate tensor calculation. I thank Dr. Ryota Kitagawa for providing me with the chalcogenide sample. I thank Prof. Bertrand Poumellec and Dr. Matthieu Lancry for giving me the opportunity to visit their lab and allowing me to further my career in academia.

I am sincerely grateful to Eve for her great help in my student journey and to Eleanor for proofreading the thesis. I would like to thank all the students in our group: Steve (Dr. now) and Albert for the memorable lab time.

I would like to thank all my friends and office mates (Fei, Zhaowei, Hughes, Kangkang, just to mention a few) for their kindness and friendship, which makes my PhD life more enjoyable. Yang Gao, thank you for your love, patience, understanding and encouragement during the most difficult stage of my PhD venture. Finally I would like to thank my parents for their support. It is hard to imagine having made it to this point without them.

Chapter 1

Introduction

1.1 Motivation and aims

Since the invention of the laser in 1960 [1], this new form of light has attracted enormous interest because its relevance to a wide range of applications in science and technology including laser spectroscopy, laser medicine and laser material processing. More recently, lasers with pulse duration in the femtosecond regime have been demonstrated [2]. The ultrashort pulse lasers open new frontiers in ultrafast optics and spawn research groups around the world. Ultrashort pulse lasers have two main advantages compared to the conventional lasers. First, the ultrashort pulse duration enables a measurement with extremely short temporal resolution on a femtosecond scale. Dynamic studies of chemical reactions in gases and charge carriers in semiconductor have been carried out using ultrashort pulse lasers [3, 4]. Second, the focused ultrashort pulses can produce extremely high intensity enabling new frontiers in the physics and technology of light-matter interactions ranging from table-top ultrafast x-ray generation and filament propagation in air to super-continuum generation and ultrafast laser material processing [5-9]. The work presented in this thesis will mainly focus on the study of femtosecond laser interaction with transparent materials. For the most of the available commercial femtosecond laser system, the intensity at the focus can reach 10^{13} W/cm^2 when the laser is tightly focused inside the transparent material. As a result, nearly any materials including wide band-gap insulator, such as sapphires and fused silica, can be easily ionized through nonlinear absorption, resulting in optically induced breakdown. Moreover, during the laser material processing, the absorbed pulse energy only can transfer to the lattice on the order of 10 ps. As a result, in contrast to the material modification using nanosecond or longer laser pulses where the processing is dominated by the thermal effect, for the

femtosecond laser interaction with the materials, a very clean modified region with minimum collateral damage and heat affected zone can be induced making it a promising technique for high precision micro-structuring materials. Furthermore, the nonlinear absorption process enables induced modification to be confined in the focal volume where the local intensity is higher than the threshold for modification. The transparent material can be bulk modified in a three dimensional manner, by simply moving the transparent material relevant to the focal spot of the laser beam.

Depending on the focusing position of the laser beam, surface patterning or bulk modification could be realized in transparent materials using focused femtosecond laser irradiation. In this thesis, we will mainly study the latter case where the laser beam is focused inside the bulk transparent material. The first demonstration of micro-modification inside bulk glasses using femtosecond laser pulses occurred in 1996 by Hirao group where optical waveguides have been fabricated [8]. In the same year, Mazur group demonstrated the ability to modify the refractive index of sub-micrometer sized volumes inside the transparent material providing a new method for three-dimensional data storage [9]. Since then, significant attention has been drawn to the study of modification of materials with ultrashort laser pulses which generates a wide range of applications including laser surgery [10], integrated optics [8, 11-31], optical data storage [9, 32-34] and three dimensional micro- and nanostructuring [35-66]. Moreover, depending on the exposure parameters and material property, three qualitatively different kinds of structural changes can be induced inside transparent materials: an isotropic refractive index change mainly used for the waveguide inscription [8] (type-I); a form birefringence with negative index change enabling the realization of retardation plates [39] (type-II); and a void suitable for the application of data storage [34] (type-III). Despite the promise of ultrashort laser pulses in processing transparent material for a variety of applications, the mechanism of inducing different structural changes in transparent materials is still not fully understood.

It is with this background that our investigations in the field of femtosecond laser interaction with transparent materials began. The main objective of this thesis is to

explore novel applications using femtosecond laser direct writing technique and to gain further knowledge of the fundamental light-material interactions.

Waveguide writing is one of the most important application for the femtosecond laser induced type-I modification. There are only few reports on the femtosecond laser direct writing in high index glasses such as SF57, chalcogenide and heavy metal oxide glasses having $n_0 > 1.8$ and $n_2 > 10^{-15}$ cm^2/W [18, 27, 46, 67]. Bismuth borate glass possesses a large n_2 value (5×10^{-15} cm^2/W at 1064 nm) which is almost 20 times higher than the nonlinear refractive index of silica glass [68]. This makes it an excellent candidate material for the fabrication of nonlinear optical devices such as optical switches or supercontinuum generators. Moreover, thermal poling can induce high second-order nonlinearity in bismuth borate glass [69], which can be used for fabricating nonlinear optical devices such as frequency converters or electro-optic modulators [24]. Despite these advantages, the implementation of passive waveguide components in bismuth borate glass using femtosecond laser direct writing is still unexploited. In this thesis, type-I modification was firstly demonstrated in high index bismuth borate glass using femtosecond laser direct writing. Low loss waveguides and passive waveguide components were also fabricated.

Recently, femtosecond laser induced type-II modifications characterized by birefringence, anisotropic reflection and negative change, have attracted increasing interests [36-38, 48]. The self-assembled periodic nanostructures, which have a size as low as 20 nm and formed in the focal volume of the fused silica, justified all the phenomena observe for this type of modification. Micro-reflectors, rewritable data storage and micro-fluidic channels have been demonstrated using these nanostructures [37, 38, 48, 54, 55]. Despite the varieties of applications, there is still lack of characterization of their properties on various fabrication parameters, which are essential to enable a better understanding of the mechanisms responsible for the formation of the nanostructures, and consequently how to efficiently exploit them. In this thesis, Type-II modification in fused silica was studied using variable repetition rate femtosecond fiber laser system at two different wavelengths. A two dimensional periodicity, one along the polarization of light and one with the value of laser wavelength along the light propagation direction, was identified. In addition, a

quantitative analysis the dependence of the nanogratings period as a function of laser parameters was completed. Moreover, it was demonstrated that the range of effective pulse energy which could produce nanogratings narrows when the pulse repetition rate of writing laser increases

Generally, the femtosecond laser induced modifications depend on the exposure parameters (wavelength, pulse duration, repetition rate, pulse energy) and material property (bandgap, thermal diffusivity). Here, a new phenomenon in ultrafast laser processing of transparent optical materials, in particular silica glass, manifested as a change in material modification by reversing the writing direction was observed. The tilt of pulse front was utilized as a new parameter to control the structural modification.

Birefringent modification is induced in the chalcogenide glass by femtosecond laser direct writing. Unlike the previously reported photoinduced anisotropy in chalcogenide glass [70, 71] and form birefringence in fused silica [39, 40], the optical axes of the birefringent region are not determined by the polarization direction of the irradiating light. Instead, by varying the scanning direction of the laser irradiation, the optical axes of the birefringence can be changed. As a result, the information on the direction of writing could be recorded inside transparent materials. Moreover, this type of photoinduced anisotropy can be erased by annealing, and is reversible by repeatable scanning.

Finally, a unique non-reciprocal photosensitivity was identified for the lithium niobate crystal for ultrafast laser direct writing. It was demonstrated that when the direction of the femtosecond laser beam is reversed from +Z to – Z directions, the structures written in lithium niobate crystal when translating the beam along the +Y and –Y directions are mirrored. Therefore in a non-centrosymmetric medium modification of the material can be different when light propagates in opposite directions.

1.2 Thesis Overview

In chapter two: This chapter provides an introduction to the basic nonlinear propagation and ionization mechanisms that governing the interaction of ultrashort pulse with transparent materials.

In chapter three: The experimental setup for the femtosecond laser material processing was introduced. Quantitative phase and birefringence technique for characterizing the sample after irradiation has also been discussed.

In chapter four: This chapter presents results of positive refractive index modification (type-I) in high index bismuth-borate glass by femtosecond laser irradiation. A specific set of writing parameters leading to waveguides perfectly mode matched to standard single-mode fibers at 1.55 μm with an overall insertion loss of ~1 dB and with propagation loss below 0.2 dB/cm was identified. Passive waveguide components such as Y-splitters and directional couplers have also been demonstrated. Finally, the nonlinear refractive index of the waveguides has been measured to be 6.6 $\times 10^{-15}$ cm^2/W by analyzing self-phase modulation of the propagating femtosecond laser pulse at the wavelength of 1.46 μm. Broadening of the transmitted light source as large as 500 nm was demonstrated through a waveguide with the length of 1.8 cm.

In chapter five: This chapter presents results of induced form birefringence (type-II) in fused silica by femtosecond direct writing. Self-assembled, sub-wavelength periodic structures are induced in fused silica by a tightly focused, linearly polarized, femtosecond laser beam. Two different types of periodic structures, the main one with period (Λ_E) in the direction of the laser beam polarization and the second with period (Λ_k) in the direction of the light propagation, are identified from the cross-sectional images of the modified regions using scanning electron microscopy. We demonstrate the spatial coherence of these nanogratings in the plane perpendicular to the beam propagation direction. The range of effective pulse energy which could produce nanogratings narrows when the pulse repetition rate of writing laser increases. The period Λ_E is proportional to the wavelength of the writing laser and period Λ_k in the

head of the modified region remains approximately the wavelength of light in fused silica.

In chapter six: A new phenomenon was discovered in ultrafast laser processing with transparent optical materials, manifested as a change in material modification by reversing the writing direction. The effect resembles writing with a quill pen and is interpreted in terms of new physical effect - anisotropic trapping of the electron plasma by a tilted front of the ultrashort laser pulse. Different types of ultrafast laser induced modifications were demonstrated inside fused silica by varying the direction of pulse front tilt.

In chapter seven: Birefringence is induced by femtosecond laser direct writing inside chalcogenide glass. The optical axes of the birefringent region are not determined by the polarization direction of the irradiating light. Instead, the direction of the optical axis is defined by the laser scanning direction and the birefringence is produced by stress which was induced by thermal expansion of the glass during laser irradiation. Moreover, the polarization of light, passing through the modified region, rotates in opposite directions on the two sides from the centre of the region, which was produced by the twist of optical axis along the light propagation direction. Furthermore, it is observed that the information on the direction of writing could be recorded and be rewritable inside transparent materials.

In chapter eight: It has been a common belief that in a homogeneous medium, the photosensitivity and corresponding light-induced material modifications do not change on the reversal of light propagation direction. Here we demonstrate that when the direction of the femtosecond laser beam is reversed from +Z to – Z directions, the structures written in lithium niobate crystal when translating the beam along the +Y and –Y directions are mirrored. Therefore in a non-centrosymmetric medium modification of the material can be different when light propagates in opposite directions.

In chapter nine: This chapter concludes the thesis by summarizing the key findings and gives an outlook on future research and application directions.

Chapter 2

Background

In this chapter, the equations describing the nonlinear propagation of ultrashort laser pulse in transparent material are first reviewed in Section 2.1. Section 2.2 gives a brief overview of the nonlinear ionization mechanism involved during the laser material interaction process.

2.1 Ultrashort laser pulses in transparent material

The propagation of an electromagnetic wave in a nonmagnetic medium, where there are no electric charges or currents, is governed by the Maxwell equations:

$$\nabla \times \mathbf{E}(\mathbf{r},t) = -\frac{\partial \mathbf{B}(\mathbf{r},t)}{\partial t} \tag{2.1}$$

$$\nabla \times \mathbf{H}(\mathbf{r},t) = \frac{\partial \mathbf{D}(\mathbf{r},t)}{\partial t} \tag{2.2}$$

$$\nabla \cdot \mathbf{D}(\mathbf{r},t) = 0 \tag{2.3}$$

$$\nabla \cdot \mathbf{B}(\mathbf{r},t) = 0 \tag{2.4}$$

with

$$\mathbf{D}(\mathbf{r},t) = \varepsilon_0 \mathbf{E}(\mathbf{r},t) + \mathbf{P}(\mathbf{r},t) \tag{2.5}$$

$$\mathbf{B}(\mathbf{r},t) = \mu_0 \mathbf{H}(\mathbf{r},t) \tag{2.6}$$

where **E** and **H** are the electric and magnetic fields, respectively; **D** and **B** are the corresponding electric flux density and magnetic flux density; ε_0 and μ_0 are the electric permittivity and magnetic permeability in free space, and **P** is the induced

polarization. By solving the Maxwell equations, the wave equation that describes the light propagation in a homogeneous and isotropic medium becomes:

$$\nabla^2\mathbf{E}+\frac{1}{c^2}\frac{\partial^2\mathbf{E}}{\partial t^2}=-\mu_0\frac{\partial^2\mathbf{P}}{\partial t^2} \tag{2.7}$$

where $c=\sqrt{\frac{1}{\varepsilon_0\mu_0}}$, and c is the speed of light in vacuum. In conventional optics when the electric field strength is small, the polarization vector **P** is a linear function of **E**

$$\mathbf{P}(\mathbf{r},t)=\varepsilon_0\chi^{(1)}\mathbf{E}(\mathbf{r},t) \tag{2.8}$$

where $\chi^{(1)}$ is the first order susceptibility tensor and we have taken the material response to be instantaneous. For an isotropic medium, the linear susceptibility is defined as the scalar quantity $\chi^{(1)}$. This further simplifies equation (2.7)

$$\nabla^2\mathbf{E}+\frac{n_0^2}{c^2}\frac{\partial^2\mathbf{E}}{\partial t^2}=0 \tag{2.9}$$

where n_0 is the linear refractive index

$$n_0=\sqrt{1+\chi^{(1)}} \tag{2.10}$$

The linear relation between **P** and **E** in equation is only an approximation. At high field strengths, it is no longer valid. The dependence of the polarization on the field becomes nonlinear and is generally described as a power series of the electric field:

$$\mathbf{P}=\varepsilon_0(\chi^{(1)}\mathbf{E}+\chi^{(2)}\mathbf{EE}+\chi^{(3)}\mathbf{EEE}+\ldots)\equiv\left[\mathbf{P}^{(1)}+\mathbf{P}^{(2)}+\mathbf{P}^{(3)}+\cdots\right] \tag{2.11}$$

where $\chi^{(j)}$ (j = 1,2,…) is the j^{th} order susceptibility, and $\mathbf{P}^{(j)}$ is the j^{th} order polarization. Generally, the orders over the 3rd in (2.11) are negligible. Moreover, in a material with an inversion symmetry, $\chi^{(2)}=0$, as a result (2.11) becomes:

$$\mathbf{P}=\mathbf{P}^{(1)}+\mathbf{P}^{(3)}=\varepsilon_0(\chi^{(1)}+\frac{3}{4}\chi^{(3)}|\mathbf{E}|^2)\mathbf{E} \tag{2.12}$$

hence (2.12) can be simplified to:

$$\nabla^2 \mathbf{E} + \frac{n^2}{c^2}\frac{\partial^2 \mathbf{E}}{\partial t^2} = 0 \tag{2.13}$$

The refractive index n can be given as:

$$n = \sqrt{1 + \chi^{(1)} + \frac{3}{4}\chi^{(3)}|\mathbf{E}|^2} \approx n_0 + n_2 I \tag{2.14}$$

where $n_2 = \frac{3\chi^{(3)}}{4\varepsilon_0 c n_0^2}$ is the nonlinear refractive index and $I = \frac{1}{2}\varepsilon_0 c n_0 |\mathbf{E}|^2$ is the laser intensity. This nonlinear refractive index gives rise to self-focusing and self-phase modulation when the ultrashort pulses propagate through the medium.

2.1.1 Self-focusing

Self-focusing of light is a result of refractive index variation due to the spatial distribution of the intensity profile. As shown in Fig. 2.1, when an optical pulse with a Gaussian shaped spatial profile propagates through a glass plate, the intensity profile produces a Gaussian transverse refractive index distribution. The material at the center of the laser beam will have a large refractive index. As a result, the material is turned into a positive lens and focuses the incident laser beam.

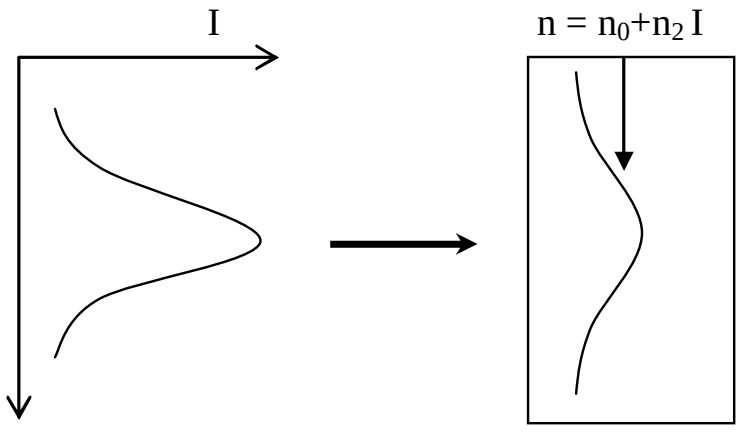

Figure 2.1: The relation between an intense laser beam with a Gaussian spatial profile and a nonlinear index of refraction in the material.

Although the refractive index change depends on the laser intensity, the strength of the self-focusing effect depends only on the peak power of the laser pulse [72]. As the power of the laser pulses increased to some critical power, filament is formed in which the self-focusing balances diffraction. The critical power P_{cr} was given as [72]:

$$p_{cr} = \frac{\pi(0.61)^2 \lambda_0^2}{8 n_0 n_2} \tag{2.15}$$

where λ_0 is the vacuum wavelength of the laser radiation. In fused silica, n_2 is 3.2 × 10^{-16} cm^2/w and n_0 is 1.47, so that P_{cr} is calculated to be 2 MW. For a laser pulse with 150 fs duration, this threshold is corresponding to pulse energy of 0.3 μJ. If the peak power of the laser pulse exceeds this critical power, then catastrophic collapse of the laser beam could happen [72]. In reality, the free electron plasma created as a result of nonlinear ionization contributes a negative refractive index change which prevents further self-focusing [73].

2.1.2 Self-phase modulation

Self-phase modulation is the counterpart of self-focusing in the time domain. Considering an optical pulse propagating through a glass plate with the length L, the phase $\phi(t)$ is given by:

$$\phi(t) = n\frac{\omega_0}{c}L - \omega_0 t = \left(n_0 + n_2 I(t)\right)\frac{\omega_0 L}{c} - \omega_0 t \tag{2.16}$$

where ω_0 is the carrier frequency. If the linear dispersion is negligible, the instantaneous frequency $\omega(t)$ then has the form:

$$\omega(t) = -\frac{\partial\phi(t)}{\partial t} = \omega_0 - \frac{n_2\omega_0 L}{c}\frac{\partial I(t)}{\partial t} \tag{2.17}$$

As a result, the leading edge of the pulse shifts to lower frequency (red) while the trailing edge shift to the higher frequency (blue). The spectrum of the laser pulse broadens with the propagation distance.

2.2 Femtosecond laser induced optical breakdown

In dielectrics, electrons are strongly bound to the lattice and the minimum energy needed to free electrons from the valence band (binding of 9 eV for fused silica) is well above the single photon energy of the near-infrared light source. (800 nm, 1.55 eV). As a result, the infrared light can not be absorbed. However, when the incident laser intensity is high enough, the nonlinear absorption become possible allowing the transparent material to be modified by light. The mechanism of ultrashort laser pulse modification of transparent materials can be divided into two parts: absorption of laser energy by the materials through nonlinear ionization and the subsequent dissipation of the absorbed energy. The nonlinear absorption takes place through three steps: production of initial seed electrons through nonlinear photoionization; followed by avalanche photoionization and finally the plasma formation. In this section, we first review three ionization processes that can take place during optical breakdown: multiphoton absorption, tunneling, and avalanche ionization. A discussion of material modification due to laser induced ionization and plasma generation in transparent materials will also be presented.

For optical breakdown and material damage to occur in transparent material, a nonlinear absorption mechanism must deposit laser energy in to the material by promoting electrons from valence band to the conduction band. There are two classes of nonlinear mechanisms that play a role in this absorption, photoionization and avalanche ionization.

2.2.1 Photoionization

Photoionizaton refers to direct excitation of the electron by the laser field. Depending on the laser frequency and intensity, there are two different regimes of photoionization, the multiphoton ionization (MPI) and tunneling ionization [74]. In MPI regime, the electron density N_e grows as:

$$\left(\frac{dN_e}{dt}\right)_{MPI} = \sigma_m I^m \tag{2.18}$$

where σ_m is the multiphoton absorption coefficient for *m*-photons absorption. The number of photons required is determined by the smallest *m* which satisfies the relation: $m\hbar\omega \geq E_g$, where E_g is the bandgap energy of the dielectric material and $\hbar\omega$ is the photon energy. Typically, *m* is ~ 6 for fused silica with 800 nm wavelength, which shows the high intensity sensitivity of this nonlinear process. In tunneling regime, the Coulomb potential is suppressed by the strong incident field allowing valence electrons to tunnel to the conduction band. Keldysh showed that both multiphoton and tunneling regimes could be described with the same framework [75]. The transition from multiphoton to tunneling ionization is characterized by the Keldysh parameter γ defined as:

$$\gamma = \frac{\omega(2m^* E_g)^{\frac{1}{2}}}{eE} \tag{2.19}$$

where *E* is the amplitude of the laser electric field oscillating at frequency ω, m^* and *e* are the effective mass and charge of the electron. When γ is much larger (smaller) than 1, multiphoton (tunneling) ionization dominates the excitation process. In the intermediate regime, the photoionization is a mixture between tunneling and multiphoton ionization. In fused silica (E_g = 9 eV), $\gamma = 1$ for a laser intensity $I = 7.5\times10^{13}$ W/cm^2 at the wavelength of 800 nm. The laser intensity reaches this value at the focus for a pulse energy of 1.4 μJ in our laser processing setup.

2.2.2 Avalanche ionization

Avalanche ionization involves free-carrier absorption followed by impact ionization (Fig. 2.2). Multiphoton and tunneling ionization provide the initial free electrons for the avalanche process that follows. Once the free electrons have been created, they can gain energy by absorbing photons through inverse bremsstrahlung. As the energy of an electron exceeding the minimum conduction band by more than the band gap energy, it can ionize another electron from valence band, resulting two excited electrons at the minimum conduction band [76]. For avalanche ionization, the conduction band electron density grows as:

$$\left(\frac{dN_e}{dt}\right)_{avalan} = \alpha I N_e \tag{2.20}$$

where α is the avalanche ionization coefficient.

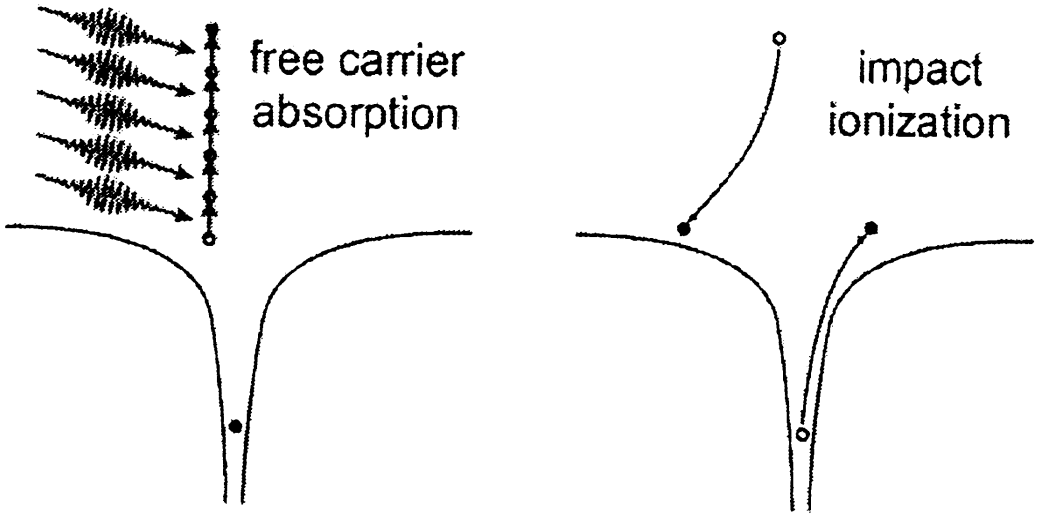

Figure 2.2: Schematic diagram of avalanche ionization [74].

2.2.3 Plasma formation:

Seeded by nonlinear photoionization, the density of electrons in the conduction band grows through avalanche ionization until the plasma frequency approaches the frequency of the incident laser radiation (the critical plasma density). Since the plasma frequency is defined as:

$$\omega_p = \sqrt{\frac{N_e e^2}{\varepsilon_0 m_{opt}}} \tag{2.21}$$

the critical plasma density equals:

$$N_{cr} = \frac{\omega_0^2 \varepsilon_0 m_{opt}}{e^2} \tag{2.22}$$

This high density plasma strongly absorbs laser energy by free-carrier absorption. Only after the laser pulse is gone is energy transferred from the electrons to the lattice. This shock like deposition of energy, on a time scale much shorter than the thermal

diffusion time, leads to ablation of material on the surface or permanent structural change in the bulk. Moreover, the plasma can modify the real part of the refractive index according to:

$$n = n_0 - \frac{N}{2n_0 N_{cr}} \tag{2.23}$$

For a Gaussian beam, the plasma induced refractive index modification has the smallest value in the beam axis. As a result, the beam is defocused by the plasma, which acts as a diverging lens. A balance between self-focusing and plasma defocusing leads to filamentary propagation.

Chapter 3

Experimental setup and analysis tools

In this chapter, the setup utilized for femtosecond laser material processing is described in Section 3.1. The rest of the chapter illustrates the optical characterization techniques for analyzing the laser induced modifications: quantitative phase microscopy for measuring the change of the refractive index and quantitative birefringence microscopy for birefringence measurement.

3.1 Direct writing setup

The experiment setup for the femtosecond laser direct writing process consists of a radiation source, the beam delivering system and the three-axis stage. The laser beam used for the most of the work was extracted from a Coherent laser system comprising of a mode locked Ti:Sapphire oscillator (“Mira”) and a regenerative amplifier (“RegA”) seeded by the output of the “Mira”. The “Mira” and “RegA” were pumped by frequency diode pumped 10 W and 12 W lasers respectively. A train of pulses with 150 fs pulse duration, at a repetition rate of 250 kHz, and at a central wavelength of 800 nm, were used in the experiment. The temporal duration of the laser beam from the RegA output was monitored using an autocorrelator. The linearly polarized laser beam passing through a collimated telescope was tightly focused into the bulk of the sample, by a 50X (NA = 0.55) microscope objective, down to a focal spot of ~ 1.5 μm. The laser polarization was controlled using a half-wave plate and the pulse energy was varied using a neutral density filter. A computer controlled shutter was used for regulating the laser exposure time. The sample was mounted on a computer controlled, three-axis, linear motorized stage (Aerotech ALS-130).

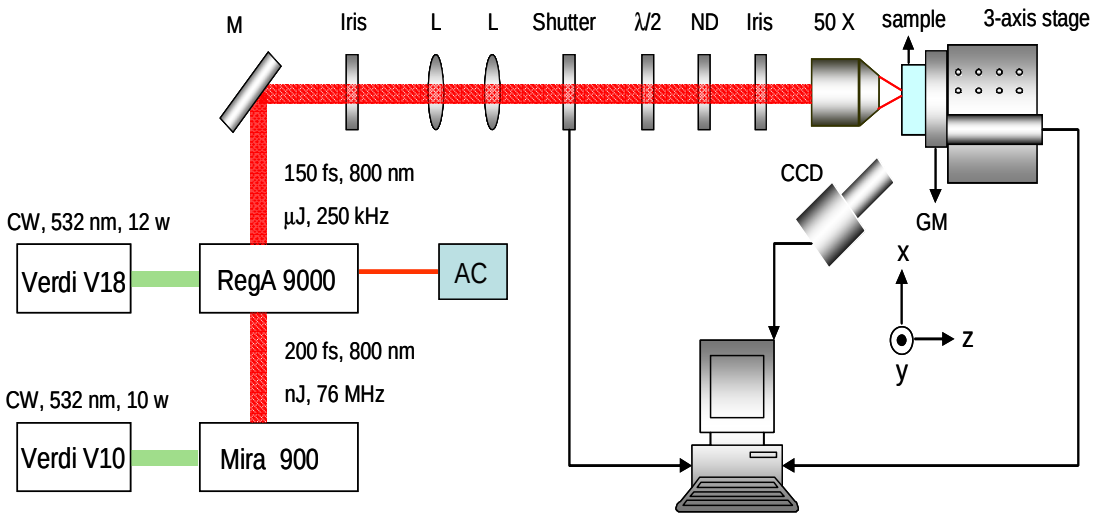

Figure 3.1: Schematic of direct writing setup. M: metallic mirror, L: lens, ND: neutral density filter, λ/2: half-wave plate, CCD: charge coupled device and AC: autocorrelator.

The stage was carefully tuned for various loading weight before the writing process. The resolution is 20 nm and the repeatability is 120 nm for all three axes of the stage. A home written HP-VEE program was applied to control the stage movement. The desired patterns of modifications were realized in the bulk material by moving the stage, while the laser was irradiating the sample with the shutter open. A CCD camera with high magnification was used to control the focal depth inside the sample and to monitor the writing process. To ensure that the input surface of the sample was perpendicular to the direction of propagation of the writing laser, two goniometers were utilized to mount the sample allowing tilting in the xz and yz planes respectively. The goniometers were adjusted until the reflections of the sample were positioned in the centre of the iris when the objective was temporally removed from the setup (Fig. 3.1). This critical alignment could also be confirmed by irradiating an ablation line on the sample surface when the focus point was near the surface within a few microns. A uniform ablation line would appear on the sample surface, across the edges, when its surface was perfectly perpendicular to the propagation direction of the writing laser.

Based on the translation direction of the stage, with respect to the laser propagation direction, there are normally two different writing geometries: a transverse writing geometry in which the sample is translated perpendicularly to the beam propagation direction and a longitudinal writing geometry in which the sample is translated along the beam propagation direction. In this thesis, the transverse writing geometry is used

since it provides much greater flexibility and allows us to write waveguides or patterned structures of arbitrary length. In contrast, for a longitudinal writing geometry, the length of the structural modification is limited by the focal length of the focusing objective. The transverse writing geometry results in an intrinsic asymmetry of the structure cross section (zy plane). This is mainly due to the fact that: along the propagation direction of the laser, the size Δz is determined by the confocal parameter $2\pi w_0^2 / \lambda$ (where w_0 is the beam waist), while perpendicular to the laser propagation direction, the size Δy is determined by the focal diameter $2w_0$. Several techniques, including the astigmatic cylindrical telescope [77], multiple scan [25], deformable mirrors [78] and slit beam shaping methods [21] have been used to overcome this problem.

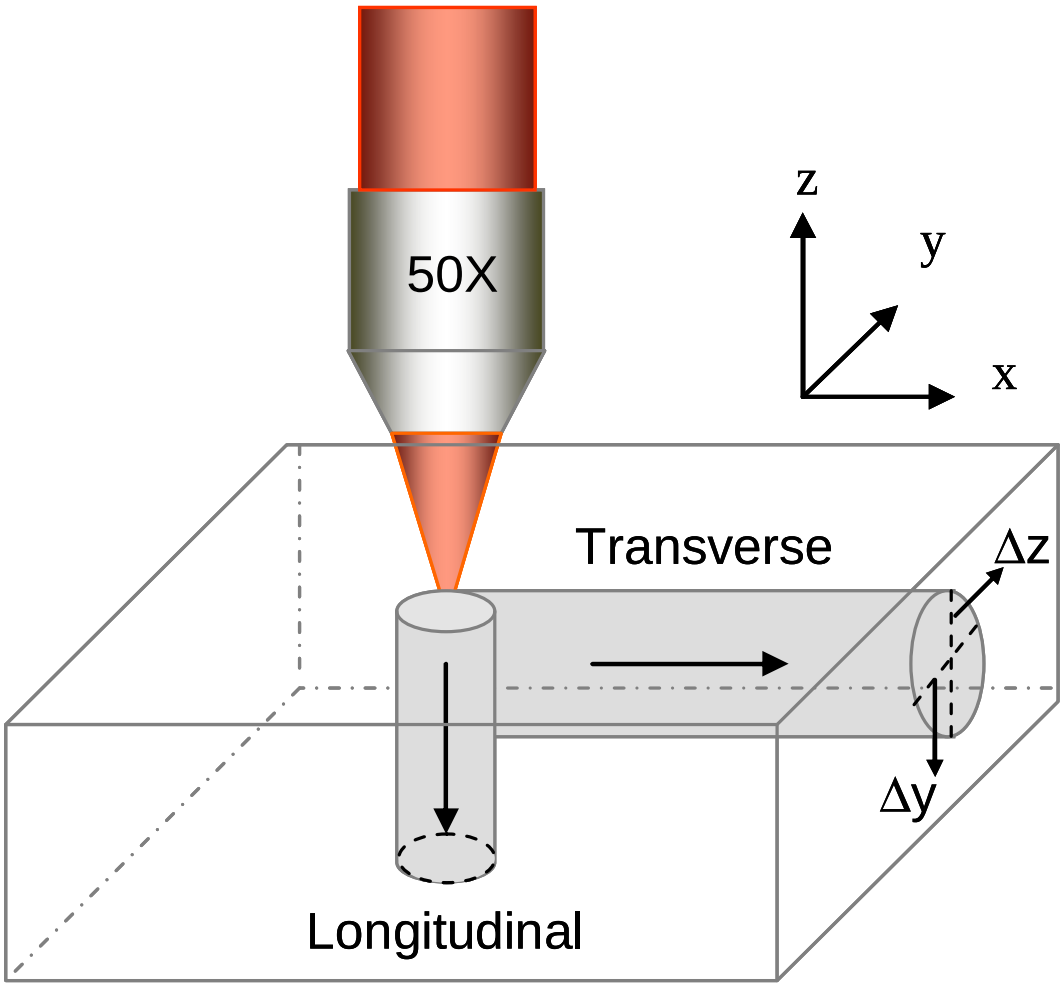

Figure 3.2: Longitudinal and transverse writing geometries for femtosecond laser direct writing.

3.2 Optical Characterization

After femtosecond laser irradiation, the sample was inspected using an optical microscope (Olympus BX-51). Optical properties, including laser induced refractive index modification and birefringence, were characterized using quantitative phase and birefringence imaging techniques.

3.2.1 Quantitative phase microscopy

Depending on the laser parameters and material properties, three types of modifications have been induced in the bulk of the material by femtosecond laser direct writing. The fundamental characteristic of these modifications can obtained from the quantitative information of refractive index profile of the focal region after laser irradiation. There have been several methods in the literature for measuring the refractive index profile of the structures embedded inside the transparent materials [79-83]. Their summary is listed in Table 3.1.

Techniques	Spatial resolution	Sensitivity	Disadvantages
Refractive near-field profiling [79]	Sub-micrometer	On the order of 10^{-4}	Expensive equipment, strict requirement for detector sensitivity and calibration from reference samples
Phase-stepping interferometry [80]	micrometer	On the order of 10^{-4}	Home-made setup, difficult to alignment
Digital holography Microscopy [81]	micrometer	On the order of 10^{-4}	Expensive equipment
Near-field scanning optical microscopy [82]	nanometer	10^{-5}	Expensive equipment, very hard to setup
Quantitative phase microscopy [83]	micrometer	On the order of 10^{-4}	Expensive software

Table 3.1: Various techniques used to measure the refractive index profile of femtosecond laser induced modifications.

A non-interferometric solution: quantitative phase microscopy (QPM) [84] was utilized here to analyze the refractive index profile of the focal region after modification. By using an optical microscope (Olympus BX-51) in transmission mode, a set of images: one in-focus (I_0) and two very slightly positively/negatively (I_+/I-) defocused images were firstly captured by the CCD camera (Fig. 3.3). The images were then converted into intensity data using the computer. It is now well established that the propagation of light field along the optical axis z in microscope obeys the transport of intensity equation [83]:

$$\frac{2\pi}{\lambda}\frac{\partial I(\vec{r})}{\partial z} = -\nabla.\left(I(\vec{\mathrm{r}})\nabla\phi\left(\frac{\vec{\mathrm{r}}}{M}\right)\right) \tag{3.1}$$

where $\vec{\mathrm{r}}$ = (x, y) is a two dimensional vector in the transverse plane, I is the intensity distribution of the image and M is the magnification of the microscope. The differential information of the propagation of the field on the left hand side of the Equation 3.1 can be obtained from:

$$\frac{\partial I(\vec{r})}{\partial z} \approx \frac{I_+ - I_-}{2\Delta z} \tag{3.2}$$

where Δz is the defocus distance. Given this information and the intensity information of the in focus image, the Equation 3.1 can be solved using an appropriate algorithm [84]. This analysis is based on coherent illumination; however, the optical microscopes used in QPM systems have a partially coherent illumination source. It can be shown [84] that a partially coherent source gives an identical result to the coherent case, in Equation 3.1, provided that the irradiance distribution of the illumination source shows inversion symmetry. The de-focused images were obtained by translating the objective using a motorized stage (Physik Instrumente). Both the image acquisition and the algorithm for phase map calculation in the QPM system are from IATIA Ltd. The refractive index change of the modified region can then be calculated using Equation 3.3:

$$\Delta n = \frac{\Delta\phi\lambda}{2\pi d} \tag{3.3}$$

where λ is the wavelength of 550 nm used by IATIA software to calculate the quantitative phase image, d is the thickness of the modified region and $\Delta\phi$ is the phase change between the modified and bulk of the material that is measured from QPM.

Examples of QPM measured type-I modifications was shown in Figure 3.4. The three bright field images were captured with 20X objective and a 8-bit mega-pixel CCD camera (Pixelink PL-A642). The NA of the condenser was set to be 80% NA of the objective. Using the QPM technique described previously, the phase information of the modified structure is shown in Figure 3.4 (a). Moreover, the differential interference contrast (DIC) image can be emulated using the calculated phase information of the structure (Fig. 1(c)). Furthermore, the QPM technique can apply both to the non-absorbing and absorbing material [83].

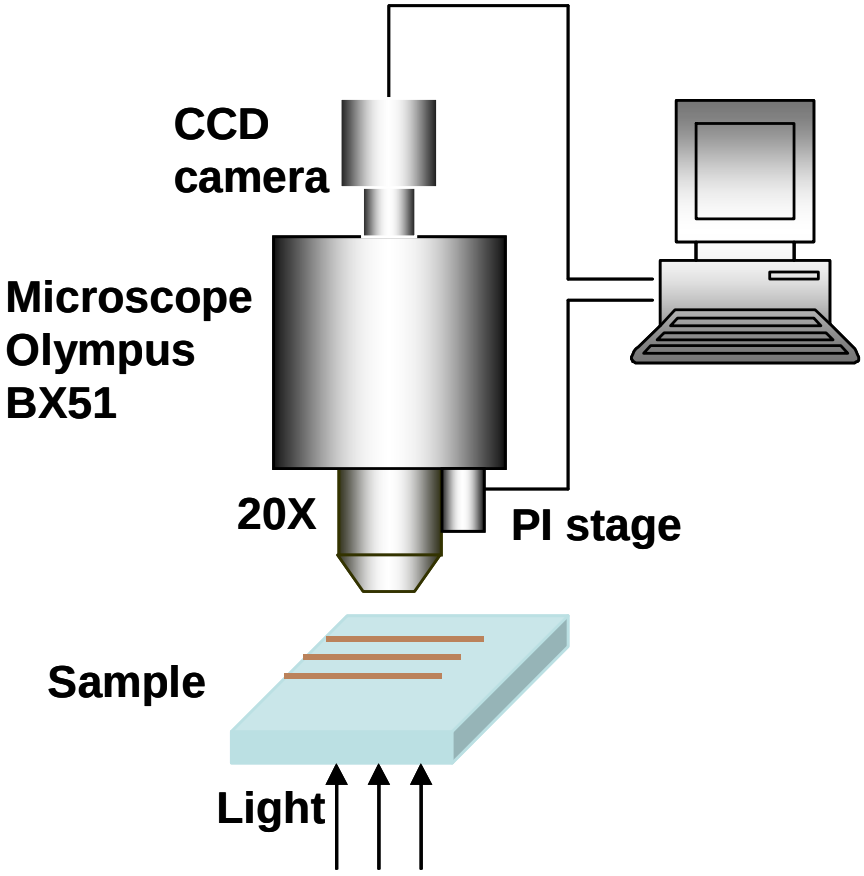

Figure 3.3: Schematic of quantitative phase microscopy setup.

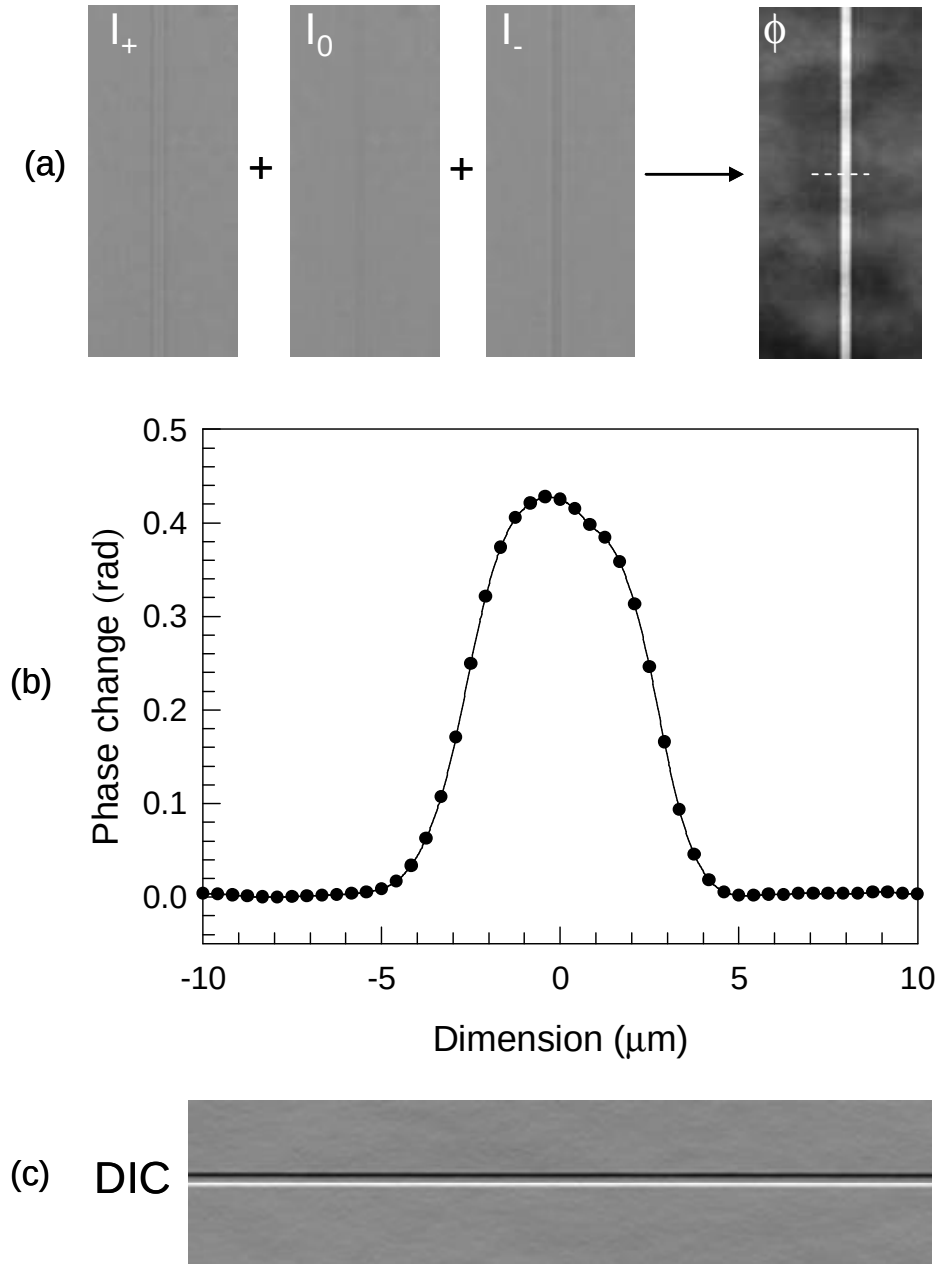

Figure 3.4: QPM measurement of the waveguide structures. (a): Three bright field images: one in one in-focus (I_0) and two very slightly positively/negatively (I_+/I-) defocused images were captured in order to calculate the quantitative phase image ϕ. (b): Quantitative phase change information of the arrow in (a) cross the waveguide structure. (c) DIC image of the waveguide structure using the calculated phase information from (a).

3.2.2 Quantitative birefringence microscopy

The type-II modification, which shows anisotropic reflections, form birefringence and negative refractive index change, attracts increasing interest in the application of microreflectors, rewritable data storage and bio-sensing [37, 42, 54, 55]. The self-

assembled periodic structures created in the irradiated volume of the fused silica account for all these phenomena. Normally, Scanning Electron Microscope (SEM) was used to image the nanogratings and distinguish them from fs induced Type-I modification. As a main drawback, this technique is time consuming and also required the sample to be polished. It was shown that femtosecond laser induced form birefringence was ascribed to the self-assembled nanogratings within the irradiate volume. As a result, the direct investigation of form birefringence is a very promising way to study the type-II modification. Here, a quantitative birefringence imaging system (CRi Abrio) was used for the measurement of femtosecond induced birefringence.

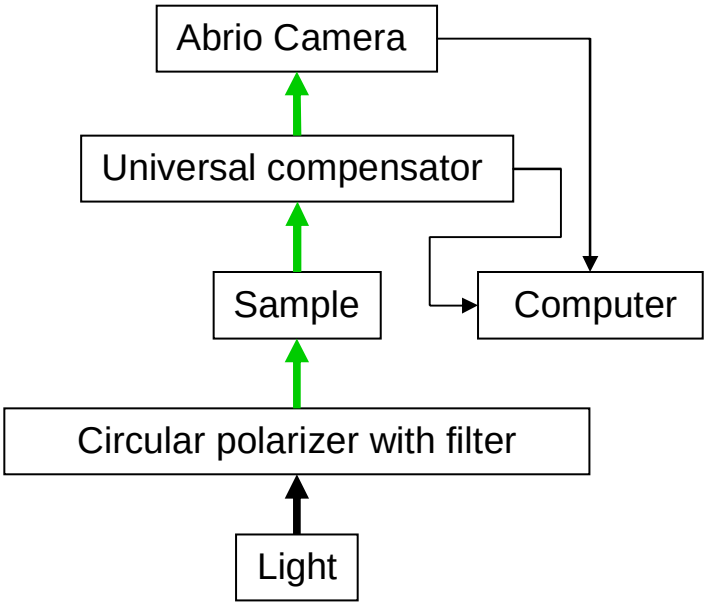

Figure 3.5: Schematic of quantitative birefringence microscopy setup.

The imaging system is also based on the Olympus BX51 optical microscope. The circular polarized green light, generated by passing the white light through the green band-pass filter and circular polarizer, was used for illuminating the sample (Fig. 3.5). The transmitted light was collected by the microscope objective and passed through the liquid crystal (LC) based universal compensator. The univeral compensator can changes the polarization state of the light with no moving parts and most importantly with no image shift. Four intensity images were recorded for various polarization state of the universal compensator. The intensity images were then processed using a specific algorithm [85, 86] embedded in the commercial software. Birefringence

information including retardance (R), which is defined as: $R = \Delta n.d$ (Δn is the refractive index difference between two directions and d is the thickness of the birefringent material) and azimuth angle(slow axis between horizontal) can be calculated. As shown in Figure 3.6, the femtosecond laser induced form birefringence inside the fused silica was measured quantitatively using this technique. The square is composed of 100 lines written inside the fused silica, with a line spacing of 1 μm, using femtosecond laser direct writing. The square behaves as a uniaxial material with a retardation of 140 nm (Fig. 3.6(b)) and a slow axis oriented vertically (Fig. 3.6(c)). The form birefringence was created as a result of self assembled nanogratings induced in the irradiated volume of the fused silica ((Fig. 3.6(a)).

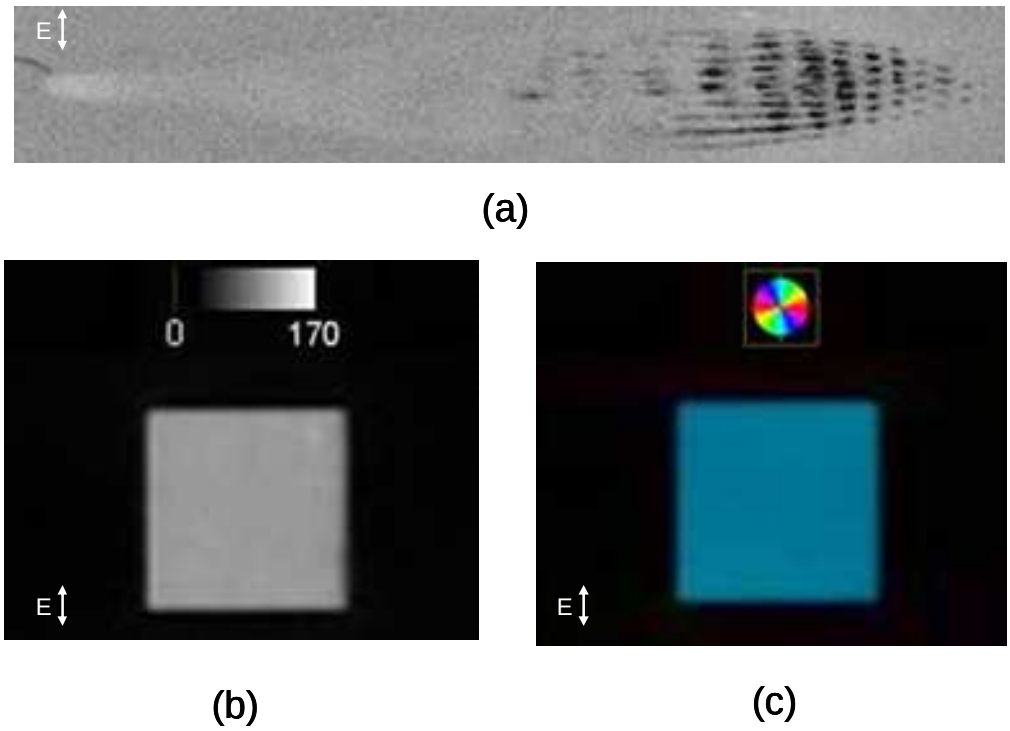

Figure 3.6: (a): SEM image of nanogratings in the fused silica after laser irradiation. (b,c): Quantitative birefringence measurement of the square, the retardation was measured in (b), and the slow axis is revealed in (c). The color of the circular legend in (c) shows the direction of the slow axis. E: electric field of the writing laser.

Chapter 4

Low loss photonic components in high index bismuth borate glass

4.1 Introduction

Integrated optical devices including channel waveguides, power splitters, couplers, gratings and waveguide lasers, are finding increasing applications in optical communication systems. Traditional manufacturing technologies for waveguides and related optical devices include photolithographic with subsequent etching, ion exchange and UV-writing. While these techniques are well established, they are limited to planar processing near the surface of the sample. In 1996 a novel technique for fabrication of waveguides and integrated optical circuits inside glass materials, by a focused ultrashort-pulse laser emerged [8]. The high intensity of a focused femtosecond laser beam enables localized non-linear absorption of laser energy in the focal volume of bulk transparent materials. The photo-generated hot electron plasma rapidly transfers its energy to the lattice, giving rise to high temperatures and pressures; this produces, by a mechanism still under investigation, a local permanent refractive index modification without affecting the surrounding area. Compared to the traditional techniques for waveguide fabrication, femtosecond direct writing provides a number of distinct advantages. First, there is no photosensitivity requirement for the processing material due to the nonlinear absorption mechanism during the ultrafast laser irradiation. Nearly all materials, especially those traditionally challenged to be modified by other methods, could be processed using this technique. By laser beam scanning or sample translation, complex structures can be directly fabricated inside the materials in a three dimensional manner. Second, the device prototyping process is quite flexible. The pattern can be easily changed by software control, with a significant cost reduction with respect to the other techniques which require photolithographic steps. Third, the direct writing is fast and a one-step process. The

laser processing setup could be very compact and the scanning speed can reach up to few meters per second.

Various optical components including: buried channel waveguides, power splitters, couplers, gratings and waveguide amplifiers have been demonstrated using femtosecond laser direct writing [8, 11-18, 20-23, 25, 26, 28, 30, 31, 67, 87-91]. However, glasses with low linear (n_0) and nonlinear (n_2) refractive indices, such as fused silica, have been used in the majority of the femtosecond laser direct writing experiments. There are only a few reports on femtosecond laser direct writing in high index glasses such as SF57, chalcogenide and heavy metal oxide glasses having $n_0 >$ 1.8 and $n_2 > 10^{-15}$ cm^2/W [18, 27, 46, 67].

Bismuth borate glass possesses a large n_2 value (5×10^{-15} cm^2/W at 1064 nm) which is almost 20 times higher than the nonlinear refractive index of silica glass [68]. This makes it an excellent candidate material for the fabrication of nonlinear optical devices such as optical switches or supercontinuum generators. Moreover, thermal poling can induce high second-order nonlinearity in bismuth borate glass [69], which can be used for fabricating nonlinear optical devices such as frequency converters or electro-optic modulators [24]. Despite these advantages, the implementation of passive waveguide components in bismuth borate glass using femtosecond laser direct writing is still unexploited.

In this chapter, we demonstrate positive index modification (type-I) in high index bismuth-borate glass using femtosecond direct writing. The slit beam shaping method, utilized in the waveguide fabrication process, was described in Section 4.2. A specific set of writing parameters leading to waveguides perfectly mode matched to standard single-mode fibers at 1.55 μm, with an overall insertion loss of ~1 dB, and with a propagation loss below 0.2 dB/cm, was identified (Sec. 4.3). Passive waveguide components such as Y-splitters and directional couplers have also been demonstrated. A close agreement between their performances and theoretical predictions based upon the characterization of the waveguide properties is shown (Sec. 4.4) Finally, the nonlinear refractive index of the waveguides has been measured to be 6.6×10^{-15} cm^2/W by analyzing self-phase modulation of the propagating femtosecond laser

pulse at the wavelength of 1.46 μm. Broadening of the transmitted light source as large as 500 nm was demonstrated through a waveguide with a length of 1.8 cm (Sec. 4.5). Section 4.6 provides a summary of the key results.

4.2 Slit beam shaping for waveguide fabrication

The bismuth-borate glass sample (BZH7) used for the waveguide fabrication has the composition of $12.5Bi_2O_3$-43.75ZnO-$43.75B_2O_3$ (mol %) and the dimensions of 30 mm × 20 mm × 0.5 mm. Using the laser system described in Sec. 3.1, the collimated laser beam was focused via a 50X objective (NA = 0.55) beneath the input surface of the sample at various depths, ranging from 10 – 200 μm. The polarization direction of the laser beam was controlled to be perpendicular to the waveguide structures. The pulse energy (E_p) was varied from 12 nJ to 1 μJ using a neutral density filter. The sample, mounted on a computer controlled xyz stage, was translated along the x-axis (Fig. 4.1(a)), perpendicular to the propagation direction of the laser beam (z-axis). The transverse writing geometry allowed the fabrication of waveguides with a length and shape limited only by the sample dimensions. However, this results in an intrinsic asymmetry of the waveguide cross-section [77]. Several techniques, including the astigmatic cylindrical telescope [77], multiple scan [26], slit beam shaping [21] and deformable mirror [78] methods have been used to overcome this problem. The slit beam shaping method was used in our experiment since it allows a simple optical setup and free adjustment to the required beam shape. By inserting a slit, orientated parallel to the writing direction (x-axis), close to the focusing objective lens (Fig. 4.1(a)), we managed to fabricate nearly circular optical waveguides (see Appendix for details).

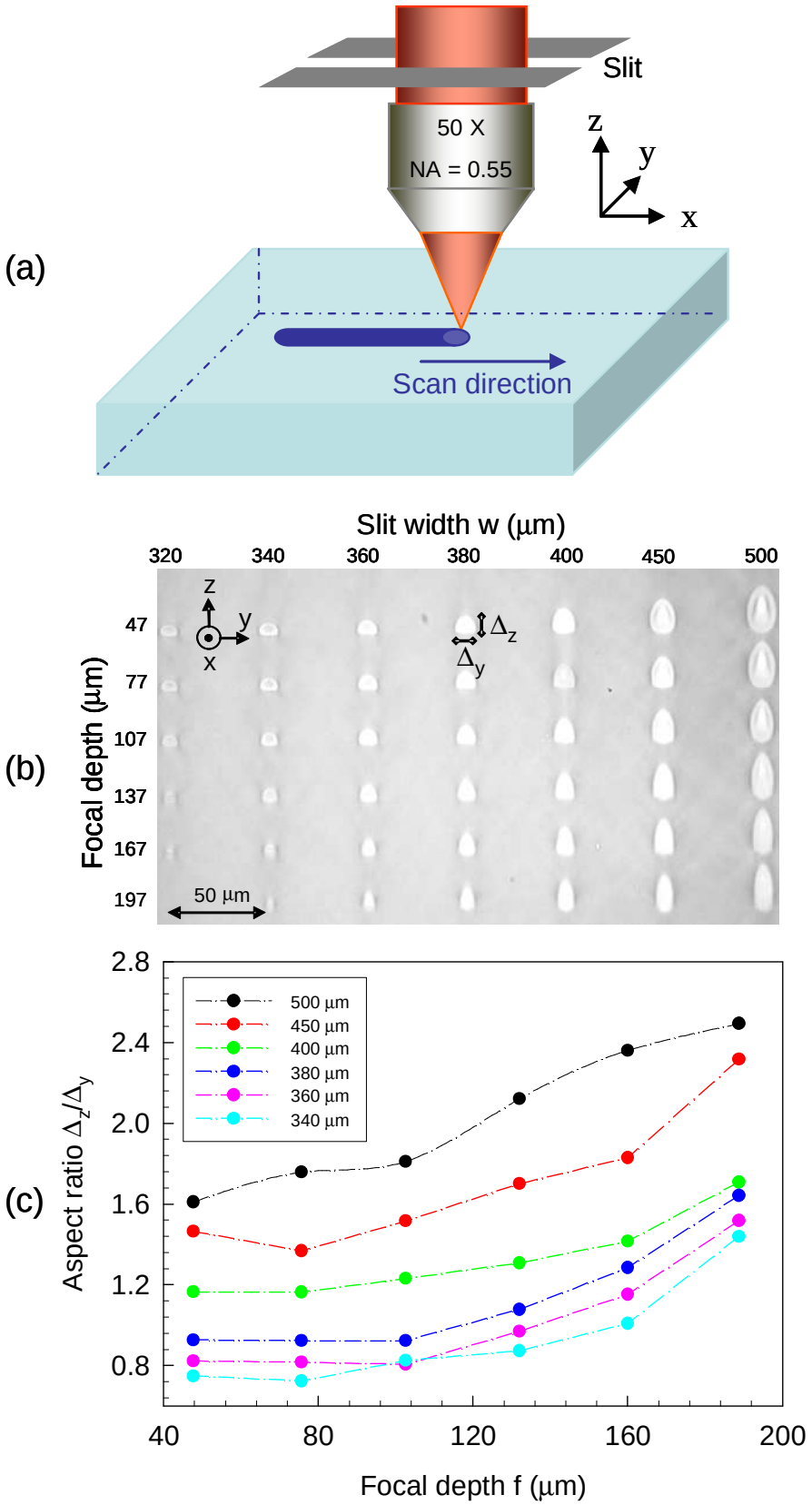

Figure 4.1: (a): Schematic of the writing process. (b): Microscope image of the waveguides in the yz plane. (c): Aspect ratio versus focal depth using various slit widths.

4.3 Waveguide Characterization

4.3.1 Waveguide cross-section

After irradiation with the ultrashort laser pulses, the sample was side-polished and checked under the optical microscope in transmission mode. In order to determine the proper slit width for fabricating waveguides with circular cross-sections, groups of channels using the same pulse energy but with slit widths varied from 320 μm to 500 μm were fabricated (Fig. 4.1(b)). The pulse energy was measured before the slit. For each column, the channels were fabricated using the same slit width and, for each row, the structures were irradiated by focusing the laser beam at a different focal depth. The aspect ratio (Fig. 4.1(b)) was decreased from 1.6 to 0.7 by reducing the slit size from 500 μm to 340 μm at the focal depth of 47 μm (Fig. 4.1(c)). By using the 380 μm slit, a nearly symmetric structural modification with the dimension of ~ 10 μm can be achieved in the yz plane (Fig. 4.1(b)). Moreover, using the same slit size, the aspect ratio could maintain the same ratio if the focal depth was less than 100 μm (Fig. 4.1(c)). Beyond this value, the effect of spherical aberration, which leads to an increase of aspect ratio, cannot be neglected. However, a cover-slip corrected objective with the designed focal depth could be used to minimize this effect.

4.3.2 Mode-field diameter and refractive index change

Near-field mode profiles of the waveguides were obtained by coupling 1.55 μm light into the waveguides using fiber butt coupling and by imaging the waveguides output facets with an Electrophysics-7290 camera using a 20X objective lens (NA = 0.3). As an example, a typical circular mode-profile for a single mode waveguide, fabricated with a 400 μm slit, 200 μm/s scan speed and 200 nJ pulse energy, is shown in Fig. 4.2(a). The $1/e^2$ mode field diameter (MFD) is measured to be 11 μm with the aid of a beam analysis system (BeamView Analyzer). The MFD of this waveguide matches well that of a standard SMF-28 fiber, having 10.4 μm MFD at 1.55 μm, therefore low insertion losses can be anticipated for this particular waveguide.

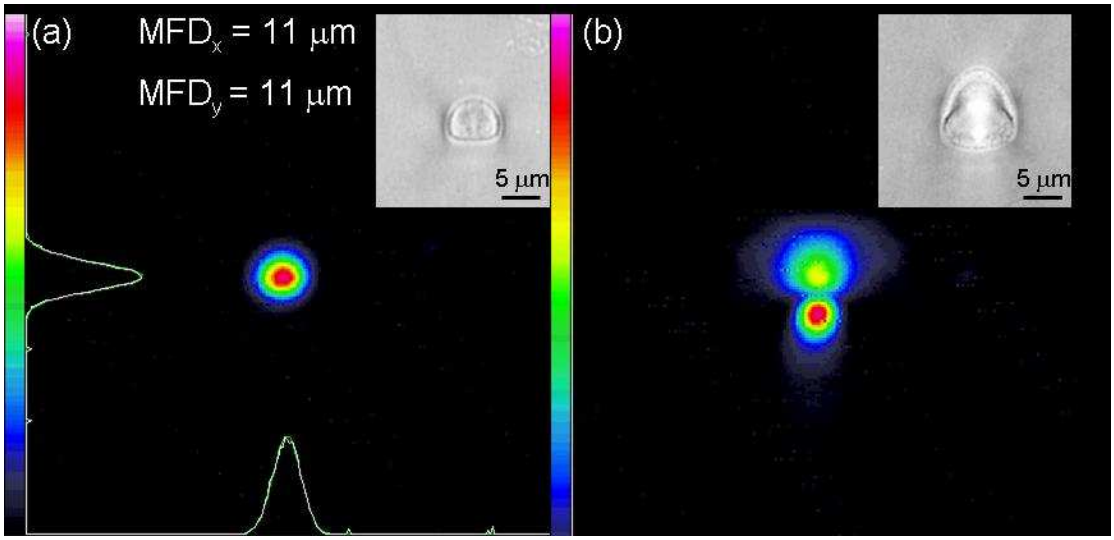

Figure 4.2: Near-field mode profiles of the waveguides at 1.55 μm and (insert) microscope images of the waveguide cross-section. (a): E_p = 200 nJ, w = 400 μm. (b): E_p = 280 nJ, w = 500 μm.

For all the waveguides fabricated in the parameter range of this study, single mode operation at telecom wavelengths was initially checked by changing the coupling conditions and ensuring that higher-order modes could not be excited. This preliminary screening allowed us to conclude that single mode waveguides in BZH7 glass can only be achieved over a narrow range of processing pulse energy, from 160 nJ to 240 nJ.

Direct confirmation of the above conclusion was provided by measuring the numerical aperture (NA) of the single mode waveguides using the beam analyzer and by estimating the normalized frequency or V-number which is defined as $V = (2\pi/\lambda)aNA$ (where "a" is the radius of the waveguides). The core radius was obtained from visual imaging of the waveguide cross-section under a calibrated optical microscope (Fig. 4.2). By assuming a step-index profile of the waveguide cross-section, the refractive index change, Δn, at 1550 nm was estimated from the measured NA value through the relation of $NA \approx (2n\Delta n)^{1/2}$ (where n = 1.8). Our results show that both Δn and V increase while increasing the pulse energy, $E_{p,}$ from 160 nJ to 280 nJ (Fig. 4.3). For pulse energies below or equal to 240 nJ it can be seen, in Fig. 3(b), that the V number is below 2.405, thus indicating single mode operation and confirming our previous observation.

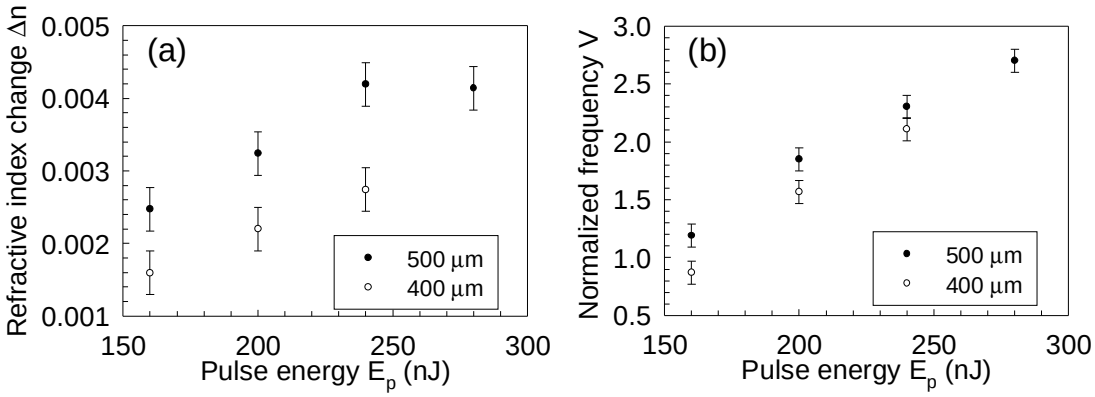

Figure 4.3: (a): Refractive index change of the waveguides fabricated using 400 μm and 500 μm slits versus pulse energy. (b): Normalized frequency of the waveguides versus pulse energy.

Δn reaches the maximum value of 4.5×10^{-3} yielding a V-number of 2.7 (Fig. 4.3(b)) and therefore indicating multimode operation (Fig. 4.2(b)), when using a 500 μm slit and 280 nJ pulse energy.

4.3.3 Insertion loss

Waveguide insertion loss measurements were performed using an external cavity tunable diode laser (Photonetics Tunics-Plus) operating in the 1.3 – 1.6 μm wavelength range. The laser beam was launched into an SMF28 single mode fiber butt coupled to the waveguides, and collected using a 10X (NA = 0.25) objective. The insertion loss was obtained from the power measured at the output waveguide facet normalized to the power at the input facet. The total insertion losses, measured at 1.55 μm for the 1.8 cm long waveguides are given in Table 4.1. The waveguide fabricated using the 400 μm slit, 200 nJ pulse energy and 200 μm/s scan speed exhibits an insertion loss of only 1 dB. Such a small value results from the circular mode profile which is perfectly mode matched to the single mode fiber and from the small propagation loss. The insertion loss of 1 dB compares favourably to the reported value of 0.7 dB/cm for the propagation loss in waveguides written in high index glass [18].

4.3.4 Propagation loss

Since Fresnel reflections at the interfaces account for 0.36 dB, or 8% loss, per facet, an upper bound of the propagation loss, can be estimated. The results, where this method yields accurate measurements, are reported in Table 4.1. The error of 0.40 dB/cm arises from three main contributions: the coupling loss error; the 1% fluctuation of the laser power and the error of 2.7% in the effective refractive index (n_{eff}).

Slit Size (μm)	Pulse Energy (nJ)	Total Insertion Loss (dB)	Propagation Loss (dB/cm)
300	200	6.93 ± 0.17	3.49 ± 0.40 [(a)]
400	160	3.85 ± 0.17	1.75 ± 0.40 [(a)]
400	200	0.98 ± 0.17	0.21 ± 0.14 [(b)]
400	240	2.16 ± 0.17	0.80 ± 0.40 [(a)]
400	280	1.70 ± 0.17	0.48 ± 0.14 [(b)]
500	160	1.45 ± 0.17	0.46 ± 0.12 [(b)]
500	200	1.37 ± 0.17	0.18 ± 0.05 [(b)]
500	240	1.79 ± 0.17	0.71 ± 0.22 [(b)]

Table 4.1: Total insertion loss and propagation loss for different waveguides. The length of the waveguides is 1.78 cm. The propagation loss is obtained from either (a) insertion loss measurements or (b) Fabry-Perot method.

The insertion loss method provides good estimates for the propagation loss, α, when $\alpha L < 0.3$ (or $\alpha > 0.74$ dB/cm for our waveguides of L = 1.8 cm) [92]. However, the best waveguides fabricated in this work appear to show a propagation loss below 0.25 dB/cm ($\alpha L < 0.1$). Such values are known to be particularly challenging to be measured and high accuracy can only be achieved with the Fabry-Perot method [24, 25].

The Fabry-Perot method owes its name to the fact that a waveguide is considered as a low-finesse symmetric resonator where the end-faces act as mirrors. By varying the wavelength of the input light source, the transmission of the waveguide cavity reaches periodic maxima (I_{max}) and minima (I_{min}). The propagation loss of a waveguide is then calculated according to Eq. 4.1, where $k = I_{min}/I_{max,}$ is the modulation ratio, $R = [(n_{eff} - 1)/(n_{eff} + 1)]^2$ is the facet effective reflectivity and L is the length of the waveguides:

$$\alpha\,[dB/cm] = \frac{4.343}{L}\ln\left(R \times \frac{1+\sqrt{k}}{1-\sqrt{k}}\right) \tag{4.1}$$

One advantage of this method is that it is independent of the value of the coupling losses. Moreover, the effective index, n_{eff}, can be directly calculated from the free spectral range $\Delta\nu$ of the cavity which is defined as $\Delta\nu = c/(2n_{eff}L)$, where L = 1.7739 ± 0.0001 cm. In order to perform the loss measurement, care has been taken while polishing the endfaces to ensure the parallelism between the two facets. The inclination was below 0.03 degrees for all the waveguides. The external cavity tunable diode laser, mentioned earlier for the characterization of the insertion loss, was also employed in the Fabry-Perot measurement as it guarantees a sufficiently narrow linewidth. The wavelength of the laser source was scanned from 1550 to 1550.4 nm in steps of 0.001 nm, which is the smallest step allowed by the instrument. The waveguide output power was recorded as a function of the input wavelength and a typical output of the measurement, relative to the waveguide written at 200 nJ pulse energy using a 500 μm slit, is given in Figure 4.4. Equally well-resolved fringes were obtained for the other waveguides albeit with different fringe visibility. The results, summarized in Table 4.1, show very good reproducibility. Overall, agreement between the insertion loss and the Fabry-Perot method is obtained with the former giving better results for higher attenuations and the latter being more suited to characterize low-loss waveguides. The measurement of the waveguide written at 200 nJ pulse energy using a slit aperture of 400 μm showed the remarkably small propagation loss of 0.21 ± 0.14 dB/cm in agreement with the indications obtained from the insertion loss measurement. The relatively large error is intrinsic of the Fabry-Perot method when applied to such low-loss waveguides. The reason can be understood from equation (4.1) by noting that the percentage error $\delta\alpha/\alpha$ comes close to infinity as α approaches zero [92].

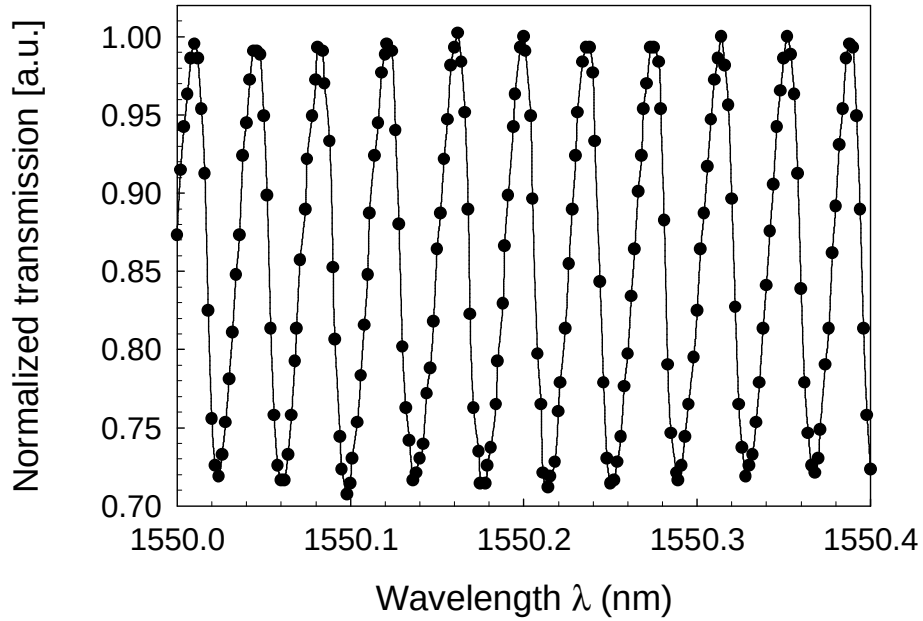

Figure 4.4: Fabry – Perot loss measurement of the waveguide (E_p = 200 nJ, w = 500 μm) at 1550 nm.

Another waveguide, written with the same pulse energy but with 500 μm slit width, showed a comparable attenuation but the error was greatly reduced by weighted average on several measurements. Further reduction of the error could be achieved by mirror-coating the waveguide end-faces to enhance the cavity finesse or by fabricating longer waveguides [92]. Within experimental errors, no polarization dependent loss was observed which comes as a direct consequence of the good circularity of the waveguides cross-section.

4.4 Optical components

Passive optical components in BZH7 glass, such as splitters and directional couplers were also fabricated and characterized.

4.4.1 Y-splitters

50:50 Y-splitters embedded in bismuth borate glass plates were written at the pulse energy of 200 nJ and scan speed of 200 μm/s using 300 and 500 μm slits. The Y-

splitters are composed of an input port which is continued by an 8 mm long straight waveguide that splits into two separate branches diverging from each other by an angle α over a length of 5 mm (Fig. 4.5(a)). For each set of writing conditions the angle α was varied between 0.4° and 2.0° in steps of 0.4°. A 50:50 splitting ratio at 1.55 μm was obtained for all the structures. The Y-branch having α = 0.4°, and written using the 500 μm slit, displayed the minimum insertion loss of 1.8 dB.

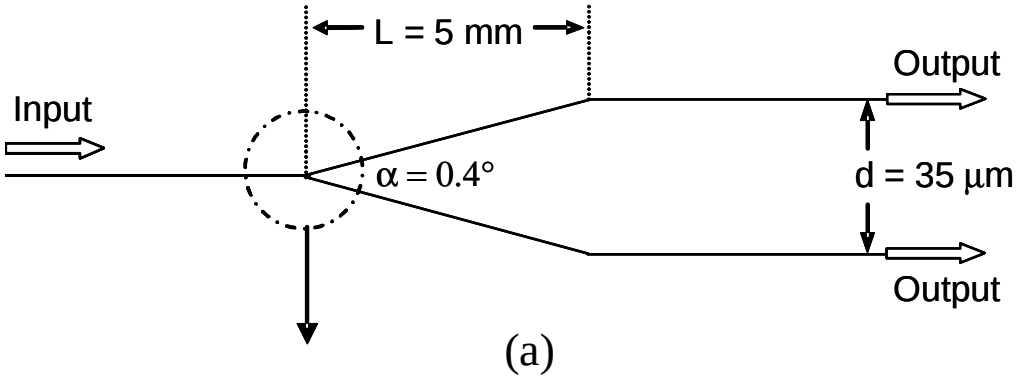

(a)

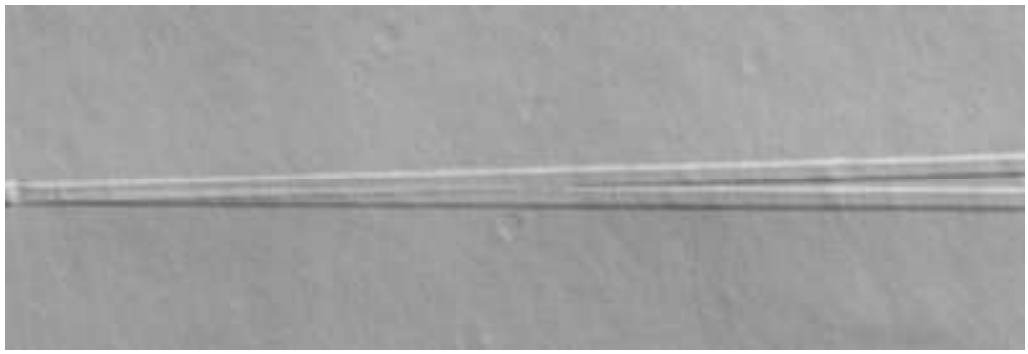

(b)

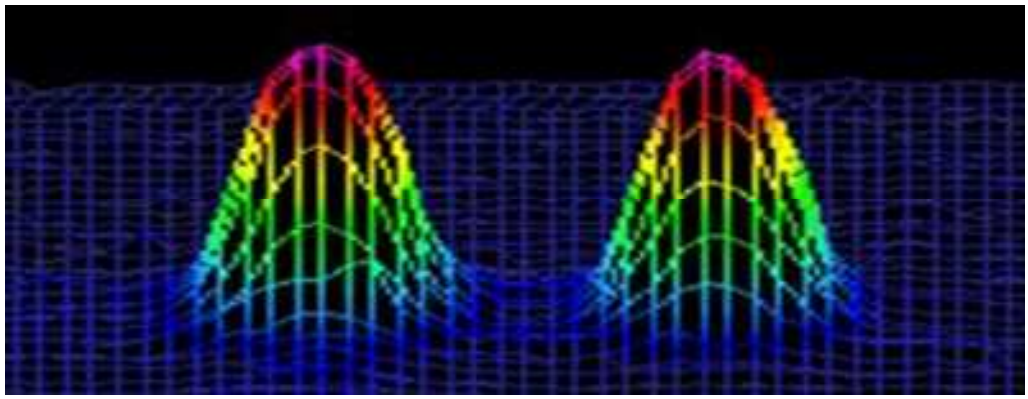

(c)

Figure 4.5: (a): Schematic of the Y – splitter (E_p = 200 nJ, w = 300 μm) (b): Differential interference contrast image of splitting part of the Y – splitter. (c): Near-field mode profile of the output facet of the Y–splitter from launching 1.55 μm light.

A differential interference contrast image of the Y-splitter is given in Fig. 4.5(b). The 50:50 splitting ratio at 1.55 μm wavelength can be appreciated from the output near-field distribution of the Y-splitter (Fig. 4.5(c)).

4.4.2 Directional couplers

Directional couplers with various coupling ratios were fabricated at 200 nJ pulse energy and 200 μm/s scan speed with slit aperture of 300 μm (Fig. 4.6). Different coupling ratios γ, defined as P_4 / (P_2+P_4), could be obtained by varying the center-to-center distance, d, between the two arms. Coupling ratios ranging from 10%, for d = 30 μm, up to 90%, for d = 15 μm, were demonstrated. The coupling ratio was also calculated using the BeamProp software (RSoft) based on beam propagation method (BPM). The simulation was done by Dr. Costantino Corbari. Assuming the step index profile and elliptical waveguide cross-section, the refractive index difference and the dimensions of the elliptical cross-section measured from microscope image were used in the simulation. The result of the computation, which is based upon experimentally measurable quantities without employing any free-parameter, is in excellent agreement with the experimental data (Fig. 4.7).

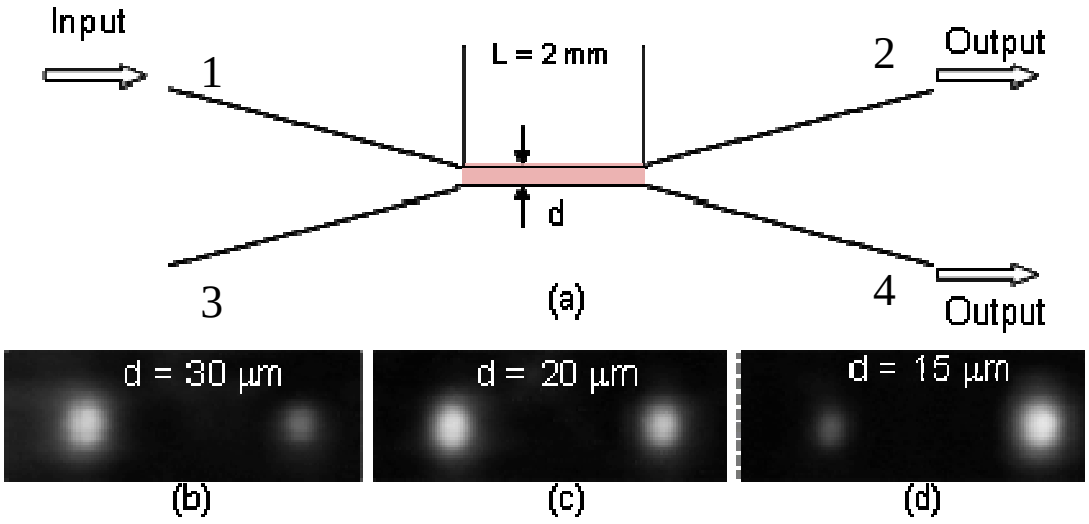

Figure 4.6: (a): Schematic of directional coupler (E_p = 200 nJ, w = 300 μm). Near-field mode profiles of the output facets of the directional couplers when the centre-centre distance d equals (b): 30 μm. (c): 20 μm. (d): 15 μm.

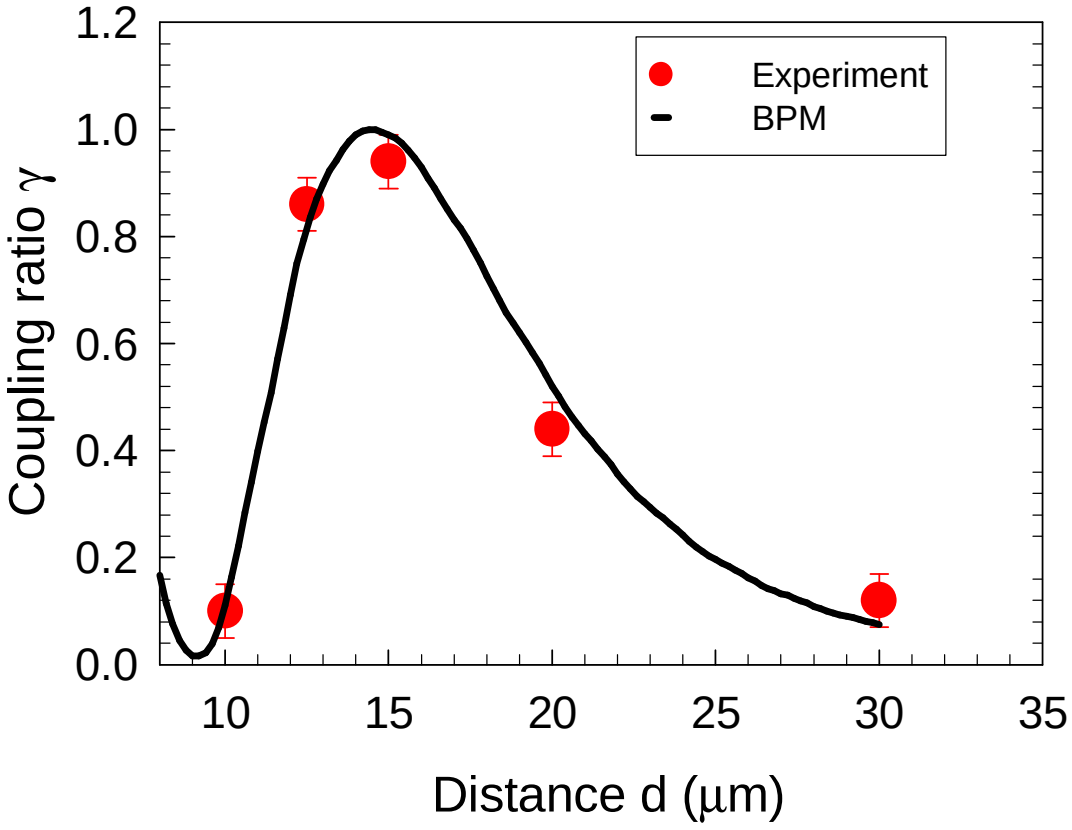

Figure 4.7: Coupling ratio γ against center-center distance d.

4.5 Characterization of second- and third-order optical nonlinearities

Finally the potential of photonics components in BZH7 glass for non-linear optical applications such as for supercontinuum generation is assessed by measuring the non-linear refractive index n_2. A Ti:sapphire OPA system emitting pulses of ~ 150 fs at 1.46 μm with a 250 kHz repetition rate was used for this purpose. A linearly polarized laser beam was coupled into the waveguide by a 4X microscope objective (NA = 0.12). The transmitted light was then collected by a 10X objective (NA = 0.3) and coupled into an optical spectrum analyzer using a multimode fiber.

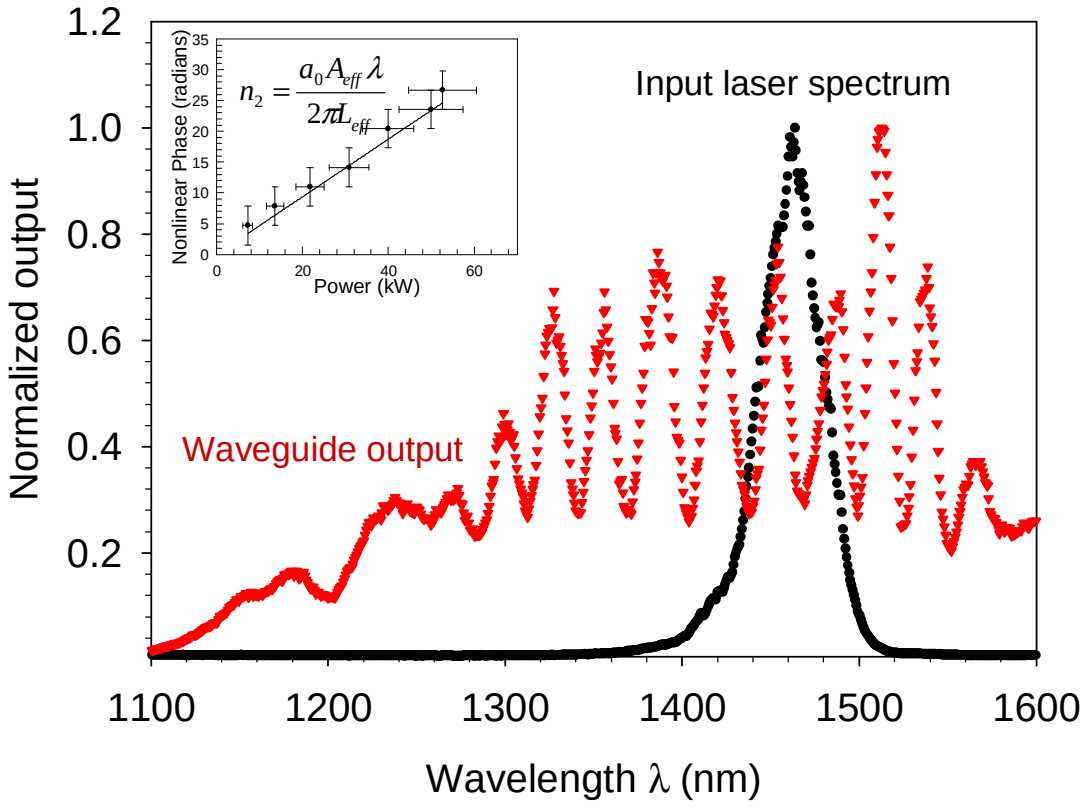

Figure 4.8: Normalized spectrum of the input pulse (black) and spectrum of the pulse (red) collected after propagation through the waveguide (E_p = 240 nJ, w = 500 μm).

The largest spectral broadening was observed in the waveguide written with 240 nJ and a 500 μm aperture. As the peak power in the waveguide was increased, the output spectrum broadened by up to 500 nm, corresponding to a phase shift of approximately 8.5π (Fig. 4.8). This broadening is due to self-phase modulation of propagating light inside the waveguide with average power of only 2.0 mW [93]. Since the pulse has the same instantaneous frequency at two distinct points, these two points represents the waves of same frequency but different phases that can interfere constructively or destructively depending on their relative phase difference. As a result, this interference produces multi-peak structures in the spectrum [93]. In this experiment, no index modification was induced, which was confirmed by the linear dependence of the output power versus the input power. The nonlinear refractive index n_2 of the waveguide was estimated to be $(6.6 \pm 0.5) \times 10^{-15}$ cm^2/W, which is comparable to the reported value of 5×10^{-15} cm^2/W at 1064 nm for the bulk bismuth-borate sample [68] and about 20 times higher than the n_2 of fused silica.

Preliminary experiments were carried out on thermal poling of the fabricated waveguides and to investigate the effect of the femtosecond laser induced modifications on the second-order nonlinearity ($\chi^{(2)}$) produced by poling in bismuth glass. The thermal poling was carried out at 290 ^{o}C for 5 minutes at a constant current of 100 μA [94]. The second-order nonlinearity of $\chi^{(2)}$ = 0.8 pm/V was measured using the Maker's fringe technique. The spatial overlap between the guided mode in the waveguides and the second-order nonlinearity induced by poling was optimized by fabricating a set of waveguides with different depth under the glass surface. The uniformly poled waveguides were then tested for evidence of second-harmonic generation (SHG) by launching 1064 nm radiation from a Q-switched (repetition rate 1 kH, 200 ns pulse duration) and mode-locked (76MHz, 300 ps) Nd:YAG laser. The second harmonic (SH) signal was produced only in the waveguides buried less than 10 μm below the surface which was in agreement with the expected depth of the nonlinear region in our glass samples.

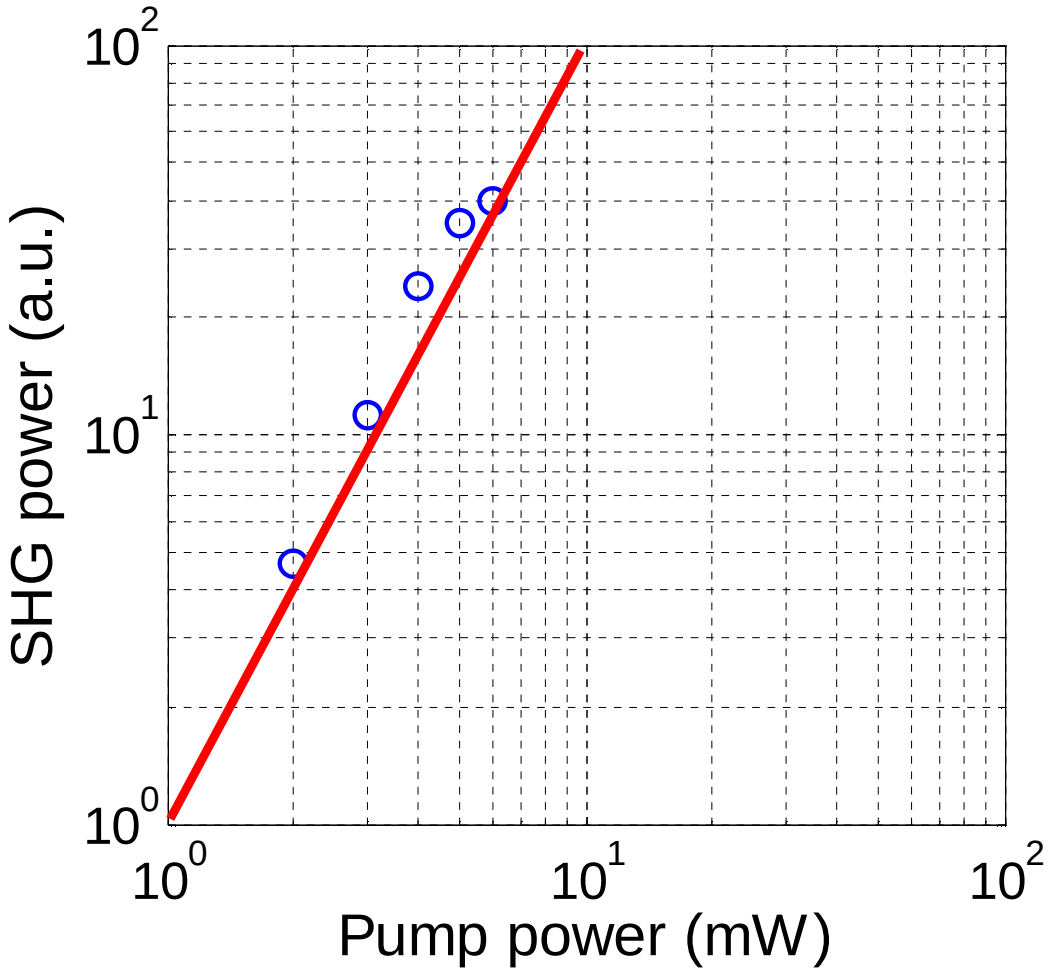

Figure 4.9: Quadratic dependence of the SHG power against the fundamental pump power.

The measured SH signal exhibited quadratic growth on the pump power (Fig. 4.9) and was about 3 times higher for the TM-polarized pump light compared to the TE-polarized light. The deviation from theoretical ratio of the SH harmonic signals of 9:1 is commonly observed in poled waveguides [95]. Under the assumption that modal-phase matching was not taking place in the waveguides, the SHG efficiencies for the waveguide and the bulk geometries were compared. In the bulk geometry the pump light was focused on the surface of a uniform region of the poled sample between the waveguides. After scaling the power densities for the two geometries and considering that the nonlinear interaction takes place at a coherence length, the values of the second-order nonlinear coefficient were found to be the same for the femtosecond laser written waveguide and for the bulk of the glass. Since in poled glass, $\chi^{(2)}=3\chi^{(3)}E_{dc}$, where E_{dc} is the frozen-in field, this result indicates that the third-order

nonlinearity in BZH7 glass is not affected by the femtosecond laser writing process as it was concluded from the n_2 measurements presented above.

4.6 Conclusion

Low loss, polarization insensitive, single mode waveguides with circular mode profiles and refractive index changes of 4.5×10^{-3} were inscribed by ultrafast laser radiation in high index bismuth-borate glass. Insertion loss of only 1 dB and propagation loss of 0.2 dB/cm at 1.55 μm were demonstrated. Y-splitters and directional couplers were also fabricated and their performances closely agree with theoretical simulations based upon experimentally measurable quantities obtained from the waveguide characterization. Moreover, a 500 nm spectral broadening was obtained by launching less than 2.0 mW average power (53 kW peak-power) of 150 fs laser pulses at 1.46 μm through the waveguides. The broadening and quality of the supercontinuum could be further increased by pumping closer to the zero-dispersion wavelength. In our case the supercontinuum is mainly caused by self-phase modulation allowing the estimation of a nonlinear refractive index n_2 of ~ 6.6×10^{-15} cm^2/W, which is in agreement with published data [68]. Preliminary experiments on the uniformly poled waveguides show the same $\chi^{(2)}$ value as the bulk glass. Further experiments to implement quasi-phase-matching in periodically poled waveguides are in progress. Femtosecond laser written low loss waveguides with large n_2 are attractive for fabricating nonlinear glass based devices.

Chapter 5

Self-assembled nanostructures by femtosecond laser direct writing

5.1 Introduction

In the previous chapter, type-I modification, i.e. the isotropic positive refractive index modification, has been demonstrated in bismuth borate glass using femtosecond laser irradiation leading to a promising technique for fabricating waveguides based devices in glasses. In this chapter, the femtosecond laser induced type-II modification, which shows form birefringence and negative refractive index change will be studied.

Previous experimental work has shown that structures written in fused silica by femtosecond laser pulses above a certain intensity threshold exhibit anisotropic reflection [37]. At that time, the appearance of anisotropic reflection, only in the direction of the polarization of the writing laser beam, could be explained by assuming that a sub-wavelength period grating was formed within the irradiated focal volume. This explanation was further strengthened by the consideration that the orientation of the suspected nanogratings was identical to that implied by the empirical observation of anisotropic light scattering in our previous work [35]. The first experimental evidence of self-assembled nanostructures created within irradiated regions in fused silica was presented in [39]. This type of periodic structure, whose period is smaller than the laser's wavelength, explained the concurrent appearance of anisotropic reflection [37], a permanent birefringent micro-layer [38], form birefringence, and an average negative index change [40]. Moreover, changes in the nanogratings due to variations of the pulse duration have been qualitatively investigated [45]. The extraordinary stability of these nanogratings has also been reported [47]. Furthermore, embedded micro-reflectors, Fresnel lens, and micro-

fluidic channels based on these nanostructures have been reported [37, 38, 54]. However, in order to have a better understanding of the mechanisms responsible for the formation of the nanostructures, and consequently how to efficiently exploit them, a systematic study of the properties of nanostructures and their dependence on various irradiation parameters is required.

In this chapter, the investigation of nanogratings in the plane of propagation of light was carried out (Sec. 5.2). In addition, the quantitative analysis of the dependence of the nanograting period, as a function of laser parameters was completed (Sec. 5.3). Moreover, it was demonstrated that the range of effective pulse energy, which could produce nanogratings, narrows, when the pulse repetition rate of the writing laser is increased (Sec. 5.4). The application of these nanogratings is discussed in Section 5.5.

5.2 Nanogratings in the plane of propagation of light

In order to study the dependence of nanogratings on various laser parameters, including the wavelength and repetition rate of the laser pulses, two different types of laser systems have been used in the experiments. The first laser source was a regeneratively amplified mode-locked Ti:Sapphire laser system (see Sec. 3.1 for details). The second laser source was a variable repetition rate fiber laser system operating at both 1045 nm and 522 nm (IMRA America FCPA μJewel D-400). The repetition rate was adjusted from 100 kHz to 1MHz and the pulse duration was 400 fs. Using the laser processing setup described in Sec. 3.1, straight lines were written inside the fused silica sample by translating the sample along the +y direction, perpendicular to the propagation direction of the laser beam (z-axis), as shown in Fig. 5.1(a). After laser irradiation, the sample A was analyzed using a scanning electron microscope (SEM) (JSM6500) after chemical etching. Another two samples B and C were imaged using backscattering SEM without etching.

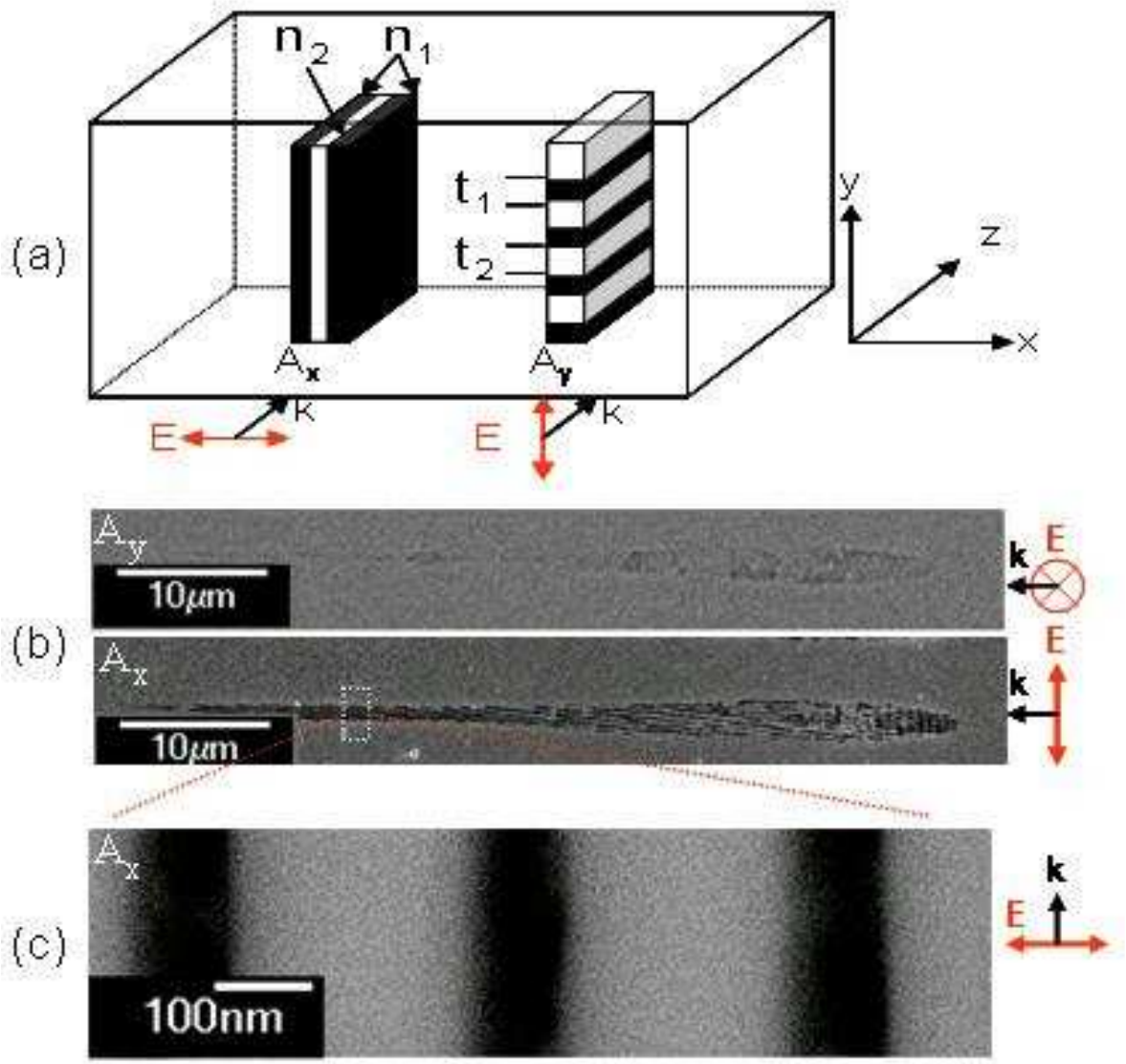

Figure 5.1: Modified regions in sample A. E: electric field of the writing laser, k: wave vector of the writing laser beam, line A_x and line A_y: E_p = 0.48 μJ, V = 200 μm/s, λ = 850 nm. (a): Schematic of the sample A showing how the self-assembled periodic structures are expected to be arranged. n_1 and n_2: local refractive indices of the plates of thickness t_1 and t_2, respectively. (b): SEM images of A_x and A_y in the xz plane. (c): Detail of the sub-wavelength periodic structure formed in the cropped region of A_x.

As depicted in Fig. 5.1(a), only the line A_x written with the polarization along x-axis (Fig. 5.1(b)), in the plane of observation (xz) reveals the periodic modulation of the index change (for these structures, xz is the plane perpendicular to the plates forming the nanogratings). On the contrary, the corresponding line A_y, written with the same conditions, but with the polarization along y-axis (Fig. 5.1(b)) shows a homogeneous profile (for these structures, xz is the plane parallel to the plates forming the

nanogratings). Figure 5.1(c) is a close-up of part of Fig. 5.1(b) revealing that the filling factor f is ~ 0.3, twice as high as the results reported in [37] (the filling factor is defined as $f = t_1 / \Lambda$, with t_1 the thickness of the zones of refractive index n_1 in Fig. 5.1(a), and Λ the period of the nanograting). In addition, the SEM image of the etched sample reveals the surface relief created in the etching process due to the density variations in the gratings. Figure 5.1(c) demonstrates an abrupt change of density between the dark area with low density of the material (i.e. the zones of refractive index n_1 in Fig. 5.1(a)), and the surrounding regions (i.e. the zones of refractive index n_2 in Fig. 5.1(a)), suggesting that the mechanism leading to the modulation of the refractive index is highly nonlinear. Furthermore, the mechanism of the structural changes responsible for the nanograting formation involves the modulation of the electron concentration, negatively charged oxygen ions can be repelled from the dark area with high electron concentration [39].

5.3 Dependence of nanograting period on laser parameters

Figure 5.2 presents SEM images of the modified region in the xz plane induced by three different writing laser wavelengths in sample B and sample C. The periodic structures can be observed in the head of the modified regions. Besides the main period Λ_E, which is in the direction of the polarization of the laser beam (E), a second period Λ_k is identified perpendicular to Λ_E, and hence parallel the direction of propagation of the laser beam (k), as shown in Fig. 5.2. Furthermore, Λ_k is 710 ± 10 nm at 1045 nm (Fig. 5.2(a)), 550 ± 10 nm at 800 nm (Fig. 5.2(b)), and 360 ± 10 nm at 522 nm (Fig. 5.2(c)) in the head of the modified region, which is very close to the wavelength of light in fused silica.

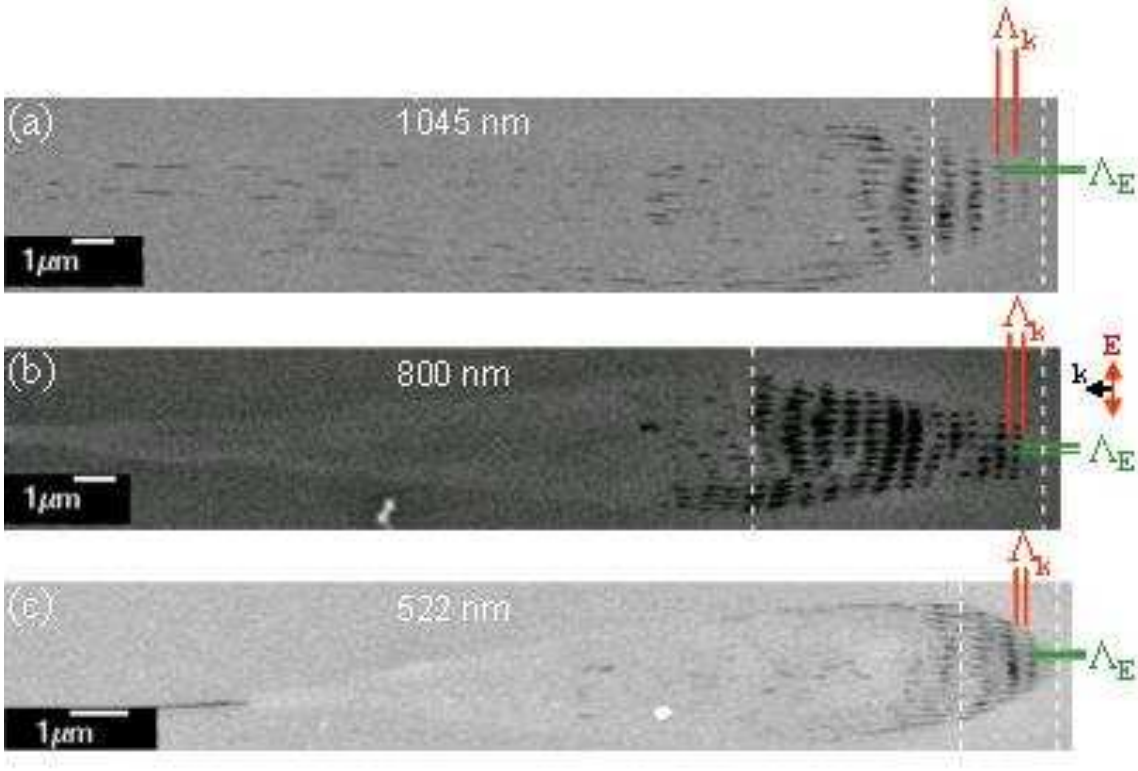

Figure 5.2: SEM images of nanogratings formed by three different central wavelengths of the irradiated laser pulses in sample B and sample C, the region between two dotted lines is used for period calculation, E: electric field of the writing laser, k: wave vector of the writing laser beam. (a): τ_p = 520 fs, E_p = 0.9 μJ, V = 200 μm/s, R_{ep} = 500 kHz. (b): τ_p = 150 fs, E_p = 0.5 μJ, V = 100 μm/s, R_{ep} = 250 kHz. (c): τ_p = 490 fs, E_p = 0.15 μJ, V = 200 μm/s, R_{ep} = 200 kHz.

In order to quantitatively analyze the period Λ_E and Λ_k, an algorithm based on the correlation coefficients between different points in the SEM image versus their distance was developed. By calculating the average value of the periods from the first maximum of the correlation functions, periods along the x and z direction are obtained, as shown in Fig. 5.3.

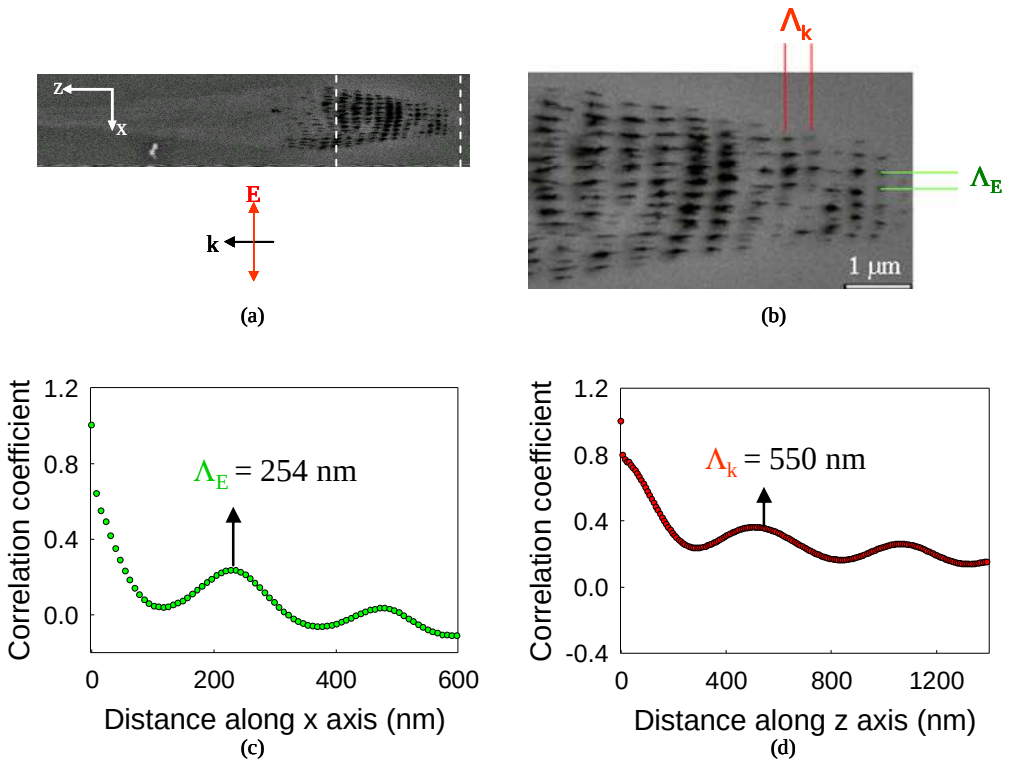

Figure 5.3: (a): SEM image of a written line in the xz plane, E: electric field of the writing laser, k: wave vector of the writing laser beam (λ = 800 nm, τ_p =150 fs, E_p = 0.5 μJ, V = 100 μm/s, R_{ep} = 250 kHz). (b): The region between two dotted lines is used for calculation. Corresponding normalized correlation functions calculated along the x (c) and z (d) axis.

It is revealed that Λ_E decreases with increasing E_p within our study range (Fig. 5.4(a-b)). In addition, the wavelength dependence illustrated in Fig. 5.4(a) suggests that shorter wavelengths yield significantly smaller structures; this is also confirmed in Fig. 5.5(a), which demonstrates that the period Λ_E is proportional to the wavelength of the writing laser. Furthermore, Λ_k in the head of the laser-modified region does not change with the pulse energy or speed and is confirmed to be approximately equal to the laser wavelength (Fig. 5.5(b)).

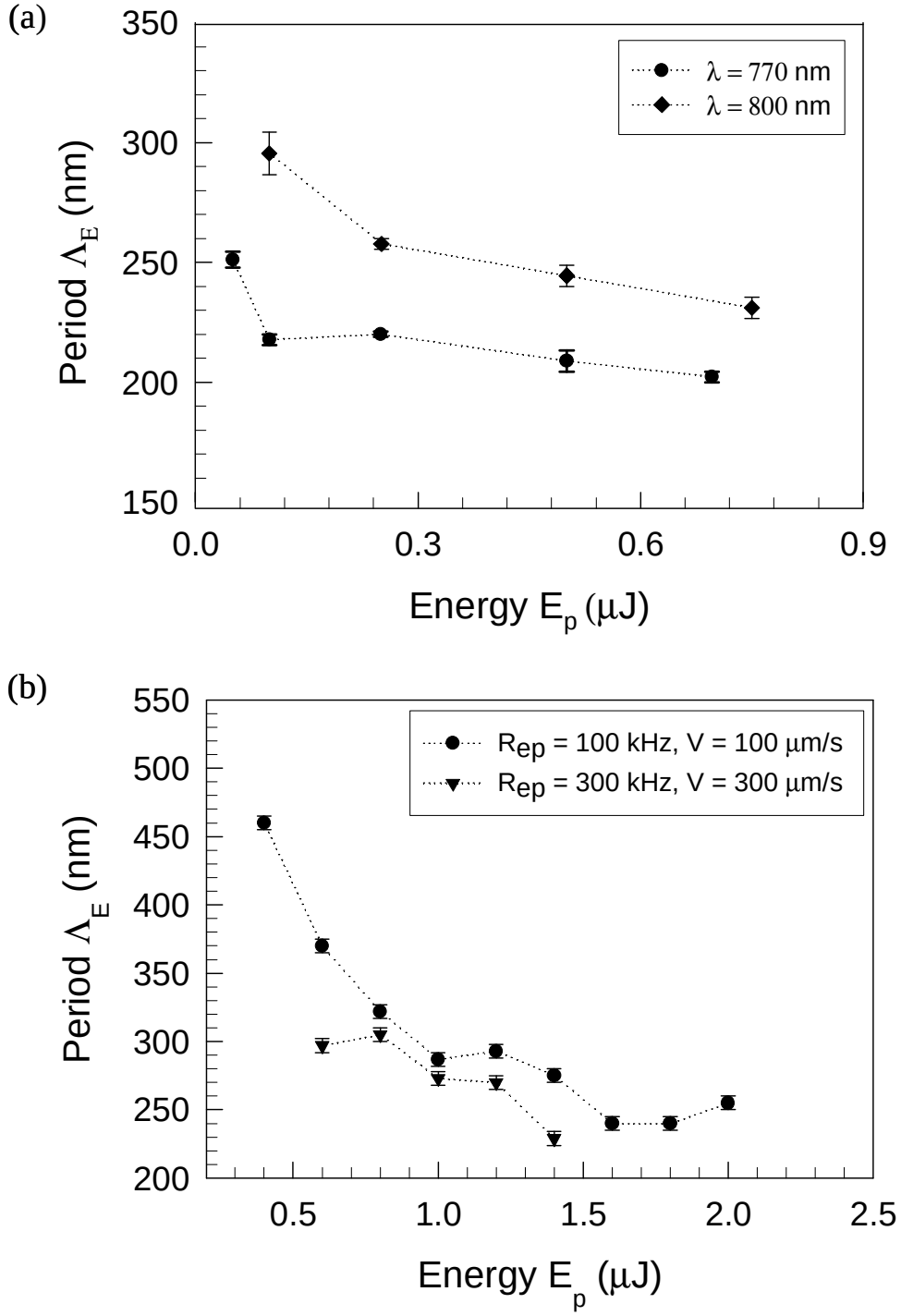

Figure 5.4: (a): Period Λ_E versus E_p (τ_p = 150 fs, R_{ep} = 250 kHz, V = 100 μm/s). (b): Period Λ_E versus E_p (τ_p = 480 fs, λ = 1045 nm).

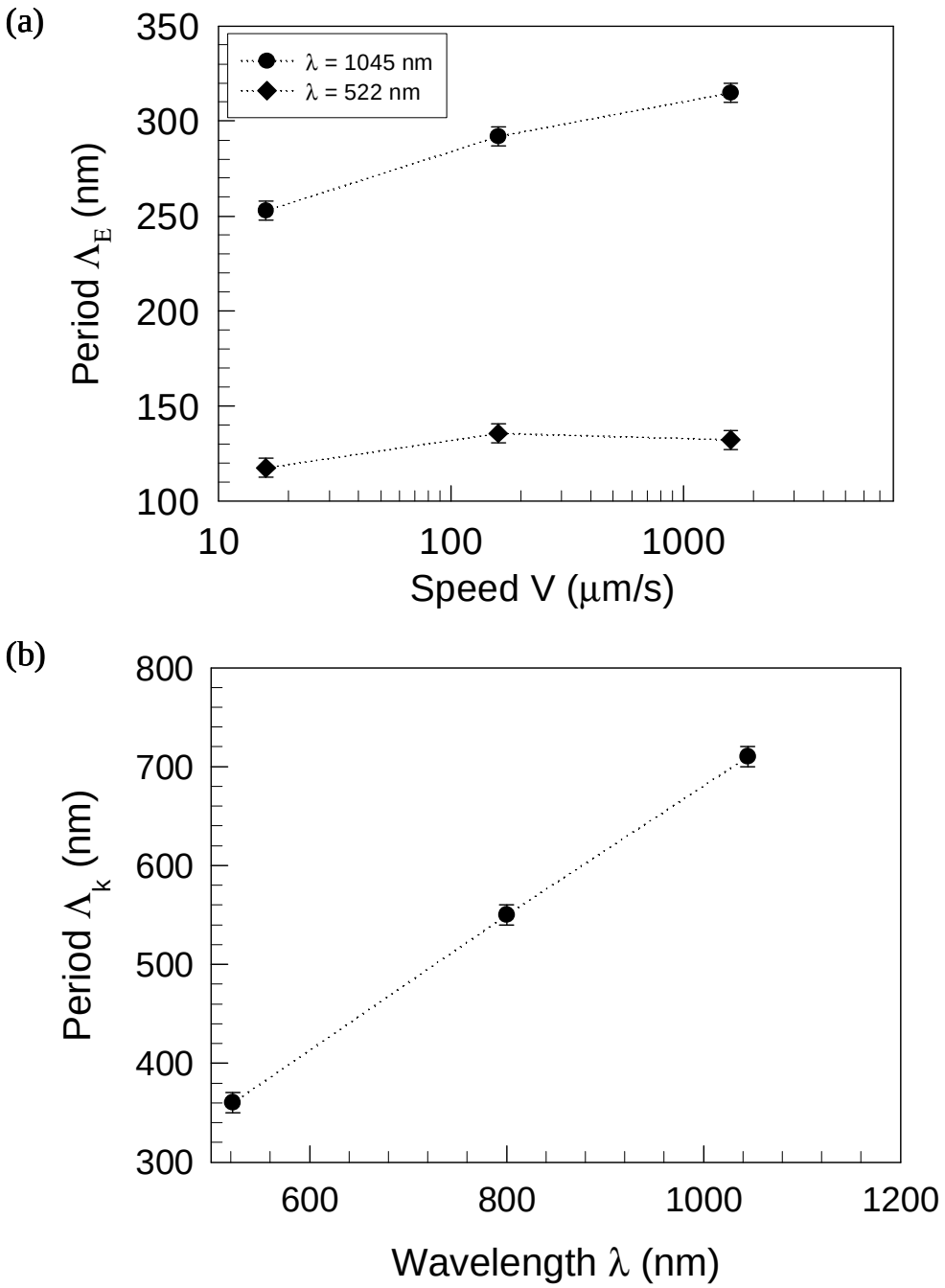

Figure 5.5: (a): Period Λ_E versus speed V at two different wavelengths (τ_p = 400 fs, R_{ep} = 200 kHz, E_p = 0.5 μJ). (b): Period Λ_k versus three different wavelengths.

5.4 Nanogratings formed in various repetition rate regimes

In order to study the nanogratings under various repetition rate regimes, lines structures induced in sample C were inspected using the Nomarkski-DIC microscope. It shows that, when the repetition rate of the laser pulses reaches 500 kHz and E_p is over ~1 μJ (Fig. 5.6(a)), or when the repetition rate reaches 1 MHz and E_p is over ~ 0.6 μJ (Fig. 5.6(b)), no birefringence or nanogratings could be observed in the irradiated regions of the sample. This could be explained by the occurrence of an accumulation effect within the focal volume when the pulse repetition rate is greater than ~500 kHz [89, 96, 97]. This indicates that the range of the pulse energy which could produce self-assembled nanogratings narrows when the pulse repetition rate of the laser increases.

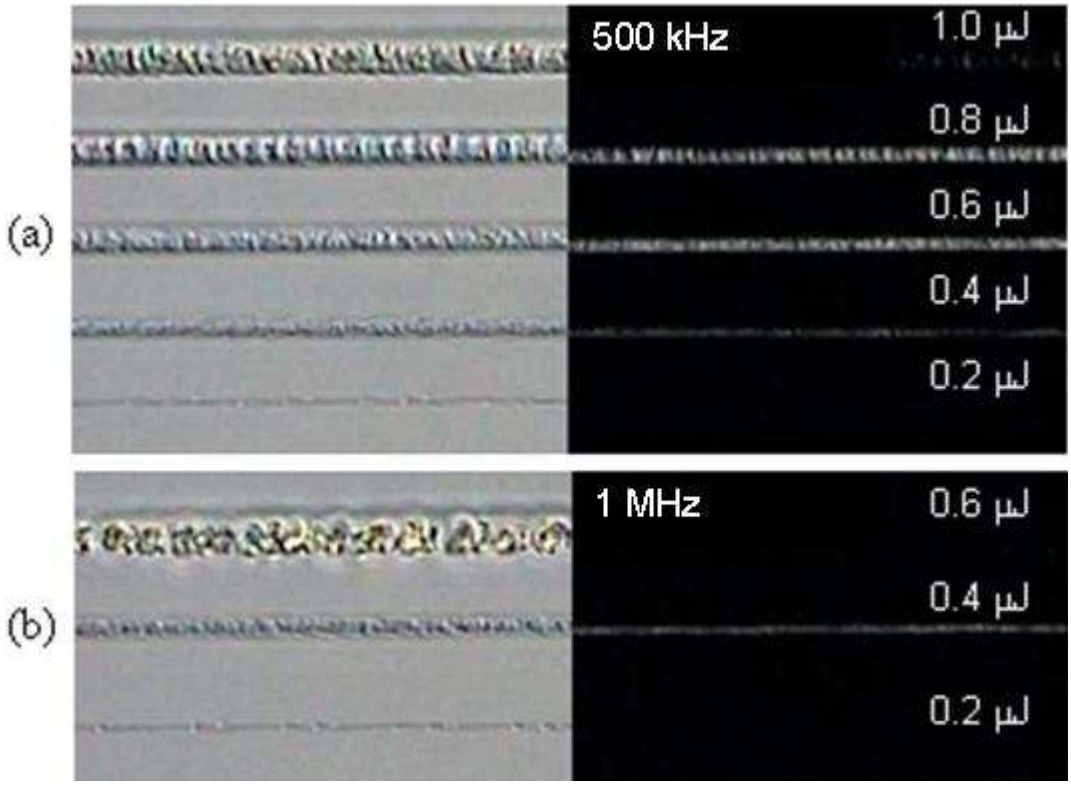

Figure 5.6: Microscope images of the irradiated regions in the xy plane in sample C, image on the left taken by back-illumination without polarizers, image on the right taken by back-illumination with cross polarizers of the same irradiated area. (a): R_{ep} = 500 kHz, V = 500 μm/s. (b): R_{ep} = 1 MHz, V = 1000 μm/s.

5.5 Application of type-II modification

Our previous experimental results showed that over a certain intensity threshold, these femtosecond laser induced periodic structures behave as an uniaxial form-birefringence material [40]. This is also confirmed using the FCPA μJewel D-400 at wavelengths of 1045 nm and 522 nm. Figure 5.7 shows a replica of IMRA's icon that was made by raster-scanning closely spaced lines (10-μm spacing).

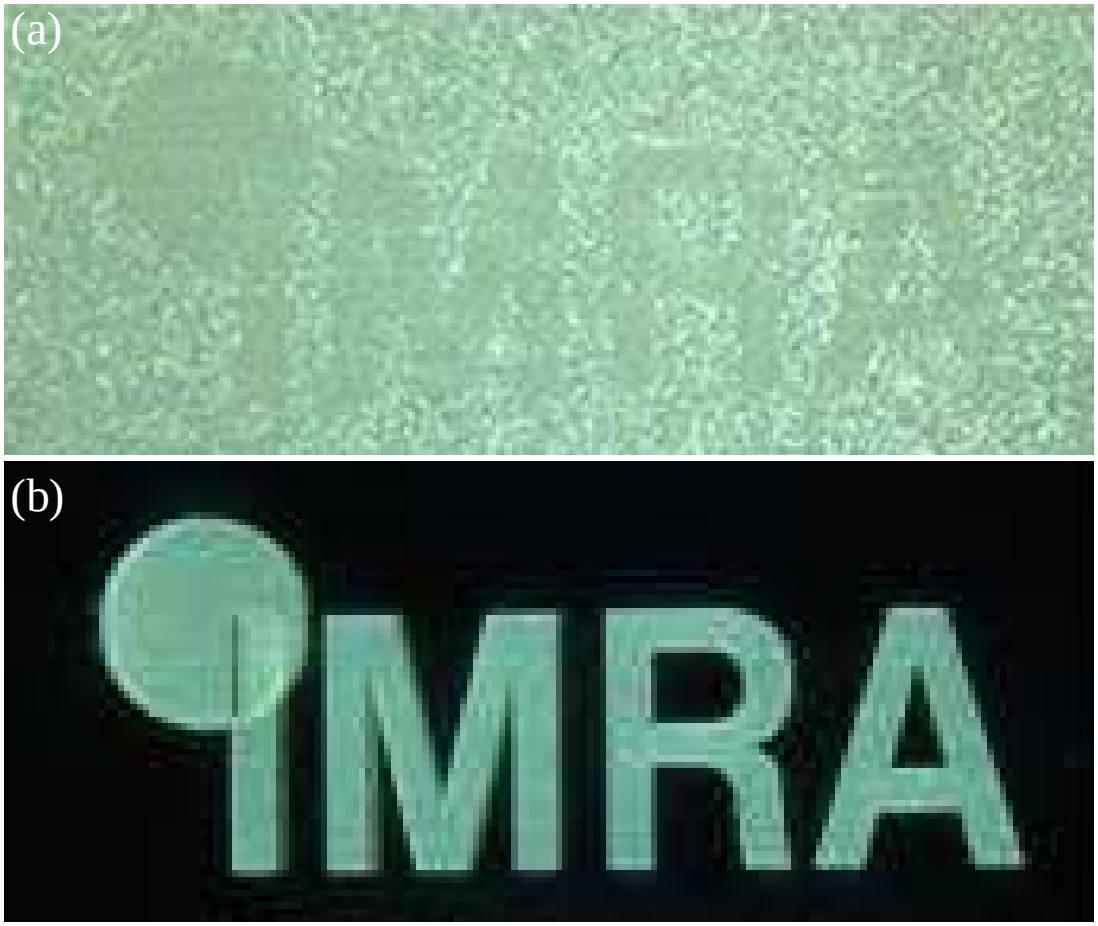

Figure 5.7: Raster scanned replica of IMRA icon, 10-μm line spacing, 500-kHz repetition rate, 1045-nm wavelength, 1.5-μJ pulse energy, ~12-hour process time, ~10-mm icon width. (a): Imaged without cross-polarizers, (b) Imaged with cross-polarizers.

5.6 Conclusions

In conclusion, two different types of periodic structures have been identified from cross-sectional SEM images of femtosecond pulse-modified regions in fused silica. The range of pulse energy which could produce nanogratings narrows when the pulse repetition rate of the writing laser increases. The period Λ_E is proportional to the wavelength of the writing laser and the period Λ_k in the head of the modified region (the region between two dotted lines in Fig. 5.2) remains the wavelength of light in fused silica.

Chapter 6

“Quill” writing with ultrashort light pulses in transparent optical materials

6.1 Introduction

Femtosecond laser induced type-I and type-II modifications in glasses and their applications have been presented in the previous chapters. The type of modification depends on several factors including the laser parameters (wavelength, pulse duration, energy and repetition rate), the numerical aperture of a focusing lens and the material parameters (band-gap, thermal properties). In fused silica, the transition from type-I to type-II and finally to type-III modification is observed with an increase of pulse energy [8, 34, 48]. Here in this chapter a new phenomenon was discovered in ultrafast laser processing of transparent optical materials. The phenomenon is manifested as a change in material modification by reversing the writing direction. The effect resembles writing with a quill pen and is interpreted in terms of new physical effect - anisotropic trapping of the electron plasma by a tilted front of the ultrashort laser pulse. Indeed the pulse front tilt can be used to control material modifications and in particular as a new tool for laser processing and optical manipulation, e.g. for achieving calligraphic style of laser writing, when the appearance of a “stroke” varies in relation to its direction. Moreover new types of modifications manifested as anisotropic bubble formation and bubble-nanograting transition were observed at high pulse energies.

The observation of the structural modification dependence on the writing direction is described in Section 6.2. The physical mechanism for this quill writing effect is discussed in Section 6.3. Different types of modification can be produced inside the

transparent material by reversing the direction of the tilted pulse front (Sec. 6.4). The anisotropic bubble formation and bubble-nanograting transition are revealed in Section 6.5.

6.2 Observation of directional dependence

Using the laser processing setup described in Sec. 3.1, a series of lines, with 7-μm spacing, were directly written by scanning in alternating directions towards the edge of the sample at a depth of 0.5 mm below the front surface. The writing speed was 200 μm/s and each line was written with only one pass (in one direction) of the laser, with the polarization directed perpendicular to the line and with a pulse energy of 0.9 μJ. After writing, the structures were side-polished and imaged with a Scanning Electron Microscope (SEM). The SEM images expose tracks that are elongated in the direction of light propagation due to the beam’s confocal parameter, and enhanced by self-focusing effects, with a periodic structure in the direction of light polarization (Fig. 6.1). On closer inspection it was surprising to observe a difference in the structures written in opposite directions. This difference is revealed in small variations of the length of the tracks and also in a tilt of the periodic structures written in the forward and reverse directions. The periodic planar nanostructures are aligned along the direction of the writing laser polarization and are responsible for the form birefringence of the irradiated regions.

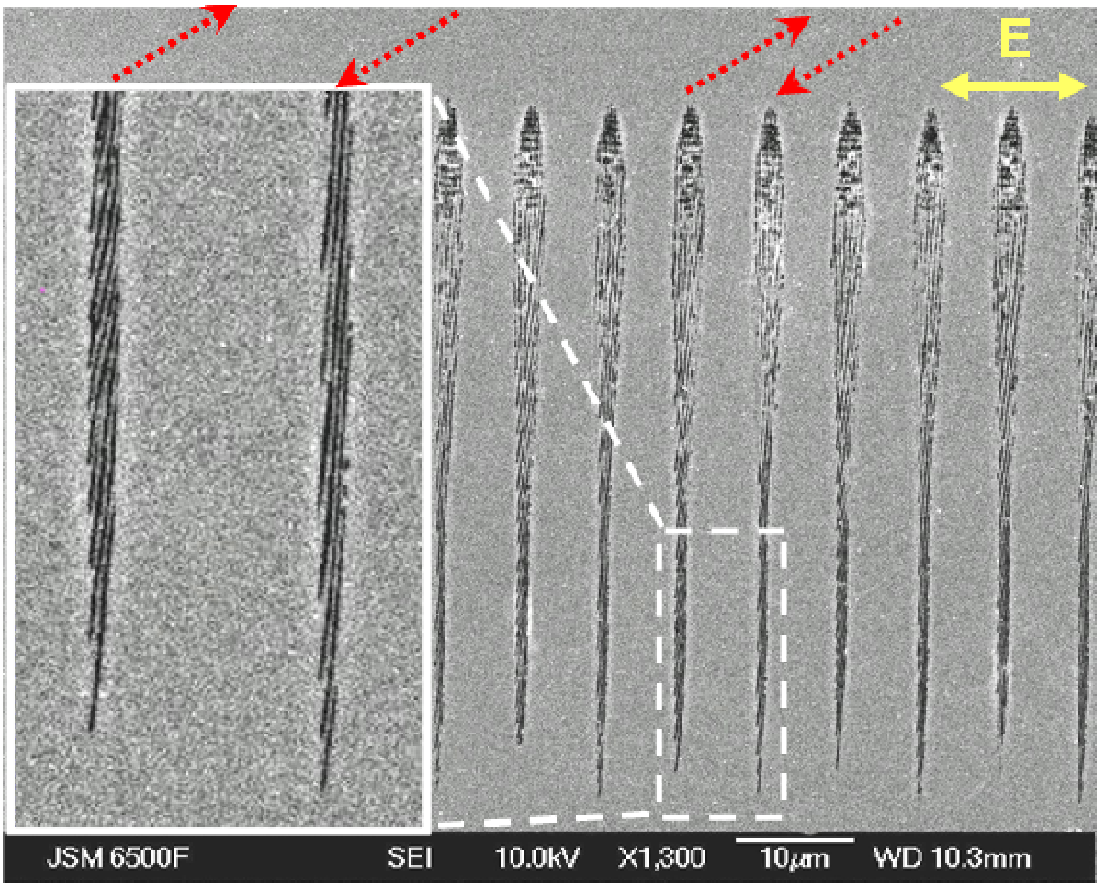

Figure 6.1: SEM images of cross-sections of the structures in glass along the light propagation. The distance between lines is 7 μm. The writing direction is shown as the dotted arrow.

In another experiment, a series of lines were written using an IMRA-FCPA μJewel D-400 amplified ytterbium fiber laser system, operating at 1045 nm, with a pulse duration of 500 fs and repetition rates ranging from 100 kHz to 1 MHz. The high stability of the FCPA laser system is crucial for systematic studies. The polarization of the laser was aligned perpendicular to the writing direction. The lines were written in alternating directions from forward to reverse and using different pulse energies ranging from 0.2 to 1.8 μJ. After writing, microscope images were captured using both crossed-polarized (CP) and Nomarski-DIC illumination (both back-illumination). Composite images were created which show the same portion of each feature using the two illumination techniques. With these composite images, the amount of birefringence visible with the CP illumination (dark part) can be compared with the texture of the feature using the DIC imaging technique (light part). The magnification is 500X (50X objective, 10X eye-piece) and the scale of the features can be gauged based on their 50-μm line separation.

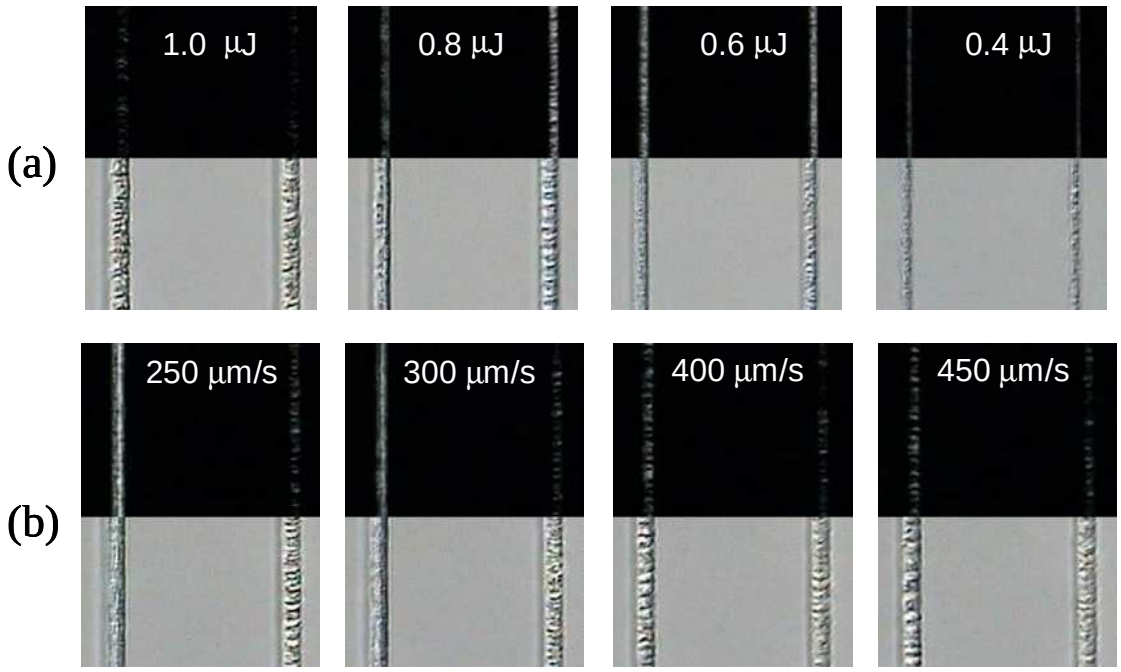

Figure 6.2: Images in crossed polarizers (dark part) and Nomarski-DIC (light part) of the lines written in glass in opposite directions at a repetition rate of 500 kHz (a) with a writing speed of 500 μm/s and different pulse energies and (b) with a pulse energy of 0.9 μJ and at different writing speeds. The distance between lines is 50 μm.

In one of the experiments, groups of lines with alternating writing directions were inscribed. Lines written in both directions at low energies were the same (Fig. 6.2). However, with an increase in energy we observed the appearance of a directional dependence in the written lines, which was strongest at about 0.8-0.9 μJ. The directional dependence is more clearly seen in the birefringence of the lines. This dependence can also be observed in the morphology (texture) of lines written in opposite directions, with a line written in one direction being rougher than a line written in the reverse direction (Fig. 6.2(a)). However, with a further increase of energy above a certain threshold value, both lines become uneven with indications of collateral damage, and the birefringence of the lines disappears as well as the directional dependence. The latter phenomenon can be explained by a cumulative thermal effect [11, 89, 96]. This is supported by the presence of modifications with rough features, much bigger than the spot of the beam, at high repetition rates (500 kHz -1 MHz) and the absence of such features with collateral damage at low repetition rates (below 200 kHz). This agrees with the heat diffusion time of about 4

μs. The dependence of the observed effect on writing speed, near the energy threshold of the disappearance of directional phenomenon, was also tested. It was observed that the directional dependence strengthen at lower writing speeds (Fig. 6.2(b)).

An intriguing result is the observation of *different* textures in the processed material for laser polarizations perpendicular and parallel to the movement of the sample *in one direction* and the *same* textures for two polarizations when writing in the *opposite* direction (Fig. 6.3(a)). The SEM images of the cross-sections of the lines, along the light propagation, revealed a different texture in the lines written in opposite directions (Fig. 6.3(b)). Remarkably, the nanograting of about 300 nm period, which is responsible for the form birefringence of irradiated regions, can be seen only in the initial part of cross-sections of lines written in one of two directions. This small area is followed by one with a collateral damage due to thermal effect, which correlates with a weak birefringence of these lines. It is also observed, that in almost the entire cross-sections of the lines, written in the opposite direction, there is the nanograting along the direction of light polarization with the period of about 250 nm together with the additional periodicity, along the direction of light propagation, of about 720 nm, which is the same value of the wavelength of light in fused silica (λ/n, $\lambda = 1045$ nm, $n = 1.45$) (Fig. 6.3(b)). These lines demonstrate no evidence of the collateral thermal damage and have much stronger birefringence (Fig. 6.3(a)).

Lines written at a repetition rate of 100 kHz also clearly show different textures in opposite directions, without any evidence of collateral damage due to thermal effects. The SEM images reveal the presence of the nanograting in the direction of light polarization almost in the entire cross section for one writing direction and the nanograting, again with additional periodicity along the propagation direction with the value of the wavelength of light, for the opposite writing direction (Fig. 6.4(b)).

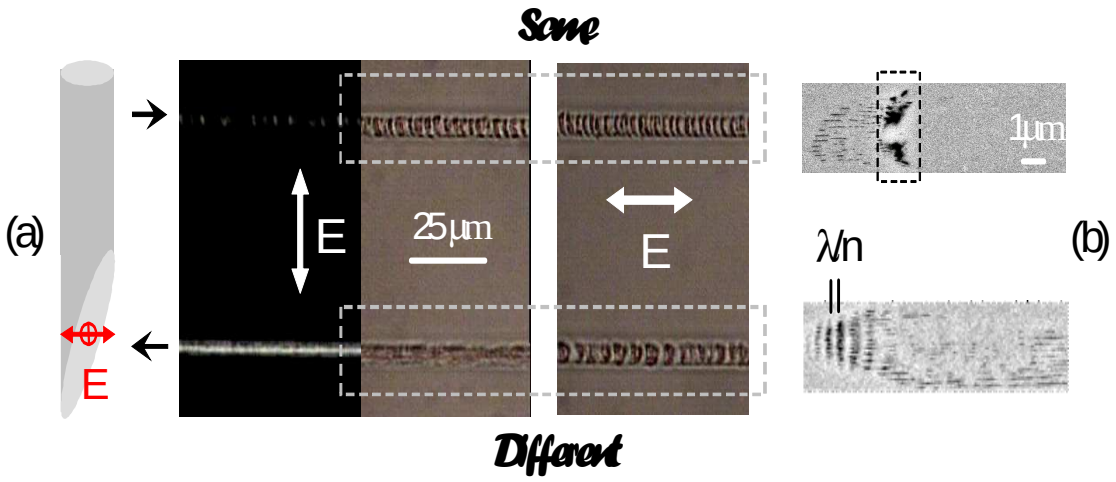

Figure 6.3: (a) Optical microscope images of the lines written with orthogonal polarizations with a 500 kHz repetition rate, a writing speed 250 μm/s and a pulse energy 0.9 μJ. The difference in texture for two polarizations is observed only for one writing direction (dark part). The tilted front of the pulse along writing direction is shown. (b) SEM images of cross-sections of the lines written with the polarization perpendicular to writing direction are also shown. The regions of collateral damage are marked with dashed lines.

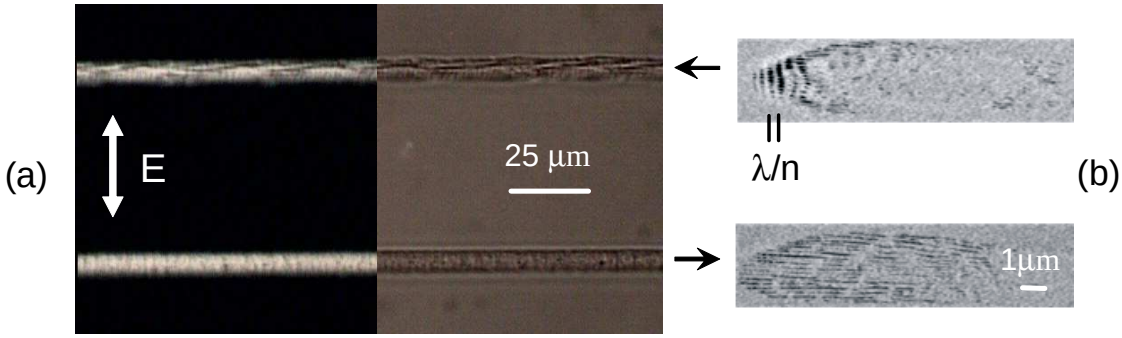

Figure 6.4: Optical microscope (a) and corresponding SEM (b) images of cross sections of the lines written in glass in opposite directions with repetition rate 100 kHz, writing speed 100 μm/s and pulse energy 2 μJ.

6.3 Discussion of the mechanism

The writing anisotropy is observed only at particular pulse energies, which excludes the stage movement as the cause. Inspection of the intensity distribution of the laser beam did not reveal any peculiarities in the shape of the beam, which was close to circular (Gaussian shape). The only possibility left to explain the puzzle of the writing direction anisotropy is related to the anisotropy of the frequency distribution (frequency chirp) in the beam. A spatial frequency chirp and related pulse front tilt is quite common in femtosecond laser systems [98]. Even a small delay across the beam that corresponds to ~ 10% of the pulse duration, results in a pulse tilt as strong as tens of degrees in the vicinity of the focal plane. The pulse front tilt is enhanced in a dispersive media, as in the case of electron plasma close to plasma frequency, which is formed in the focus of the beam due to multiphoton ionization of glass. The pulse front tilt is a tilt in the intensity distribution in the front of the pulse. It is known that, in the presence of intensity gradients, the charges (e.g. electrons) experience the pondermotive force (light pressure), which expels the electrons from the region of high intensity [99, 100]. Indeed, free electrons are affected by a variation of the laser intensity as they quiver in the electric field of the laser pulse. In the non-relativistic case this can be expressed with the fluid equation of motion in an electromagnetic field by

$$\frac{\partial \mathbf{v}}{\partial t} + (\mathbf{v}\cdot\nabla)\mathbf{v} = -\frac{e}{m_e}\left(\mathbf{v}\times\mathbf{B} + \mathbf{E}\right) \tag{6.1}$$

where $\mathbf{v}$ is the electron velocity vector, m_e is the electron mass, e is the electron charge. The ponderomotive force, $\mathbf{F_p}$, and potential, U_p, follow from this equation by time averaging the electric field as:

$$\mathbf{F_p} = -\frac{e^2}{4m_e\omega^2}\nabla E^2 = -\frac{e^2}{2\varepsilon_0 c m_e \omega^2}\nabla I \tag{6.2}$$

$$\mathbf{U_p} = \frac{e^2 I}{2c\varepsilon_0 m_e \omega^2} \tag{6.3}$$

where c is the light speed in vacuum, ε_0 is the permittivity of free space, ω is the frequency of light and I is the light intensity. For very short and relativistic laser pulses, the ponderomotive force can become very important and the resulting acceleration will tend to push electrons in front of the laser pulse, as a kind of “snow-plough” effect [101]. The estimated intensity in the focus of a laser beam in our experiments is of about 3×10^{14} W/cm^2 which will produce ponderomotive potential of 30 eV. This potential is much higher than the energy at room temperature, which is of about 40 meV. Electron plasma in our experiments will still experience this kind of force in front of the pulse. Due to the tilt of the intensity distribution, the force will act on the electron plasma along the direction of the intensity gradient. By moving the beam, the pondermotive force in the front of the pulse will trap and displace the electrons along the direction of movement of the beam only in one direction that corresponds to the tilt in the intensity distribution (we refer to this phenomenon as the “quill effect”). The electron plasma waves, excited in electron plasma, are responsible for the formation of the nanograting [39] and the self-assembled form birefringence [40, 48]. The trapping and displacement of the electrons with the movement of the beam affects the interference of plasma waves, and related form birefringence. The periodic structure, with the period of the wavelength of light observed along the direction of light propagation is created as a result of the interference between plasma waves and the plasma oscillation. Trapping of the electron plasma *damps the plasma oscillation* and related interference producing longitudinal periodic structure with the wavelength of light. The observed difference in the onset of the collateral thermal damage for two writing directions is also the consequence of the anisotropic trapping effect (Fig. 6.3(b)). Further support of the proposed mechanism is the evidence of different textures of modified material for writing with light polarizations parallel and perpendicular to the movement in one of writing directions (Fig. 6.3(a)). This observation is explained by the difference in boundary conditions for the two orthogonal polarizations at the interface of the *tilted pulse front along the writing direction.*

6.4 Changing the direction of tilted pulse front

The directional dependence is explained by anisotropic trapping of the electron plasma by the tilted front of the ultrashort laser pulse. As a result, the pulse front tilt can be used to control material modifications and in particular as a new tool for laser processing and optical manipulation. Based on this idea, the first experiment was carried out using an amplified, mode-locked Ti:sapphire laser operating at 800 nm wavelength with 70 fs pulse duration and a 250 kHz repetition rate. The linearly polarized laser beam was focused via a 50X (NA = 0.8) objective at depth of 60 μm beneath the surface of the fused silica sample. Line structures were written inside the bulk material by translating the sample perpendicularly to the light propagation direction, using a linear motorized stage (Aerotech ALS-130). After irradiation, the sample was inspected using an optical microscope. The first group of lines was written by scanning in alternating directions inside the sample with the pulse energy of 2.6 μJ and the scan speed of 50 μm/s (Fig. 6.5(a)). The temporal characteristic of the pulses, in particular the pulse front tilt before the focusing objective, were characterized using a GRENOUILLE device (8.50 Model) [98]. The measured pulse front tilt for the first group of lines was 4×10^{-2} fs/mm. As shown in (Fig. 6.5(a)), the directional dependence can be clearly observed in the morphology of the lines written in opposite directions, with a line written in one direction being rougher than a line written in the reversed direction. The directional dependence can be also revealed by imaging the lines between crossed polarizers, in which only the smooth lines written in one direction show birefringence. Next the pulse front tilt was reversed by tuning the pulse compressor to the value of -8.64×10^{-2} fs/mm and the second group of lines was imprinted by scanning in alternating directions (Fig. 6.5(b)). After comparing the structures written with the opposite sign of the pulse front tilt, the mirror change in the induced modifications is evident (Figs. 6.5(a) and (b)). This experiment unambiguously demonstrates that the directional dependence of the writing process and the induced modification is determined by the pulse front tilt of the femtosecond laser pulses.

Smooth line structures written in one direction (Fig. 6.5) correspond to type-II modifications with the evidence of form birefringence, while the rough structures

produced by writing in the opposite direction belong to type-III modification with the evidence of a void formation. At pulse energies below the threshold value of 2 μJ, both lines written in opposite directions reveal type 2 modifications. Moreover, when the pulse energy was increased to 3 μJ and above, both lines revealed type-III modifications and the birefringence in the induced structures disappeared. The latter result indicates that the threshold energy for creating type-III modification inside fused silica depends not only on the pulse energy but also on the writing direction. For example, the line structures, written towards the top in Figure 6.5(a), reveal higher threshold energy for the type-III modifications than the structures written in the opposite direction. This threshold dependence reverses when the sign of the pulse front tilt is changed (Fig. 6.5(b)). Furthermore, no directional dependence could be observed when the pulse front tilt was minimized by tuning the pulse compressor.

It should be highlighted that the quill writing effect *depends strongly* on the focusing depth of the laser irradiation under the sample surface. Changing the focusing depth by only 10%, which is from 60 μm to 55 μm or 65 μm, completely eliminated the quill writing effect and produced type 2 or type 3 structures in both directions.

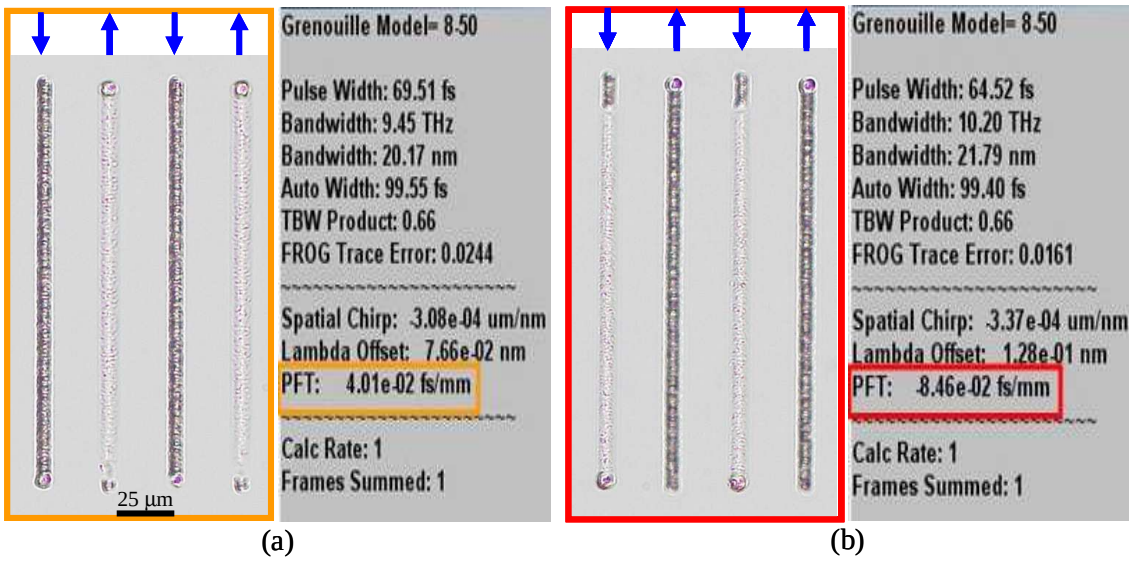

Figure 6.5: Bright field image of the line structures written using pulses with (a) positive pulse front tilt or (b) negative pulse front tilt, arrows indicate writing directions.

An alternative experiment was also carried out to provide additional evidence that the pulse front tilt is responsible for the quill writing effect. A laser source, producing pulses of 150 fs duration at 250 kHz repetition rate and 800 nm, was used in this experiment. The laser beam was focused via a 50X (NA = 0.55) objective at a depth of ~120 μm beneath the surface of the sample. The optimum depth for the quill effect in this experiment was different from the previous one due to the difference in laser beam parameters in the two experiments. The first group of four lines with alternating writing directions was imprinted with the pulse energy of 1.4 μJ and scan speed of 50 μm/s (Fig. 6.6(a)). One additional mirror was added in the setup to reverse the direction of the pulse front tilt before writing the next group of lines (Fig. 6.6(b)). In this writing configuration the second group of four lines was imprinted with all other writing parameters identical to the previous experiment. It was observed that the structural modifications in the lines of the second group were mirrored when compared with the lines of the first group. This result provides further evidence that the pulse front tilt is responsible for the directional dependence in the ultrafast laser writing.

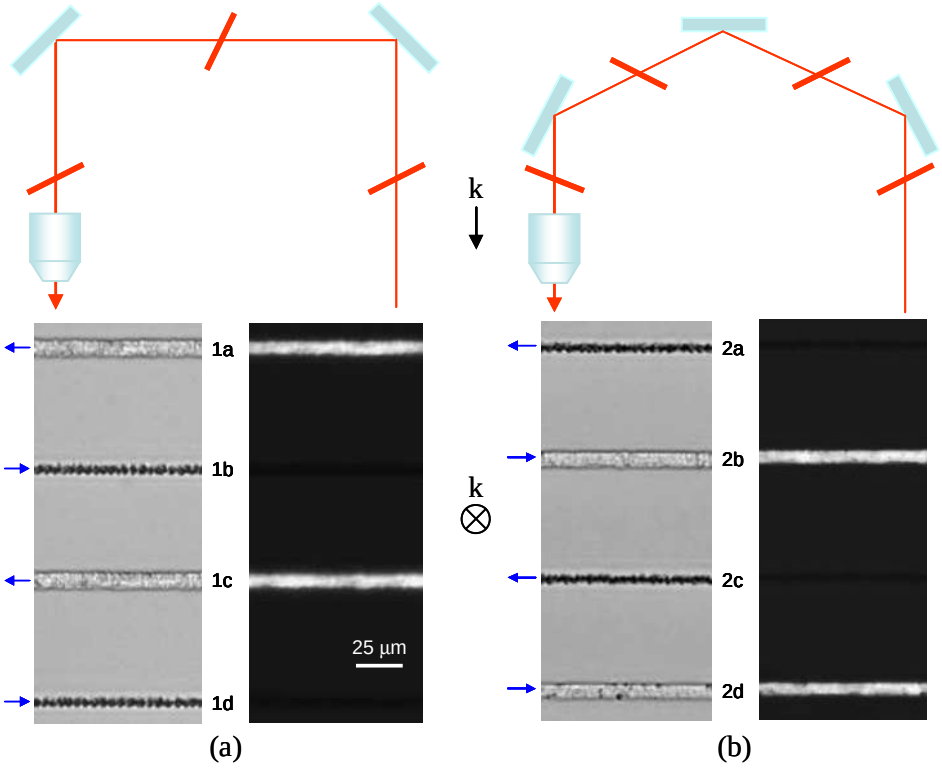

Figure 6.6: Bright field images (light part) and cross polarized images (dark part) of the line structures fabricated with 1.4 μJ pulse energy using (a) two mirrors or (b) three mirrors setup. The pulse front is shown as the bold red line in the schematic diagram of the experimental setup.

We also observed strong white light emission corresponding to type-III structural modifications and a weaker emission corresponding to the nanogratings formation, which were reproducible in different writing experiments (Fig. 6.7). The light reflected from the sample was collected. Supercontinuum generation can be excluded from the explanation of this emission, because the length of light propagation in the focus of high NA objective is too small to produce a significant spectral broadening effect. The observed white emission can be explained by thermal radiation, e.g. bremsstrahlung radiation, emitted by electron plasma which is heated to thousands of degrees at high light intensities of about 10^{14} W/cm^2 [102].

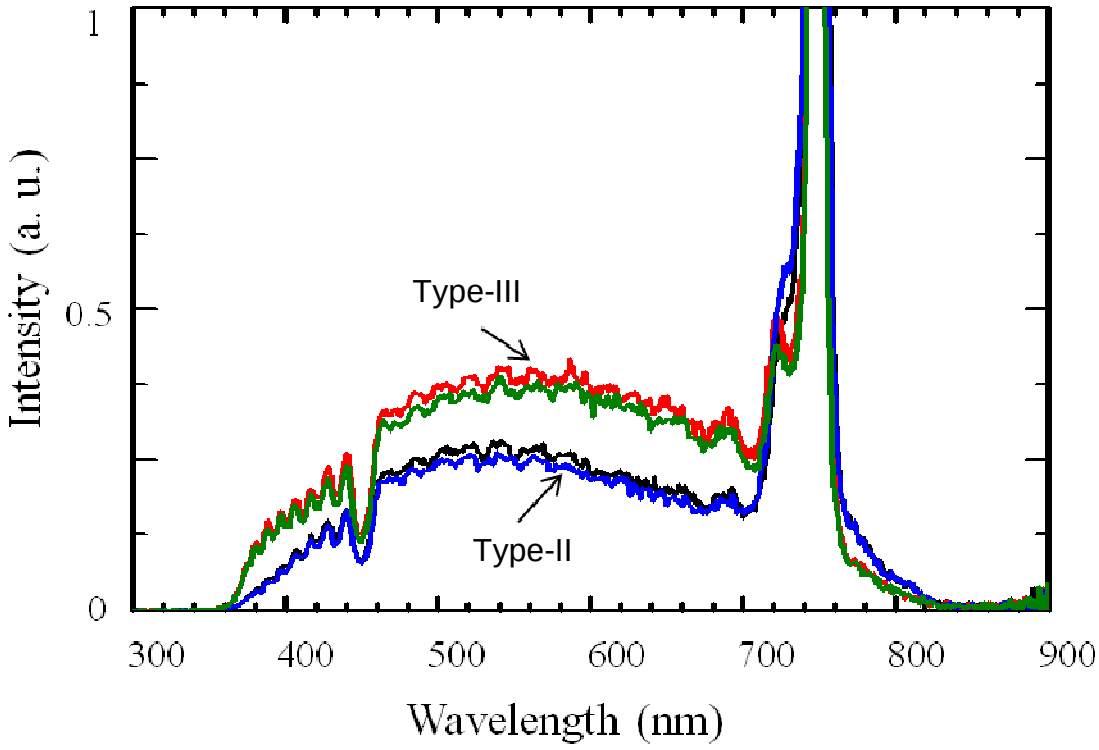

Figure 6.7: Spectra of the white emission collected in reflection during inscription of type-II and type-III structures. The spectra for the type-III structures (red and green curve) were collected during the rougher lines imprinting process as shown in the Fig. 6.5(a)) and the spectra for the type-II structures (black and blue curve) were collected during the smoother lines imprinting process (Fig. 6.5(a)).

6.5 Bubble formation and bubble-nanograting transition

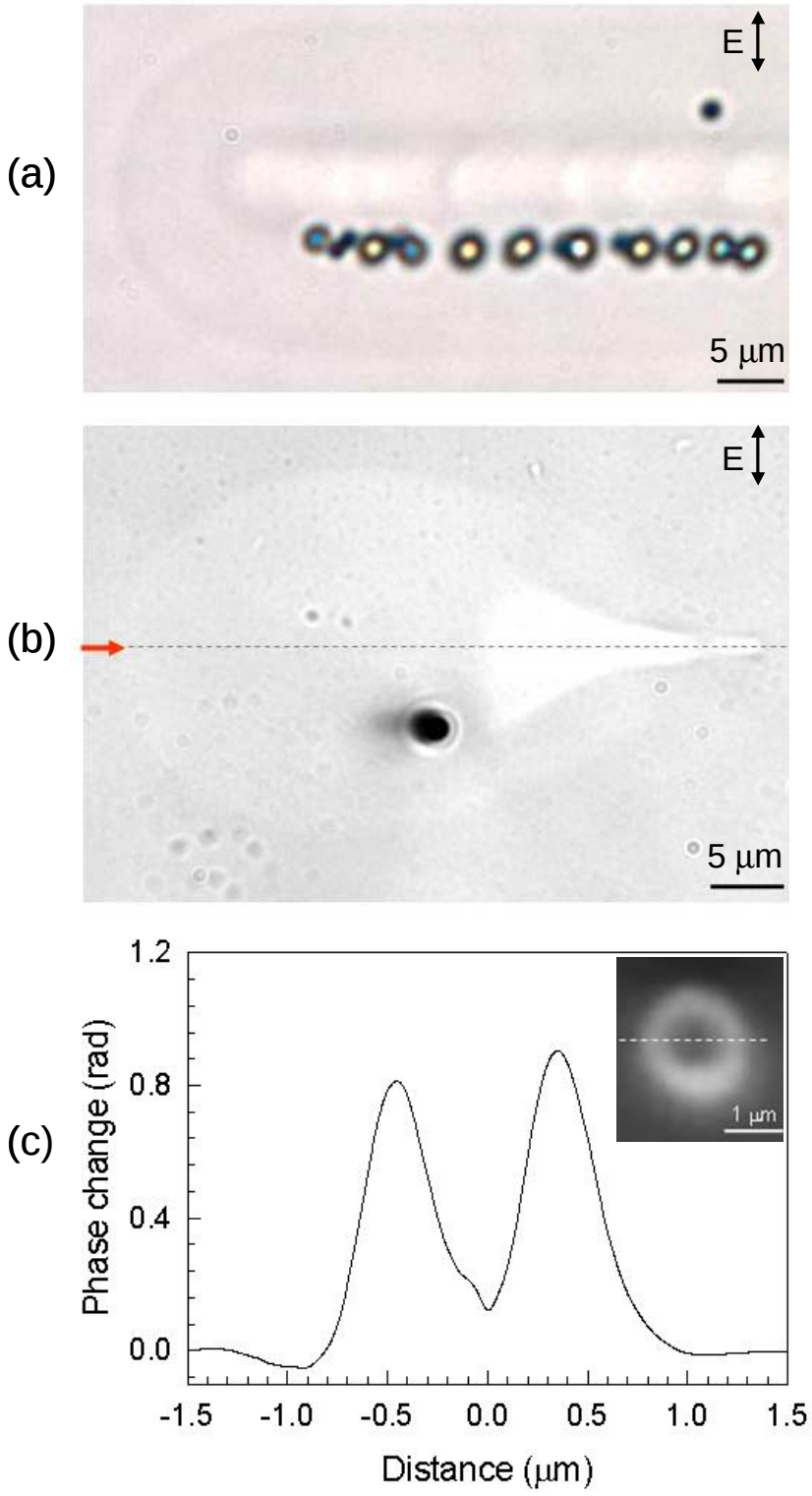

Figure 6.8: Bright field images of the structures fabricated with the pulse energy of 2.4 μJ and scan speed of 50 μm/s. (a) The line structure with the evidence of bubble formation. (b) Cross-section of the line structure with one bubble. (c) Phase profile of the bubble obtained using quantitative phase microscopy technique.

Another intriguing result was the observation of a new type of femtosecond laser induced modification, when the pulse energy was increased to the level of 2.4 μJ (Fig. 6.8). Neither birefringence structures (type-II), nor rough features with evidence of void formation (type-III) could be observed in the modified region. Instead, bubbles with diameters varying from 1 - 3 μm were revealed at the boundary of the irradiated region, which is evident from the cross-sectional image (Fig. 6.8(b)) and a corresponding top view image of the line structure (Fig. 6.8(a)). The color of bubbles visible under white light illumination in the optical microscope (Fig. 6.8(a)) is attributed to the Fabry-Perot effect. The bubbles have a lower refractive index in the centre and a higher refractive index in the surroundings from QPM measurement (Fig. 6.8(c)), which indicated that they are most likely to be voids surrounded by densified material. It is well known that voids (type-III) can be produced on the axis of a focused femtosecond laser beam inside transparent material as a result of a micro-explosion [34]. However in our case, the bubbles are formed not in the region of highest intensity (which is in the centre of a Gaussian beam) but are shifted about 5 μm towards one side of this centre (Figs. 6.8(a), (b)). It should be noted that the movement of bubbles along the direction of writing has been previously demonstrated in fused silica [103]. Surprisingly, in our experiment, the bubbles are shifted perpendicular to the writing direction. In addition, it was observed that bubbles located at both sides of the irradiated region when the writing direction was reversed (Fig. 6.9). The mechanism of anisotropic bubble formation is a puzzle. Bubbles can be formed on the axis of the focused laser beam as a result of micro-explosion and subsequently move from the molten centre to the boundary of irradiated region. Alternatively, they can be formed directly at the boundary region of a light affected zone, where tensile stress causes the formation of cavitation bubbles when the rupture strength in molten glass is exceeded [104]. Clarification of the phenomenon’s mechanism needs further investigation. However, we believe that the light pressure at the tilted front of the pulse could be responsible for the asymmetry of bubble formation and its dependence on writing direction.

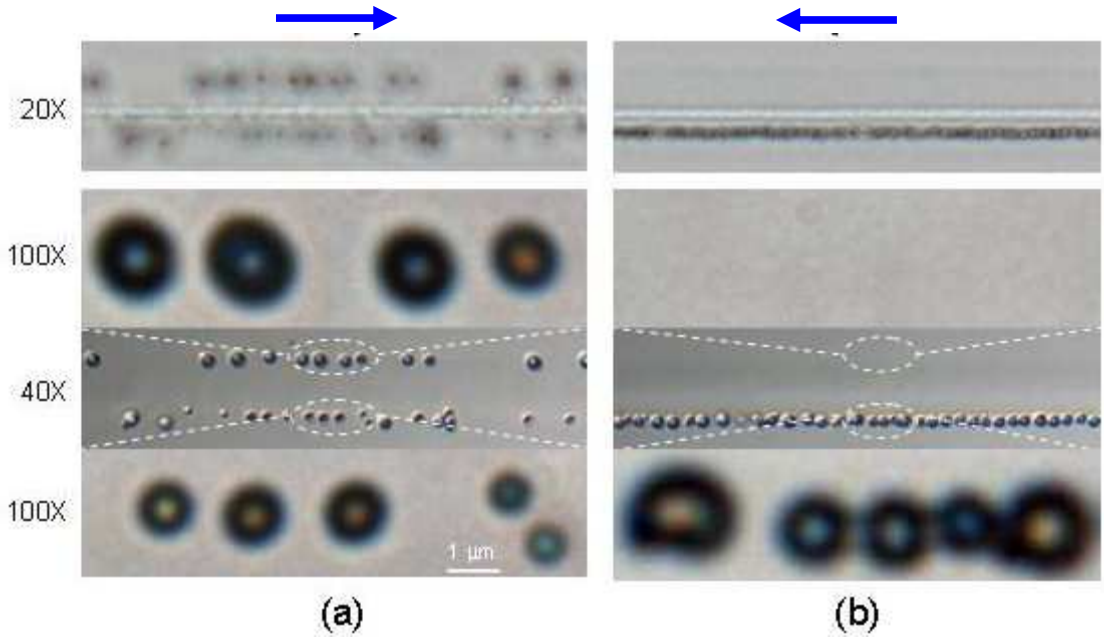

Figure 6.9: Microscope bright field images with different magnifications of the line structures fabricated in opposite directions (a) and (b) at 2.4 µJ pulse energy.

Another interesting observation was an unusual transition from the regime of bubble formation to self-assembled form birefringence which occurred during the continuous writing process (Fig. 6.10). The phenomenon revealed itself as follows during single line writing. Firstly, bubbles began to appear almost from the start of writing process. However, at a certain distance, typically about 500 µm from the start of writing, the formation of bubbles abruptly terminated. Instead the modification with the evidence of form birefringence appeared and continued till the end of line writing process. The transformation in the type of modification was correlated with the change in intensity of white light emission during the inscription process (Fig. 6.10(c)), which was similar to the emission described above (Fig. 6.7). The emission light was collected along the laser propagation direction after the sample using a highly multimode fibre with 0.5 mm diameter. Strong white light emission during the bubble formation dropped at the modification transition and only weak emission could be observed during the formation of birefringent structures. It should be noted that all writing parameters, including the pulse energy and scanning speed, were kept constant during the encryption process and the phenomenon could be repeated in different areas of the sample. However there is one parameter which is not constant, in particular the temperature of the whole glass sample, which could increase as a result of light absorption during the writing process. It should be noted that self-assembled form

birefringence structures and related nanogratings disappear at temperatures above the glass transition temperature [47].

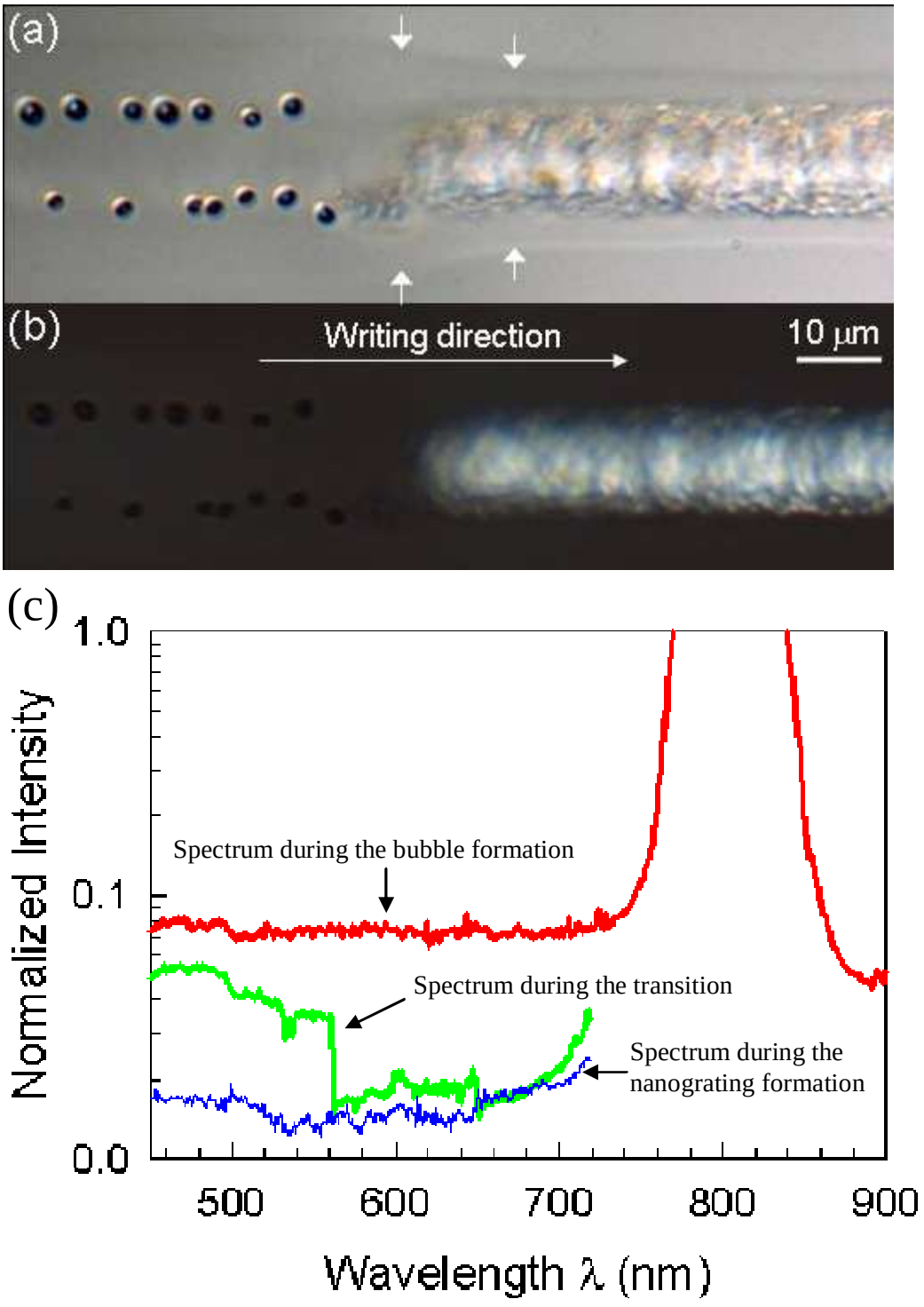

Figure 6.10: (a) Bright field image of the transition region. (b) Cross polarized image of the transition region. (c) Spectrum collected during the writing process.

This indicates that local temperature in the irradiated region should drop at modification transition from the glass melting temperature (1715 ^{0}C), corresponding to the bubble formation, to the temperature below the glass transition temperature (1175 ^{0}C), corresponding to the nanograting formation. This local temperature decrease can be explained by an increase of the heat capacity caused by the heating of the whole glass sample.[20] Indeed, given that $\Delta T = \Delta Q/mc_p$, where ΔT is the temperature difference, ΔQ is the heat energy and m is the mass of the substance, c_p is the heat capacity, the temperature drops when heat capacity increases. The nanogratings start to form once the local temperature has dropped below the glass transition temperature. The energy is consumed by a nanograting formation process which locks temperature below the glass transition temperature and explains why formation of nanogratings does not stop till the end of writing process.

6.6 Conclusions

In conclusion, it is remarkable that a laser beam, one of the most modern writing tools, could be used for calligraphic inscription similar to writing with a quill pen, which is based on the anisotropy of a quill’s tip shape. Moreover, modifications of materials by light span from photosynthesis and photography to material processing and laser writing and there are only a few parameters of the light beam which control material transformations, in particular wavelength, intensity, exposure time and pulse duration. Our results add one more parameter to this list – direction of beam movement or pulse front tilt. A change in structural modification was demonstrated in silica glass sample by controlling the direction of pulse front tilt, achieving a calligraphic style of laser writing which is similar in appearance to that inked with the bygone quill pen. Moreover a new type of modification associated with anisotropic bubble formation, which could be controlled by writing direction, was observed at high pulse energies. The phenomenon of modification transition in a continuous encryption process was observed. We anticipate that possibility of achieving control of light-matter interactions by adjusting the tilt of ultrashort pulse front will open new opportunities in material processing, optical manipulation and data storage.

Chapter 7

Stress birefringence induced in chalcogenide glass

7.1 Introduction

The results presented in Chapter 5 show that self-assembled nanostructures, within the irradiated volume, are responsible for the femtosecond laser induced type-II modifications which are characterized by anisotropic scattering, anisotropic reflection, average negative index change and form birefringence. In addition, the orientation of the nanostructures and the subsequent optical axes of form birefringence can be controlled by the polarization direction of the writing laser. This type of femtosecond laser imprinted structures has only been observed in a limited number of materials, including fused silica glass and TeO_2 crystal. In an attempt to clarify the reason for the non-appearance of self-assembled nanostructures in other optical materials, we carried out experiments in chalcogenide glasses.

Chalcogenide glasses contain a chalcogen element (sulphur, selenium or tellurium) as a substantial constituent. These glasses are characterized by longer wavelength IR transmission and high refractive indexes. Moreover, chalcogenide glasses can be doped by rare-earth elements, such as Er, Nd, Pr, etc., and hence numerous applications of active optical devices have been proposed [105-108]. Chalcogenide glasses possess high photosensitivity and show a variety of photoinduced effects including photodarkening, photobleaching, photocrystallisation and photoinduced anisotropy [109]. These effects may be dynamic (only present during optical excitation) or metastable (remaining after illumination). Furthermore, they may be irreversible or reversible. Finally, the changes may be scalar in nature (independent of the polarization of the inducing light) or vectoral (dependent on the polarization), leading to optically modified isotropic or anisotropic behaviour respectively [110]. Photoinduced anisotropy in chalocogenide glass has aroused considerable interests in

recent years [70, 71, 110-115]. The phenomenon refers to the observations that chalcogenide glasses exhibit optical anisotropies when exposed to linearly polarized light. In addition, the anisotropic principle axis can be tuned by changing the polarization direction of the exposing light. Furthermore, the photoinduced anisotropy can be erased with annealing. The photoinduced anisotropy origin from the fact that the dielectric tensor of the chalcogenide sample irradiated by linearly polarized light becomes an ellipsoid of revolution with the principal axis parallel to the electric vector of the light [111].

In this chapter, birefringent modification is demonstrated in the chalcogenide glass by femtosecond laser direct writing. Unlike the previously reported photoinduced anisotropy in chalcogenide glass [70, 71] and form birefringence in fused silica [39, 40], the optical axes of the birefringent region are not determined by the polarization direction of the irradiating light. Instead, by varying the scanning direction of the laser irradiation, the optical axes of the birefringence can be changed. As a result, the information on the direction of writing could be recorded inside transparent materials. Moreover, this type of photoinduced anisotropy can be erased by annealing, and is reversible by repeatable scanning.

7.2 Femtosecond laser induced stress birefringence in chalcogenide glass

The chalcogenide glass sample is germanium sulfur glass ($Ge_{25}S_{75}$) having a nominal composition of 25Ge-75S (mol %), which is a promising material for nonlinear optical and optical amplifier applications [108]. Using the laser system described in Sec. 3.1, the linearly polarized laser beam was focused via a 50X (NA=0.55) objective at a depth of ~200 μm beneath the surface of the sample. Line structures were written inside the bulk material by translating the sample perpendicularly to the light propagation direction, using a linear motorized stage (Aerotech ALS-130). The scan speed was 200 μm/s.

A group of lines was written with various pulse energies ranging from 0.1 μJ to 0.6 μJ (Fig. 7.1 (a)). The width of the imprinted structure increases rapidly with the pulse energy. Moreover, the width of the modified region reaches 50 μm when the pulse energy increases to the value of 0.6 μJ, which is significantly larger than the diameter of the focused beam of ~2 μm (Fig. 7.1(a)). This indicates that thermal effects can be responsible for the structural modification in the region surrounding the exposed area. Quantitative phase microscopy was used to characterize the phase change of the line structure (Fig. 7.1(b)). A central dip region shows a negative phase change ($\Delta\phi$), whereas the surrounding regions have a positive phase change. The observation indicates that femtosecond laser irradiation results in a negative Δn of the central exposed region and a positive Δn of the surrounding region. Densification created as a result of the thermal expansion of the material at the focus of the writing laser beam can account for the positive Δn of the surrounding region. The modified regions also show birefringence that can be visualised by imaging the sample between two crossed polarizers. Quantitative birefringence microscopy (Abrio system) was also utilized to measure the retardance ($R = \Delta n.d$) and identify the optical axis (slow axis) of the birefringent modification. The retardance of the birefringent region ($R = \Delta nd$) increases with the pulse energy of the writing laser (Fig. 7.1(c)). Furthermore, it was surprising to observe that the optical axis of the left part and the right part of the birefringent line structure is different (Fig. 7.1(c)). Indeed, a "U" shape of the slow axis orientation in the birefringent line structure was revealed (Fig. 7.1(d)). A "U" shape of modification can be normally observed in the line structures in fused silica written with femtosecond laser irradiation (Fig. 7.1(e)). IMRA fiber laser system, operating at 400 fs pulse duration, 500 kHz repetition rate, 1045 nm and 0.93 μJ, was used for writing the line structures in fused silica. The scan speed was 400 μm/s and the writing direction is shown with the arrow (Fig. 7.1(e)). The thermal expansion and subsequent cooling can account for this type of "U" shape of modification in fused silica, similar to the structural modification routinely observed during laser welding.

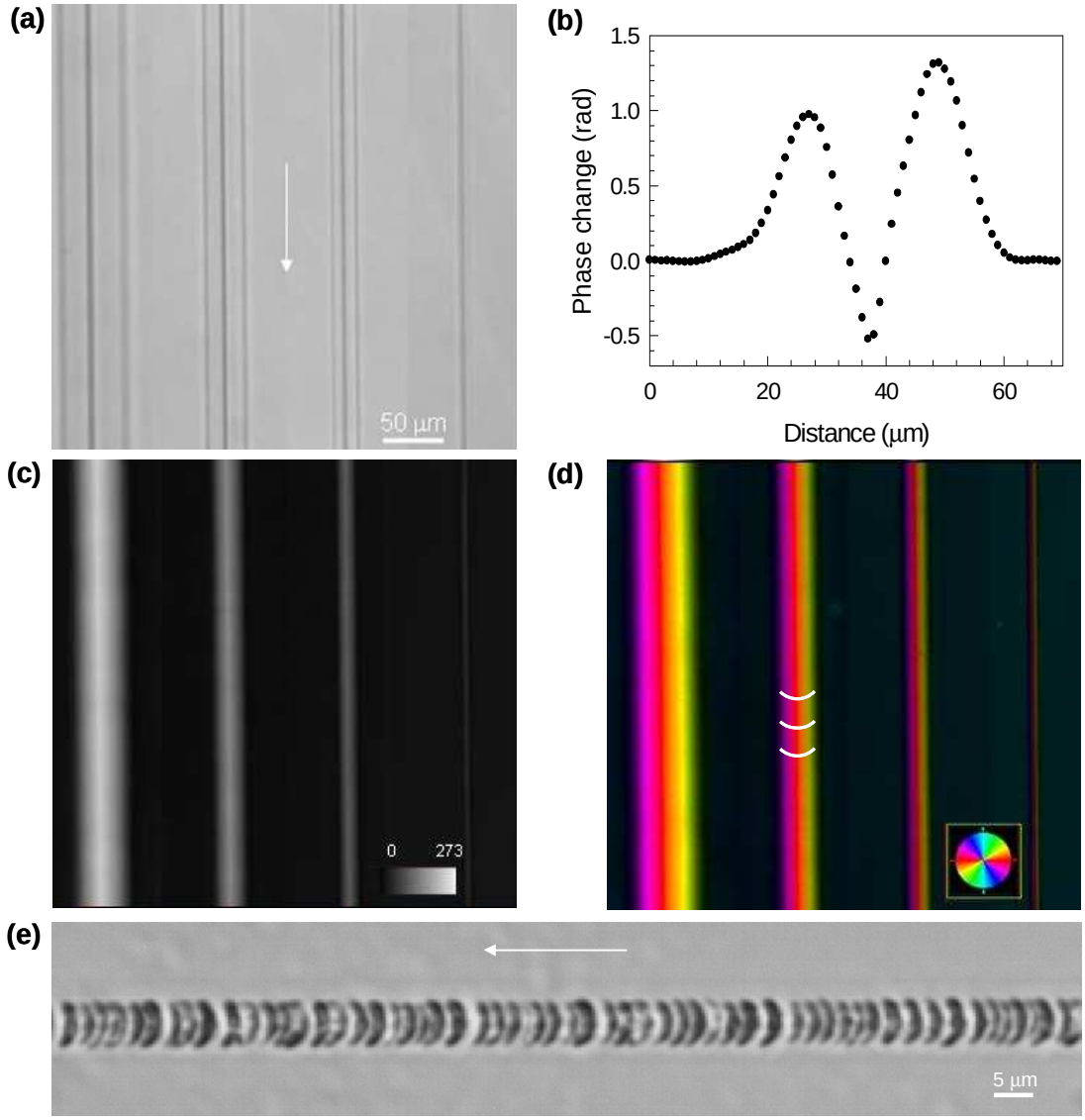

Figure 7.1: (a): Microscope image of the line structures. (b): Phase change profile of the line structure. (c,d): Quantitative birefringence measurement of the line structures, the retardation was measured in (c), and the slow axis is revealed in (d). (e): Microscope image of the line structure written in fused silica.

The "U" shape of the slow axis orientation in the chalcogenide glass was also visualized by positioning the line structures between two linear polarizers, oriented 45^0, and viewed under an optical microscope in transmission mode (Fig. 7.2). An asymmetry of transmitted light through the left part and right part of the modified region was observed (Figs. 7.2(c), (d)). This left-right asymmetry indicates that the polarization of light, passing through the modified region, rotates in opposite directions on the two sides from the center of the region.

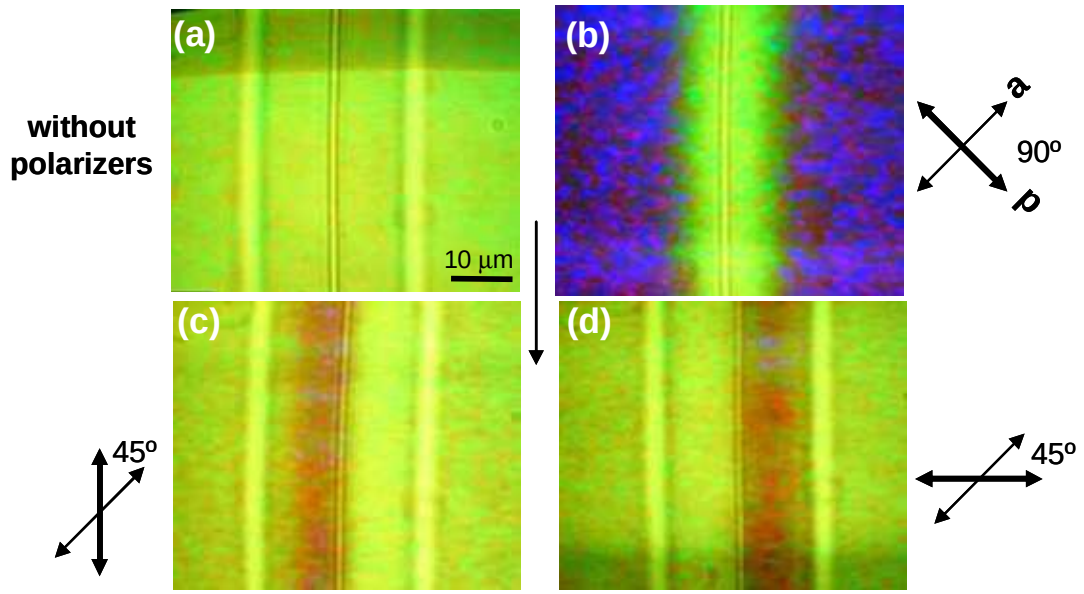

Figure 7.2: Microscope images of modified regions: without polarizers (a), with crossed polarizers (b) with polarizer and analyzer oriented with the angle of 45^0 (c) and -45^0 (d). p: polarizer, a: analyzer.

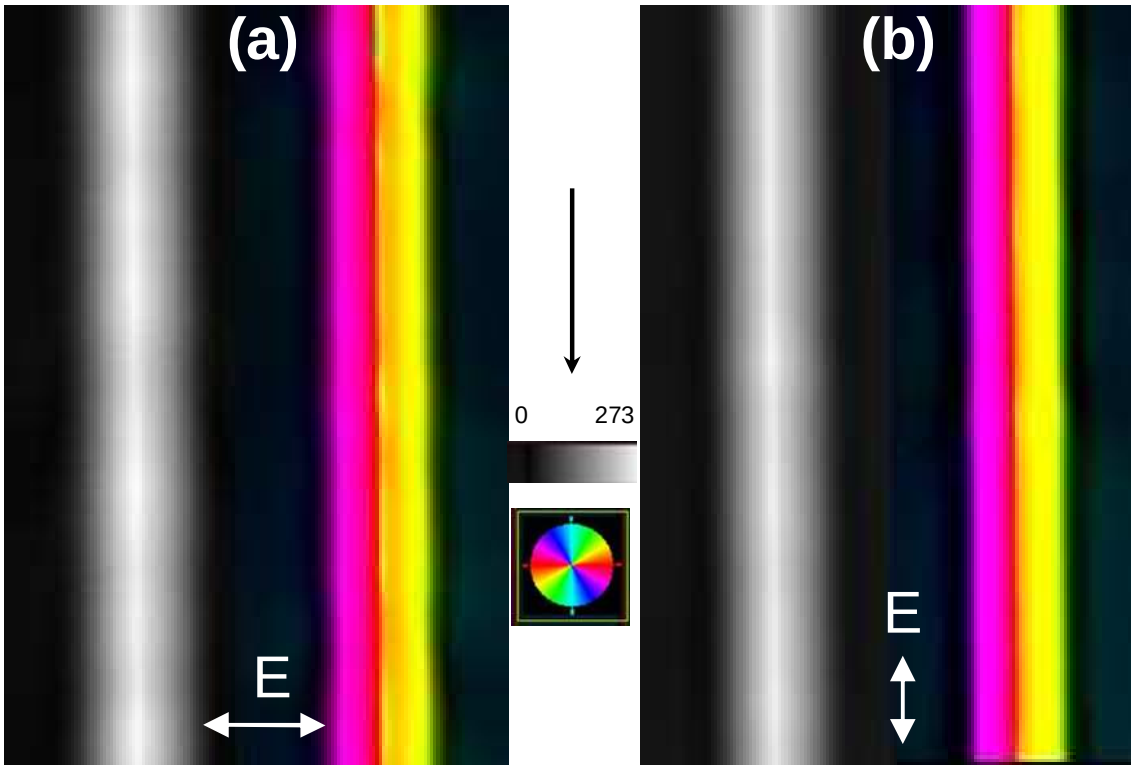

Figure 7.3: Quantitative birefringence measurement of the femtosecond laser induced modifications: with the polarization direction of the writing laser perpendicular to the line (a) and parallel to the line (b).Quantitative birefringence measurement of the femtosecond laser induced modifications: with the polarization direction of the writing laser perpendicular to the line (a) and parallel to the line (b). E: Polarization direction of the writing laser; the scan direction is shown as the black arrow; the width of the line is 30 µm.

It was mentioned in Chapter 5 that, above a certain intensity threshold, form birefringence (type-II) can be induced inside the fused silica glass. The form birefringence is created as a result of self-assembled nanostructures inside the focal region and the optic axis of form birefringence, induced in fused silica, can be controlled by the polarization direction of the writing laser beam. Moreover, it was reported that linearly polarized light can induce anisotropy in chalcogenide glass and the axes defining the optical anisotropy can be tuned by changing the polarization direction of the exposing light. However, unlike the previously mentioned type-II modification in fused silica [40] and photoinduced anisotropy in chalocogenide glass [70, 112]; in our case, the optic axis of the birefringent region does not change when the writing laser polarization direction is varied (Fig. 7.3). This demonstrates that the birefringence of the modifications imprinted in chalcogenide glass by femtosecond laser direct writing is different from the form birefringence induced in fused silica and that the optical axes of the birefringent region are not controlled by the polarization direction of the writing laser.

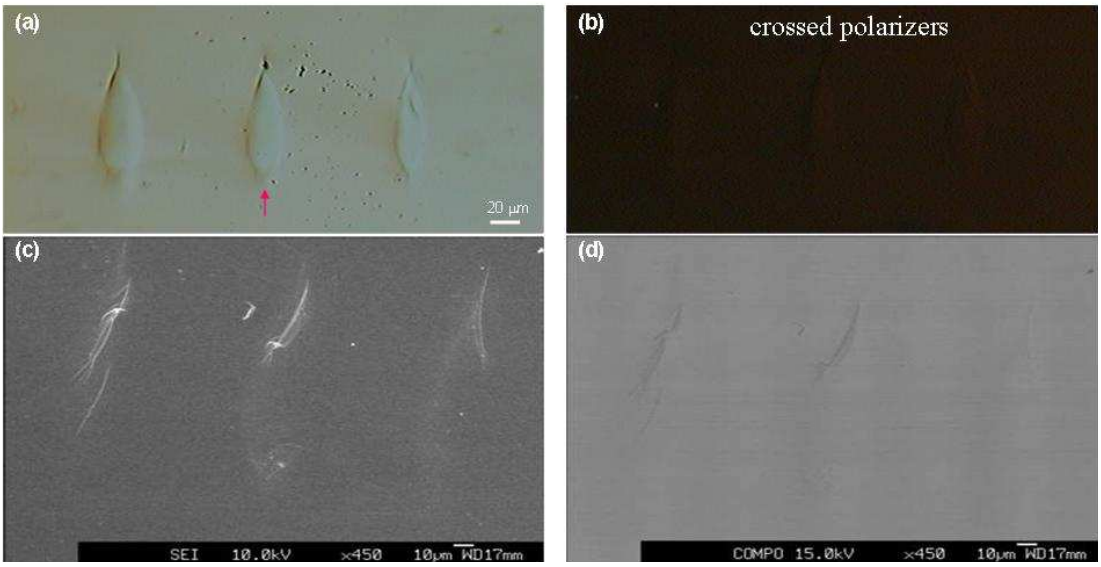

Figure 7.4: Microscope images of the cross-section of the line structures without polarizers (a) and with crossed polarizers (b). (c): Second electron image of the cross-section of the line structures. (d): Back scattering image of the cross-section of the line structures. The laser was propagating from the bottom of the image, shown as the red arrow.

A microscope image of the cross-section of the line structures is shown in Fig. 7.4 (a) and its corresponding view under cross-polarizers is revealed in Fig. 7.4 (b). No birefringence can be observed in the cross-sectional image of the line structure, indicating that no nanostructures were formed in the focal volume of the exposed region. This was further confirmed by imaging the modified region using SEM (Figs. 7.4(c), (d)).

Indeed another type of birefringence, namely stress birefringence induced by the photoelastic effect, can account for this type of birefringence of the modified region in chalcogenide glass. For stress birefringence, the relation between the retardance (R) and stress (σ) is defined as:

$$R = C_{pe} \cdot \sigma \cdot d \tag{7.1}$$

where C_{pe} is the photoelastic coefficient, d is the thickness of the birefringent region. The stress is mainly induced from the light induced thermal expansion. With the similar laser irradiation conditions producing the same amount of stress, the retardation should increase with increasing the photoelastic coefficient. Based on this idea, various glass samples with different photoelastic coefficients were irradiated using similar laser irradiation conditions. As shown in Fig. 7.5, compared to chalcogenide glass, the exposed regions show a much weaker birefringence in borate glass, with the C_{pe} reduced to the value of 4.35 x 10^{-12} Pa^{-1}. In phosphate glass, with a C_{pe} value of 0.42 x 10^{-12} Pa^{-1}, which is about 50 times smaller than the value in chalcogenide glass, no birefringence is observed.

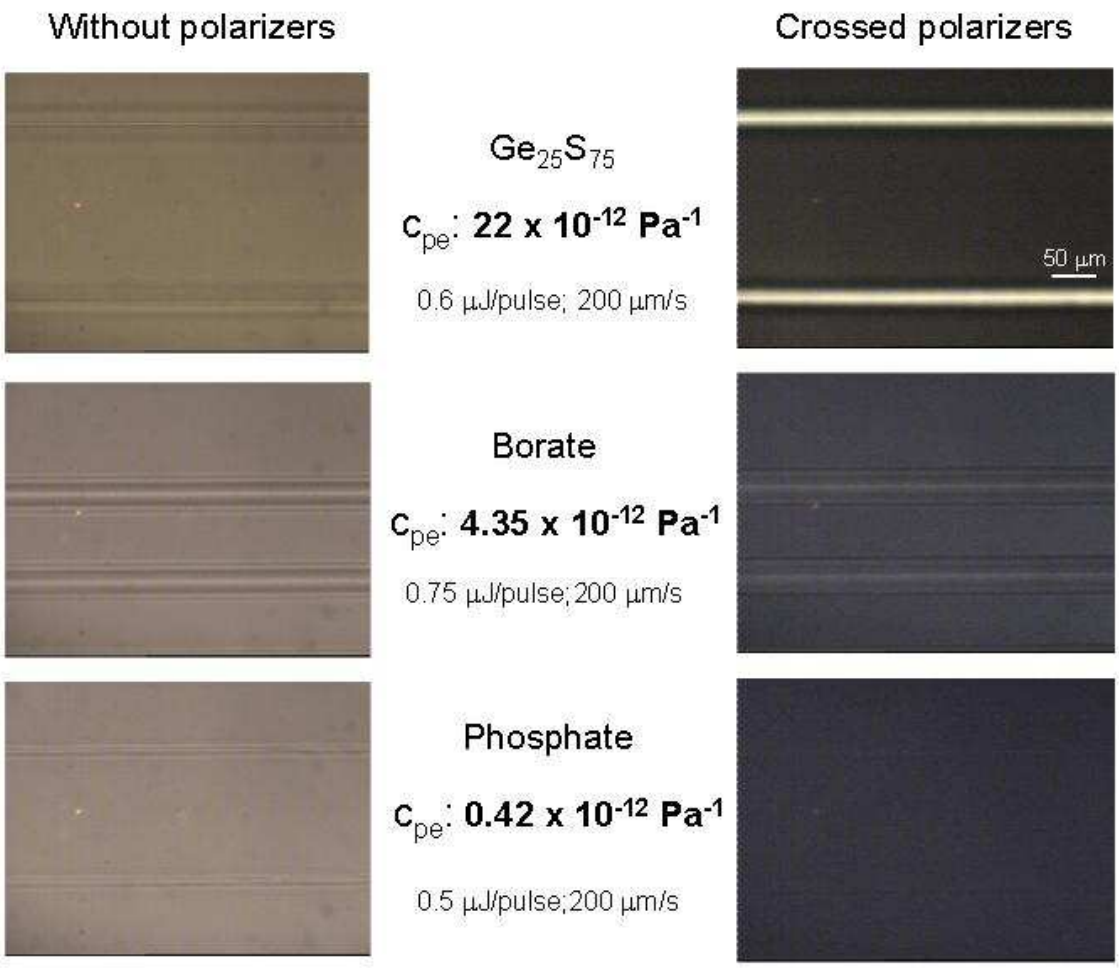

Figure 7.5: Microscope images of the femtosecond laser induced line structures inside chalcogenide, borate and phosphate glass respectively. The left part images are taken without polarizers and the right part images are taken with crossed polarizers.

7.3 Stress annealing

It is well known that the stress can be removed from glass by annealing at the transition temperature. In annealing experiment, the chalcogenide sample with imprinted structures was heated at a rate of 2 ^{0}C per minute, kept at 100 ^{0}C for one hour and then cooled to room temperature at 2 ^{0}C per minute. This treatment was then repeated at 200 ^{0}C, 240 ^{0}C, 280 ^{0}C, and after each annealing step the retardance was measured. It is observed that the retardance was unaltered up to 100 ^{0}C and start to decrease at higher temperature (Figure 7.6).

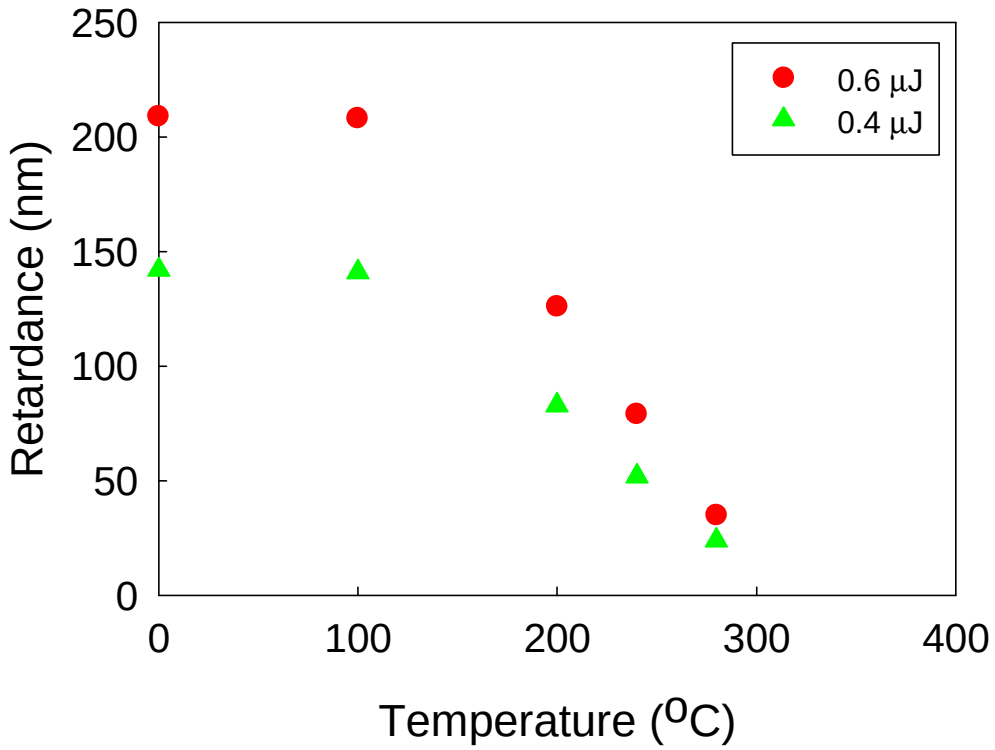

Figure 7.6: Measured retardance of the line structure versus the annealing temperature in the chalcogenide sample. The red dots are the measurements for the line structures written with 0.6 µJ and the green dots are the measurements for the line structures written with 0.4 µJ.

The retardance becomes zero when the temperature was increased to 310 ^{0}C, slightly above the glass transition temperature (305 ^{0}C). This experiment unambiguously demonstrates that the birefringence induced inside the chalcogenide glass by femtosecond laser irradiation is related to stress birefringence.

7.4 Directional dependence of the birefringent modification

It was mentioned previously, in Chapter 6, that different types of modifications can be induced inside fused silica by reversing the writing direction. The directional dependence of modification was interpreted in terms of anisotropic trapping of electron plasma by an ultrashort laser pulse with tilted front. Here, we also observed a directional dependence of modification in chalcogenide glass. Different left-right

asymmetries for the structures written in two opposite directions were revealed in Figs 7.7(a-b), which were the mirror images of each other. It was observed that the orientations of the optical axes in the left and the right part of the modified region were different. Moreover, their orientations are also dependent on the writing direction (Fig 7.7 (d)). Unlike previously reported directional dependence of modification in fused silica, where different types of modifications were imprinted in opposite writing directions. Here, the same type of birefringent modification was induced inside the chalcogenide glass in reversed writing directions (Fig 7.7 (c)). However, the "U" shape of slow axis orientation reversed when the line structure was written in the opposite direction (Fig. 7.1(d)). Similar "U" shape of structural modification and its dependence on the writing direction can also be observed in the line structures imprinted in the fused silica (Fig. 7.7(e)). The thermal expansion and subsequent cooling accounted for this kind of mirrored structural modifications in two writing directions observed in fused silica, which is different from the "quill" writing effect discussed in Chapter 6.

We also carried out experiment on the rewriting line structure in $Ge_{25}S_{75}$ sample. A line structure with double scanning was imaged using the Abrio system and its optical axis was shown in Fig. 7.7(f). The first scan direction was from the left to the right and across the whole line region in Fig. 7.7(f). After that, the second scan was started from right to left as illustrated in Fig. 7.7(f) and the scanning was finished in the middle of the previously written line structure. It is shown that optical axis of the double scanned region is defined by the second writing direction (Fig. 7.7(f)). This demonstrates that the information on the direction of writing can be recorded and be rewritable in chalcogenide glass.

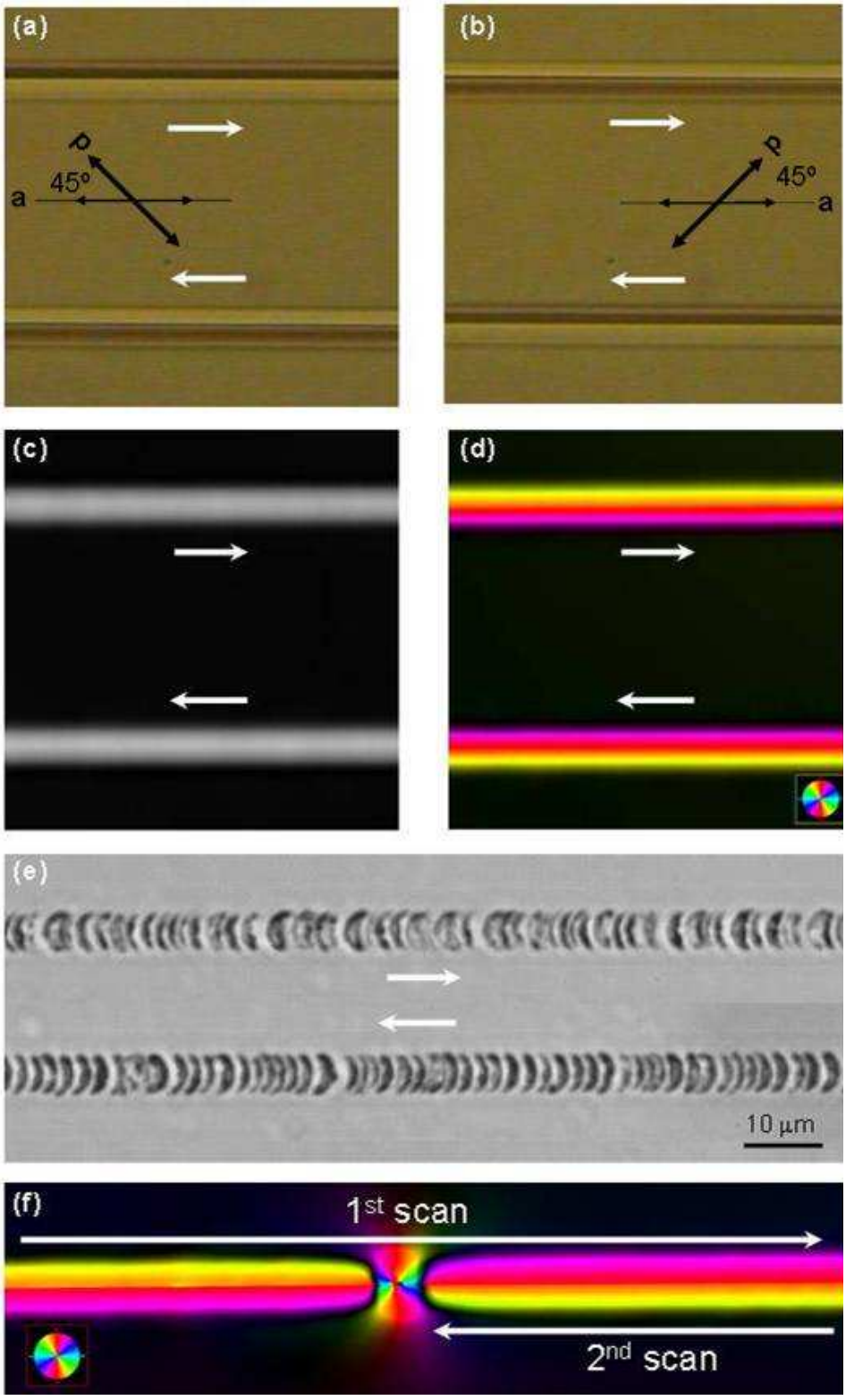

Figure 7.7: (a, b): Microscope images of the line structures written in two opposite directions using polarizers crossed with the angle of 45^0 (a) and -45^0 (b). (c, d): Quantitative birefringence measurement of the line structures written in two opposite directions, the retardation was measured in (c), and the slow axis is revealed in (d). (e): Microscope image of the line structures written in fused silica, the writing condition is the same as the one in Fig. 7.1(d). (f): Quantitative birefringence measurement of the line structure by double scanning.

7.5 Circular birefringence

In another experiment, a square structure was written inside the $Ge_{25}S_{75}$ sample. The pulse energy of the writing laser is 0.6 μJ and the scan speed is 200 μm/s. The sample was then placed between two polarizers crossed at 45^0 and imaged using an optical microscope in transmission. As expected, mirror symmetry of the structures written in opposite directions was observed (Fig. 7.8(a)). However, with a simple linear birefringence model, illustrated in Fig. 7.8(b), we can not explain the left-right asymmetry between adjacent lines written in orthogonal direction (line I and line II). The polarization direction of the transmitted light from the birefringent region should rotate towards optical axis in this model. Since the orientation of the optical axis in region 1 and region 4 (Fig. 7.8(b)) is in the same direction, the transmitted light from these two regions should has the same colour and intensity between crossed polarizers, same as the region 2 and region 3 (Fig. 7.8(a)). However, a different result was revealed in our experiment. The polarization direction of the transmitted light from the inner part of the square structure rotates in one direction regardless of writing direction. In contrast, the one transmitted from the outer part rotates in another direction. We believe such phenomenon could be explained by the circular birefringence induced in the modified region, similar to the twist nematic effect in liquid crystals (Fig 7.9(b)). A cross-sectional image of the line structure along the light propagation direction is shown in Fig. 7.9(a). Due to the carrot shape of the cross-section, the optic axis in each plane, perpendicular to the light propagation direction, will be slightly twisted (Fig. 9(a)). Moreover, the twist of the optical axis from the left part and the right part of the structure is in the opposite direction. As a result, the polarization of light, passing through the modified region 1 and region 3 (or through the modified region 2 and region 4) rotates in the same direction following the twist of the optic axis.

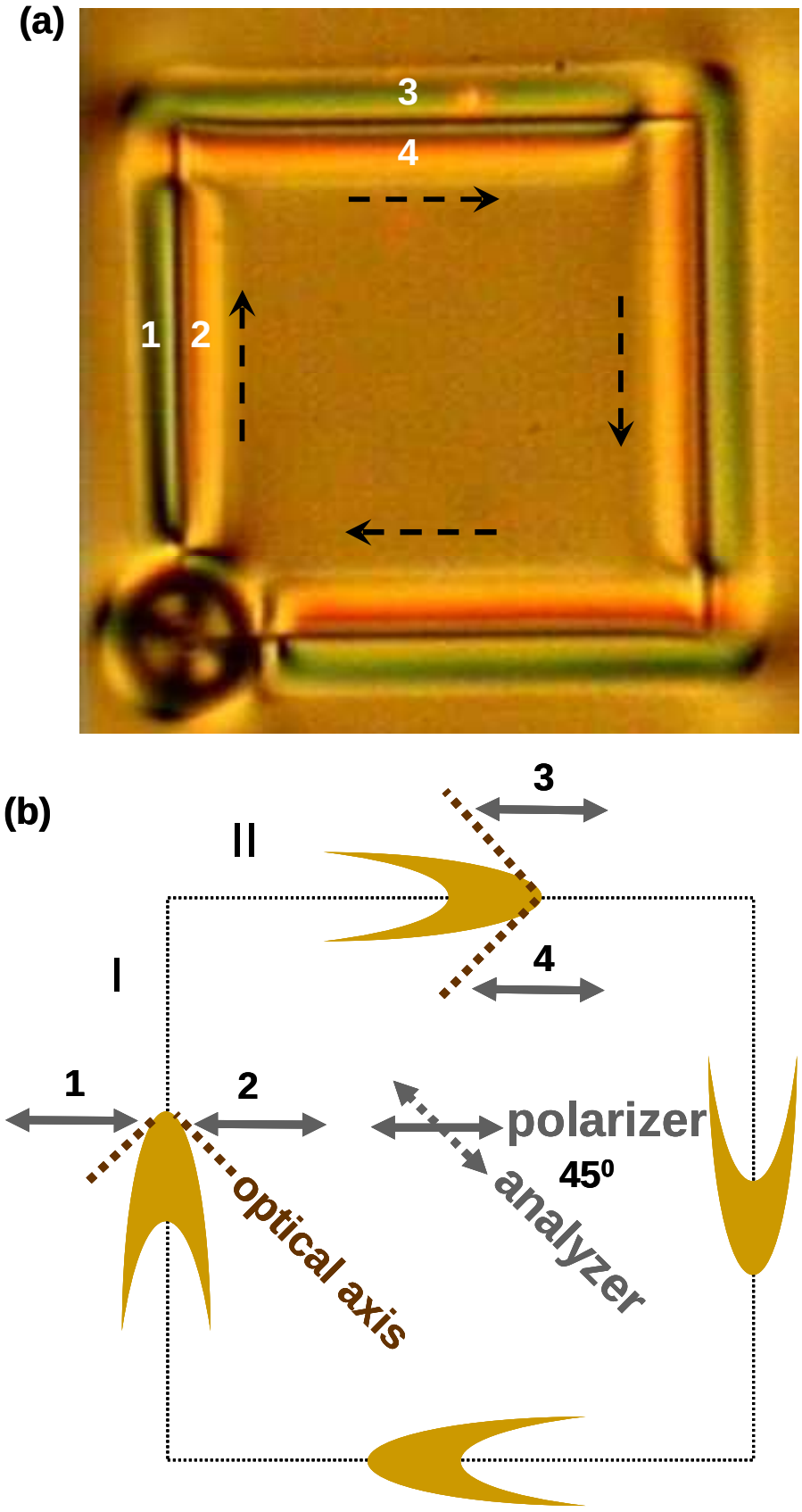

Figure 7.8: (a) microscope image of a square pattern written in chalcogenide glass using femtosecond laser direct writing. The image was taken with polarizer and analyzer oriented at 45^0. (b) Linear birefringence model of the modified region.

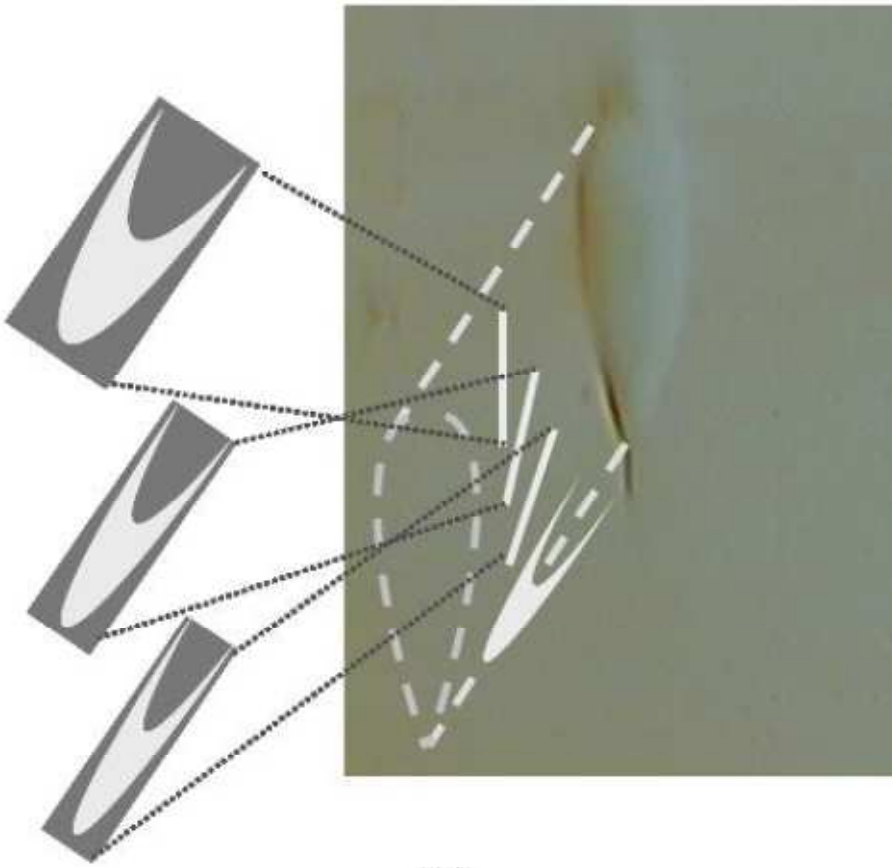

(a)

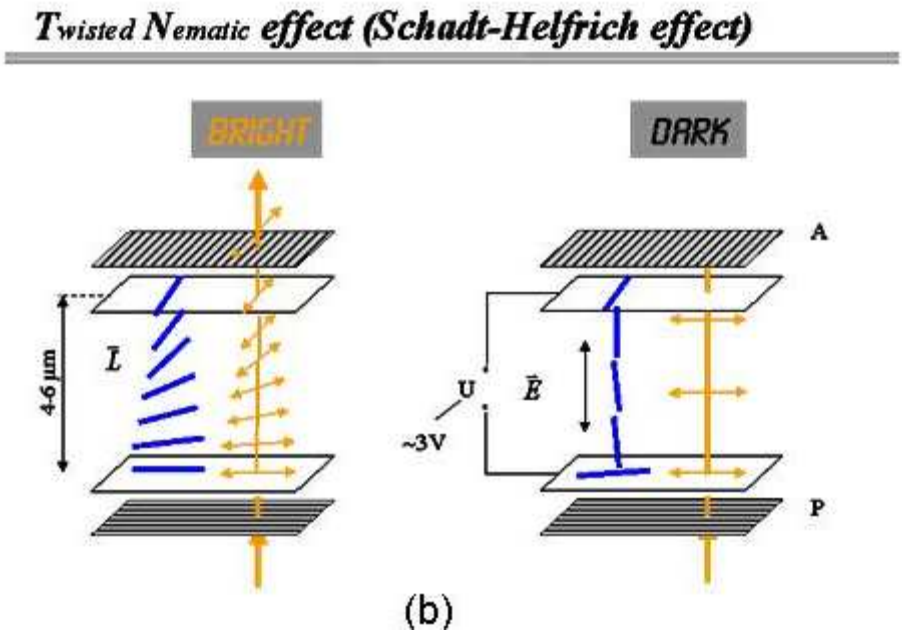

(b)

Figure 7.9: (a): Microscope image of cross-section of the line structure. (b): Twisted nematic effect in liquid crystal [116].

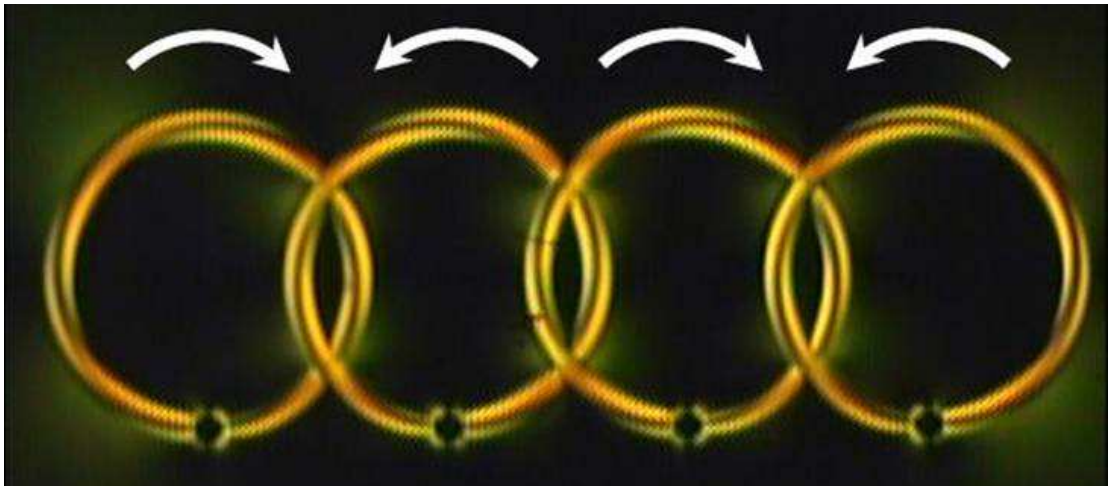

Figure 7.10: Images of written circular structures viewed with crossed polarizers: evidence of chiral patterns.

Finally, a series of circle structures was written by rotating the sample clockwise and anti-clockwise. Imaging in crossed polarizers revealed the presence of chiral patterns (Fig.7.10).

7.6 Conclusions

Birefringence is induced by femtosecond laser direct writing inside chalcogenide glass. Unlike the previously reported photoinduced anisotropy in chalcogenide glass and form birefringence in fused silica, the optical axes of the birefringent region are not determined by the polarization direction of the irradiating light. Instead, the direction of the optical axis is defined by the laser scanning direction and the birefringence is produced by stress which was induced by thermal expansion of the glass during laser irradiation. We also observe the directional dependence of the optical axis orientation on the writing direction. The “U” shape of the optical axis orientation reverses when the birefringent modification was imprinted in the opposite direction. Moreover, the polarization of light, passing through the modified region, rotates in opposite directions on the two sides from the centre of the region, which was produced by the twist of optical axis along the light propagation direction. Furthermore, it is observed that the information on the direction of writing could be recorded and be rewritable inside transparent materials.

Chapter 8

Non-reciprocal ultrafast laser writing

8.1 Introduction

The results presented in the previous chapter highlighted the type-I and type-II femtosecond laser induced modifications in glasses. However glass has intrinsically a low optical nonlinearity and it is not an ideal candidate for the applications of second harmonic generation and electro-optic modulation due to its inversion symmetry. In contrast, lithium niobate ($LiNbO_3$), which is a non-centrosymmetric crystal, is an excellent material for electro-, acousto- and nonlinear-optical applications [117-120]. Femtosecond laser induced modifications in $LiNbO_3$ have attracted increasing interest recently [19, 25, 30, 121-128]. This reason motivated the studies reported in this chapter, which were originally aimed to induce refractive index modification and waveguide structures in lithium niobate by femtosecond laser irradiation. Nevertheless, the observation of the new phenomenon, manifested as a change in material modification by reversing the light propagation direction in a homogeneous medium, led to the first evidence of non-reciprocal ultrafast laser writing, which became the main focus of this chapter.

The dependence of laser induced modification on crystal axes and light propagation direction was described in Sec. 8.2. Section 8.3 discusses the physical mechanism for the non-reciprocal ultrafast laser writing. The main results are summarized in Sec. 8.4.

8.2 Experimental results

8.2.1 Structures written in different directions

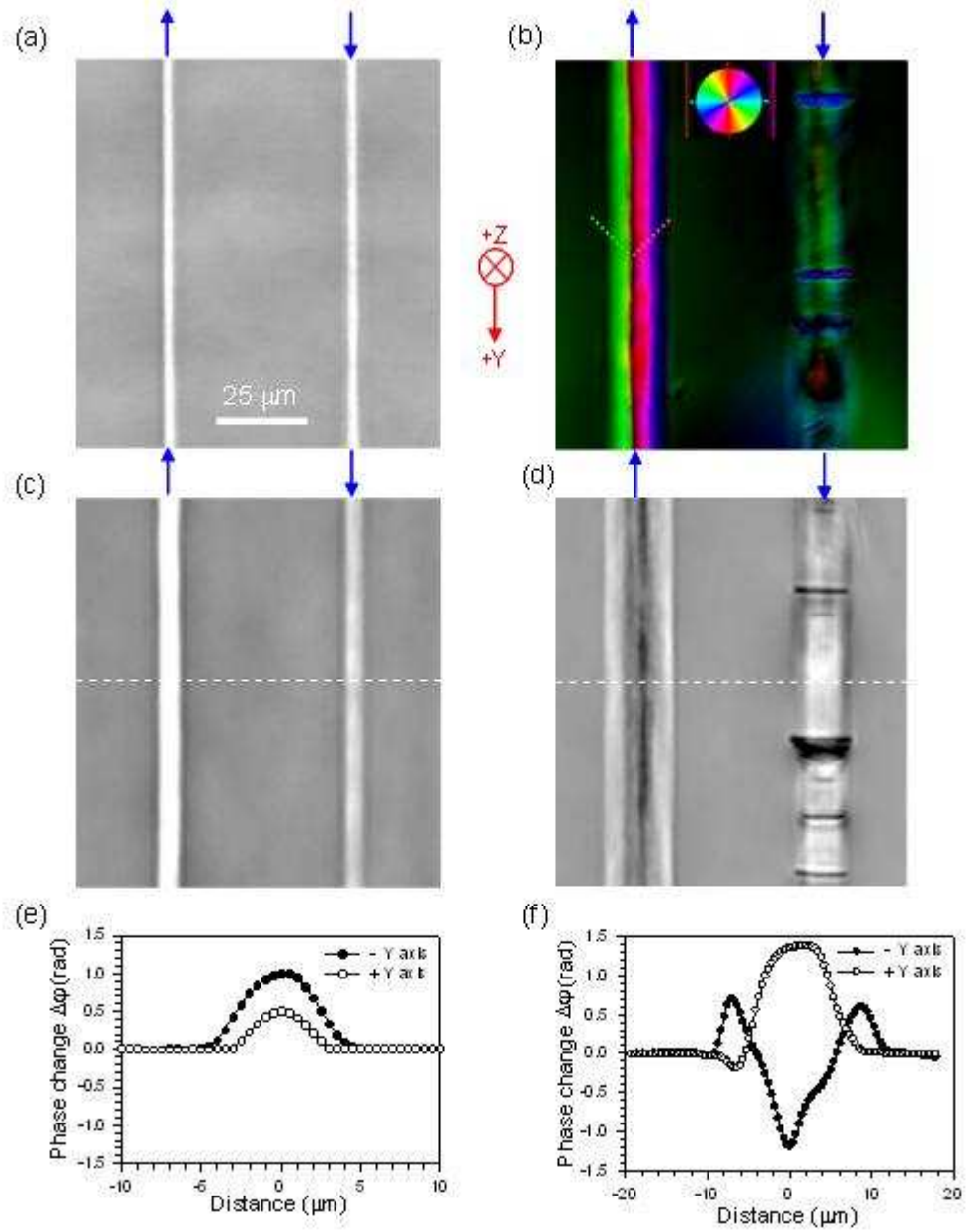

Figure 8.1: Line structures written along the Y-axis of the $LiNbO_3$ sample. (a-c): QPM phase images of the lines written along the -Y axis and the + Y axis of $LiNbO_3$ with pulse energies of: 1.2 µJ (a); 1.8 µJ (b); 2.4 µJ (c). d: Quantitative birefringence image of the line structures. The brightness represents the retardance magnitude while the colour represents the slow axis of the birefringence region. The colour of the circular legend shows the direction of slow axis. The dashed lines show the slow axis of the birefringence region. e: Quantitative phase change profile of the line structure along the dashed line in b. f: Quantitative phase change profile of the line structure along the dashed line in c. Writing directions of the structures in a-d are shown by arrows.

Firstly, groups of lines with various pulse energies ranging from 1 μJ to 2.4 μJ were written below the -Z face of the $LiNbO_3$ sample, using the experiment setup described in Section 3.1, with the scan speed of 200 μm/s. The linearly polarized laser beam (along Y-axis) was focused via a 50X objective (NA = 0.55) 150 μm below the surface of a 1 mm thick sample. For each group, two lines were produced with alternating directions, thus with the writing direction along the -Y and +Y axis of $LiNbO_3$ respectively (Fig. 8.1). Different material modifications, depending on the pulse energy and the writing direction, were observed. For the lines written in both directions with pulses energies below 1.4 μJ, a positive phase change and thus a positive index change is created in the exposed region (Fig. 8.1(a)). The lines have a width of 3 μm, which is close to the focal spot size of the laser beam (Fig. 8.1(a)). No difference was observed for the lines written in the opposite direction. The lines imprinted with pulses energies between 1.4 μJ to 2 μJ still have a positive index change in both directions (Fig. 8.1(c)). However, a directional dependence in the structures written along the –Y and the +Y axis of $LiNbO_3$ appeared. The difference is firstly revealed in the morphology of the line structures. The lines inscribed along the –Y axis of $LiNbO_3$ have a larger width than those along the +Y axis (Fig. 8.1(c)). In addition, the directional difference can also be revealed from the phase change in the structures. The lines written along the –Y axes of $LiNbO_3$ produce a larger positive phase change than those along the +Y axis (Fig. 8.1(e)). With a further increase of pulse energy above 2 μJ, this dependence could even be distinguished from the textures of the lines written in opposite directions. Some optical damage regions appeared in the lines written along the +Y axis of $LiNbO_3$ (Fig. 8.1(c)). In contrast, no damage could be observed in the whole line written along the –Y axis. The phase change ($\Delta\phi$) profile of the lines measured using QPM technique is shown in Fig. 8.1(f). As a result, the line inscribed along the +Y axis still has a positive phase change, similar to those created with lower pulse energies, and exhibits a maximum $\Delta\phi$ of 1.4 rad. By assuming the length of the structure along the Z axis of about 30 μm, the maximum refractive index modification, Δn, is 4×10^{-3}. However, the line written along the – Y axis exhibits a more complex phase change profile. A central dip region shows a negative phase change, while the surrounding regions have a positive phase change. This observation indicates that femtosecond laser modification

results in a negative refractive index change of the central exposed region and a positive index change of the surrounding region. Stressed regions, created as a result of the expansion of the material at the focus of the writing laser beam, can account for the positive index change of the surrounding region [25, 126]. This was confirmed by the quantitative birefringence imaging of the line structures (Fig. 8.1(b)). The line created along the –Y axis of the sample shows two birefringent regions surrounding the central irradiated region and the slow axis of the birefringent region is inclined about 45^0 toward the writing direction (Fig. 8.1(b)). The amorphization of the focal volume and subsequent stress induced birefringence could account for this type of modification. In contrast, no birefringence features could be observed in the structures written along the +Y axis. It is also noted that the birefringence became weaker when the pulse energy decreased and no birefringence could be observed when the pulse energy was below 2 μJ.

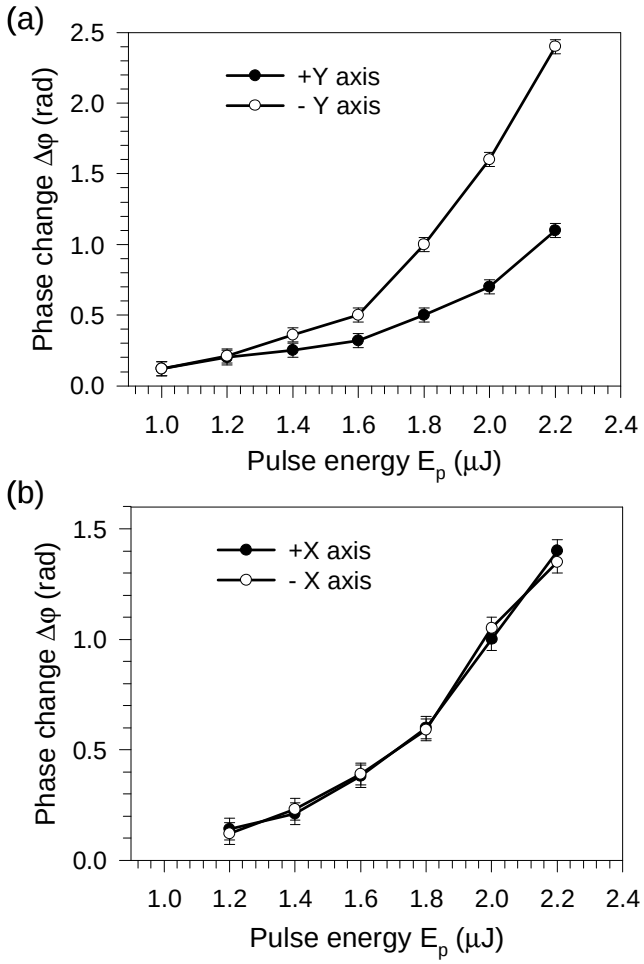

Figure 8.2: Comparison of the line structures imprinted along the Y-axis and along the X-axis. a-b: Measured phase change of the line structures versus pulse energies for the lines written along the Y-axis of the $LiNbO_3$ sample (a) and the X-axis of the $LiNbO_3$ sample (b).

Moreover, the directional dependence does not depend on the laser polarization. Compared to the structures imprinted when the crystal was translated along the Y-axis, no directional dependence has been observed when the structures were written by translating the crystal along the X-axis (Fig. 8.2). This indicates that the directional dependence of the light-induced modifications in $LiNbO_3$ is associated with the crystal symmetry.

8.2.2 Dependence of writing on crystal axis orientation

To verify that the directional dependence of the modifications along the Y axis of $LiNbO_3$ is defined by the crystal axes, four groups of lines were fabricated in the sample. Two groups of the lines with alternating writing directions, along the -Y and +Y axis respectively, were written inside the sample with the pulse energies of 2.4 μJ and 2 μJ. (Fig. 8.3(a)). The sample was then rotated by 180° around the Z axis and another two groups of structures, with the same writing parameters including the direction of the stage movement, was then imprinted in the sample (Fig. 8.3(b)). By comparing Figure 8.3(a) and 8.3(b) it can be observe that the modification of the crystal structure is determined by the orientation of the writing direction with respect to the Y axis of the crystal.

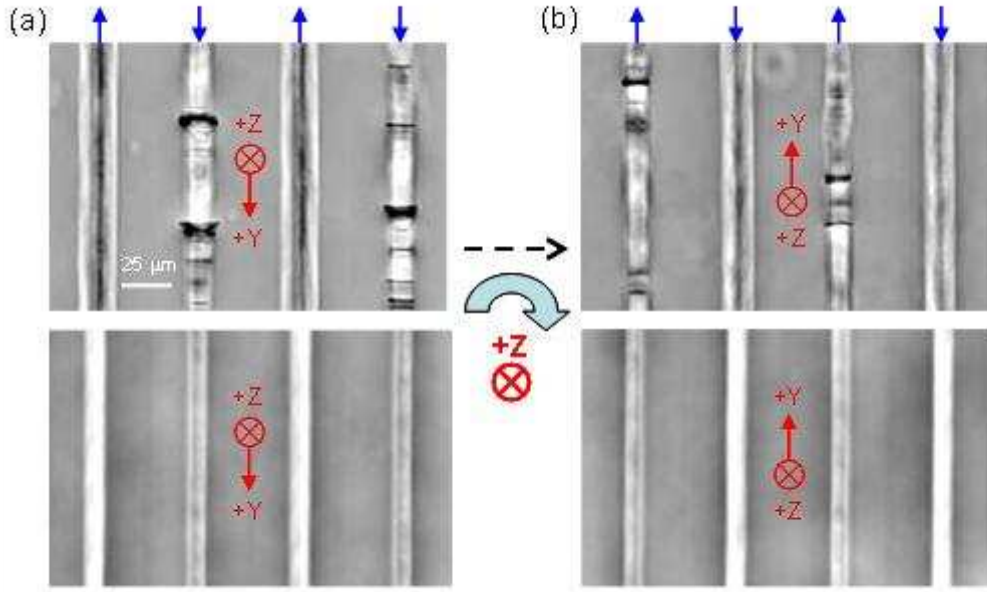

Figure 8.3: Phase images of line structures in the rotation experiment. a-b: QPM phase images of lines imprinted along the Y axis with 2.4 μJ (top) and 2 μJ (bottom) pulse energies. The lines were written before (a) and after rotating by 180° around the Z-axis (b) of the crystal respectively.

8.2.3 Writing with reversed laser beam

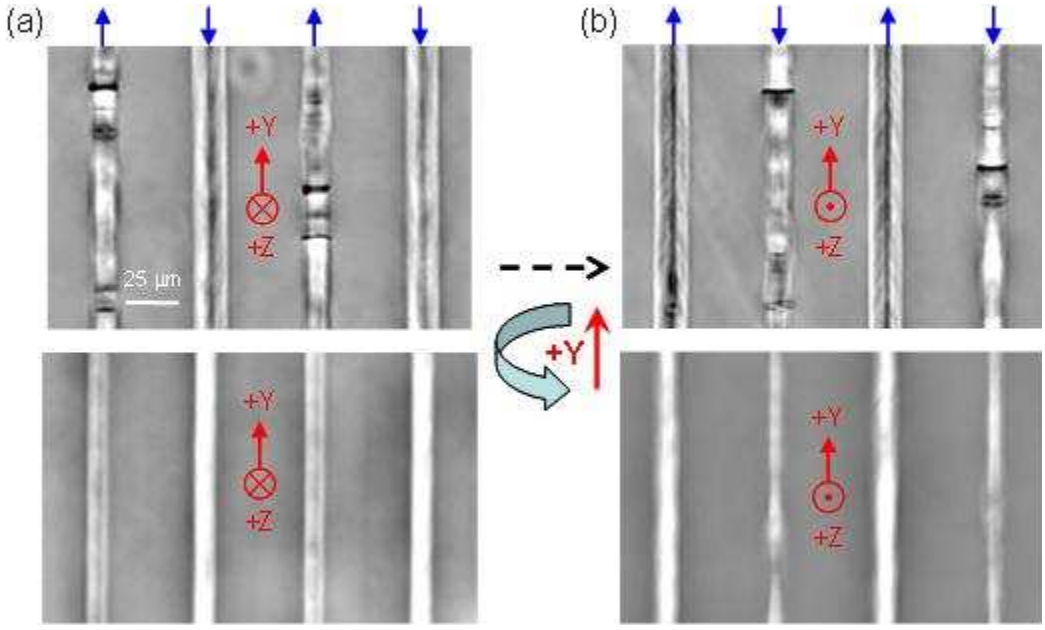

Figure 8.4: Phase images of line structures in the flip experiment. a-b: QPM phase images of lines written along the Y axis with 2.4 µJ (top) and 2 µJ (bottom) pulse energies. The lines were written by propagating the laser beam along the +Z axes (a) and the –Z axes (b) of the crystal respectively.

Secondly, groups of structures were written by the laser beam propagating along the +Z (Fig. 8.4(a)) and the –Z (Fig. 8.4(b)) axes of the crystal. As expected, the created structures were different for writing directions along the +Y and –Y axes of the sample. However, it was surprised to observe a mirror change in the structural modifications in this case, when the propagation direction of the writing beam was reversed. Indeed, in contrast to the lines, written along the +Y axis with 2.4 µJ pulse energy by the beam propagating along +Z axis, which showed the optical damage features (Fig. 8.4(a)), no damage could be observed in the lines imprinted with the same fabrication parameters by the beam propagating along –Z axis (Fig. 8.4(b)). The change in the structural modifications between these lines is only produced by reversing the propagation direction of the focused laser beam with respect to the Z axis of the crystal. Moreover, the modification features, which appeared previously in the line written along the +Y axis by focusing below the –Z face of the crystal, could

only be observed in the line written along the –Y axis when focusing below the +Z face. Therefore a mirror change of the modifications, in two similar structures written along the Y axis (+Y and –Y directions) with the reversed beam propagating direction along the Z axis, is discovered. A similar mirror change of the phase profiles was also observed for the line structures without strong damage features, written with the pulse energy of 2 μJ.

Another intriguing result is the observation of a wavy crack revealed by imaging the deeper region, located slightly beneath the modifications induced in the focal region of the laser beam (Fig. 8.5). The wavy crack appears when the pulse energy is above 2 μJ and its amplitude and period depend on the writing direction. However, the wavy crack could only be observed when the laser beam was focused under the +Z face of the $LiNbO_3$. It should be noted that the wavy crack could in fact be a helical crack (Fig. 8.5(c)). Similar wavy cracks have been observed in quenched glass plates and rubbers subjected to a biaxial stress as a result of Hopf bifurcation transitions [129, 130].

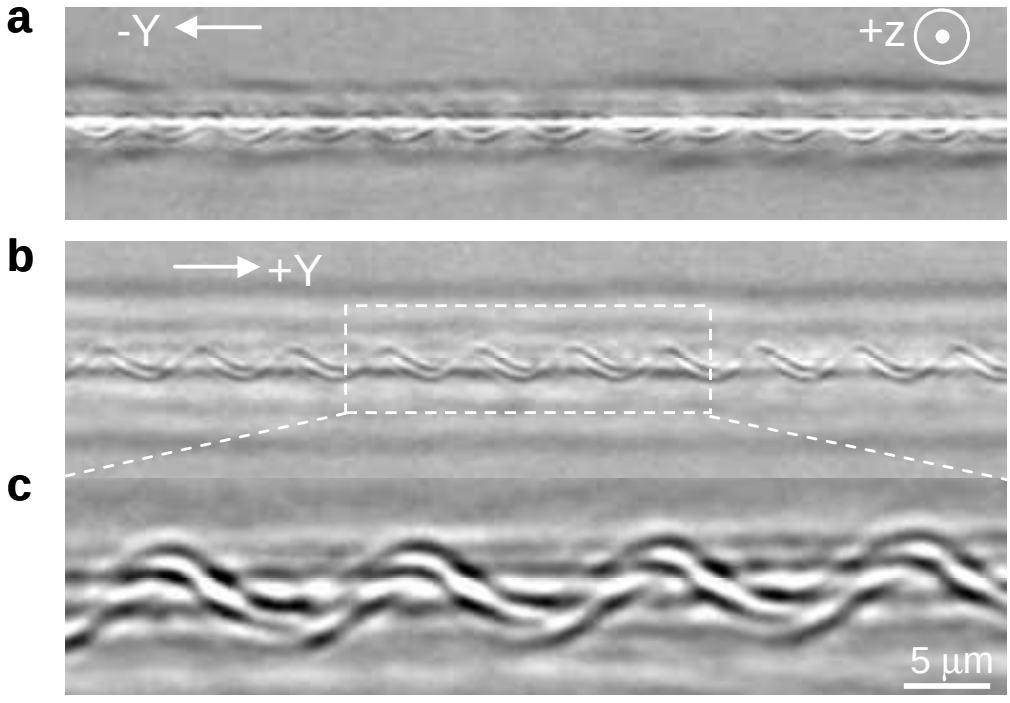

Figure 8.5: QPM phase images of wavy crack by (a) 20X objective, (b) 100X objective.

It is observed that the line width increases with reducing scan speed (Fig. 8.6). This indicates that a heat accumulation effect takes place during the writing process.

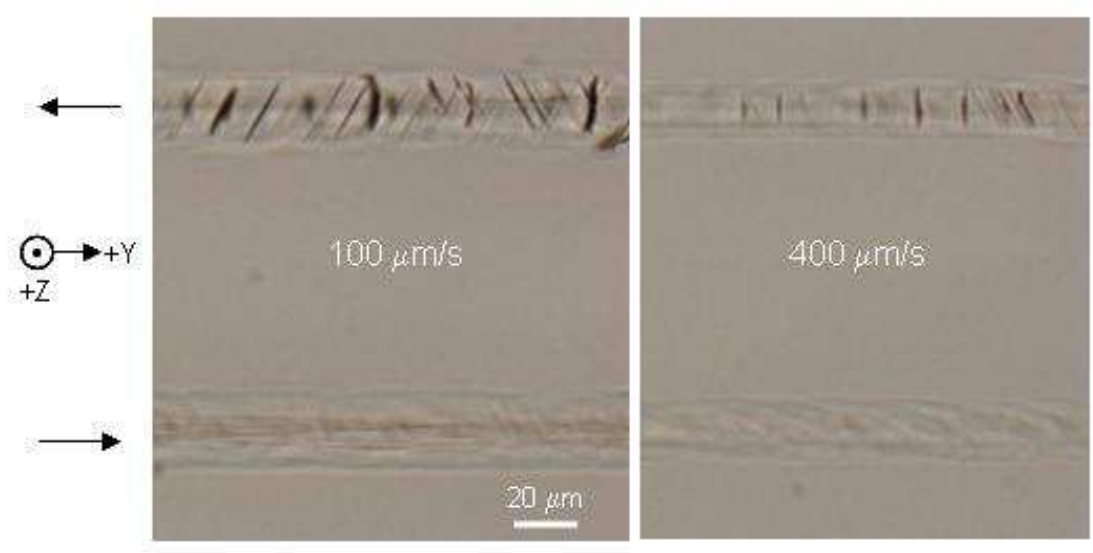

Figure 8.6: Microscopic images of line structures written with scan speeds of 100 μm/s and 400 μm/s.

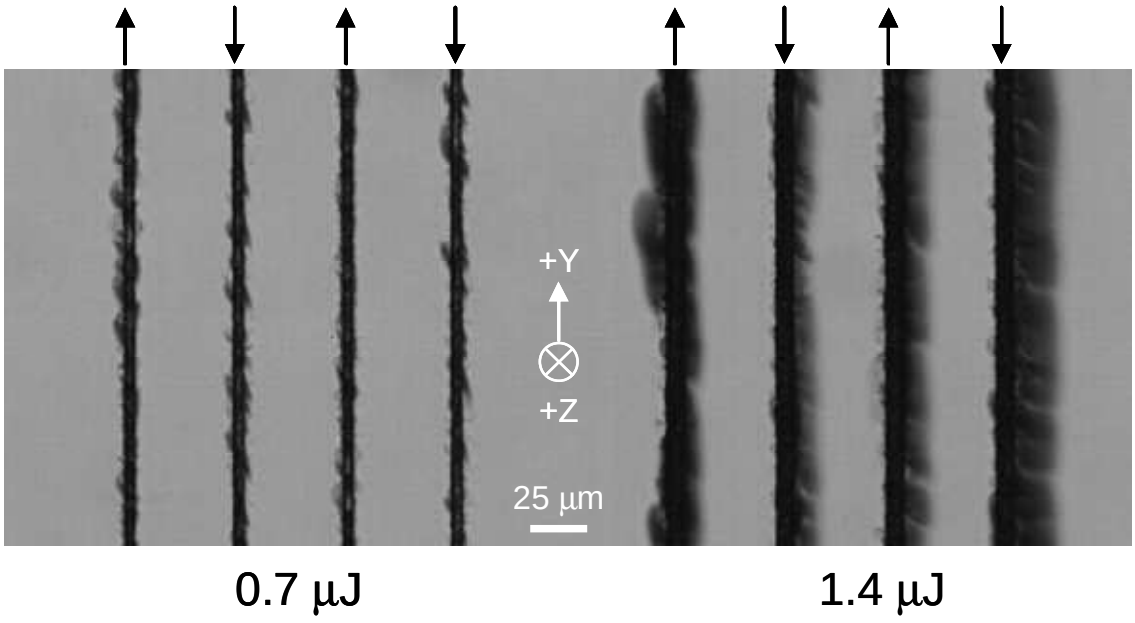

Figure 8.7: Microscopic images of line structures written with the picosecond laser pulses.

8.2.4 Picosecond laser experiment

Groups of line structures were also written in a Z-cut $LiNbO_3$ sample using the picosecond laser system (Lumera Super Rapid), operating at 1064 nm with a 9 ps pulse duration, a 250 kHz repetition rate and with pulse energies comparable to those used with the femtosecond laser system. The modifications, with crack features, were observed at fluencies and intensities of about one order of magnitude lower compared to the femtosecond laser system and with no evidence of the non-reciprocal writing phenomenon (Fig. 8.7). This indicates that ultrashort pulses are necessary for the observation of the phenomenon, possibly due to the higher intensities which could be achieved with femtosecond pulses without strong damage of the sample.

8.2.5 Lithium niobate crystal versus silica glass

It should be noted that the asymmetry of writing in opposite directions (fs-laser quill writing effect) has already been discussed in Chapter 6. However, the directional asymmetry of ultrashort-pulse-light-induced modifications in glass does not depend on the orientation of a medium or the direction of light propagation and it can instead be controlled by the tilt of a pulse front. It has been suggested that the ponderomotive force (light pressure) at the front of the pulse is responsible for the phenomenon. The light pressure produced by the tilted front of the pulse can drag electrons of the electron plasma, generated as a result of multiphoton absorption, in the direction of the writing light beam movement, in a kind of “snow-plough” effect [50].

However, in contrast to glass, the directional dependence of writing in lithium niobate depends on the orientation of a crystal with respect to the direction of the beam movement and the light propagation direction. Specifically, the created structures possess a strong anisotropy only when the focused beam is translated along the Y axis, while no anisotropy is observed when the beam is translated along the X axis. The mirror symmetry of the structures, created by the light beam propagating along the + Z and –Z axes of the crystal (see Fig. 8.4), indicates that the phenomenon observed in $LiNbO_3$ is not relevant to the tilt of the pulse front that was responsible for the fs-laser quill writing effect in glass. In a crystalline medium, even the pressure produced by a

non-tilted pulse front can result in dependence of the created structures on both the direction of writing and the propagation direction of the laser beam.

8.3 Mechanism of the phenomenon and discussion

A heat current ***J***, which is carried by the electrons of the plasma created by the femtosecond laser pulse, and generated by the ponderomotive force and the photon drag effect, can be phenomenologically presented in the following form:

$$J_i = \eta_{ijklmn} E_j E_k^* \nabla_n (E_l E_m^*) + i\zeta_{ijklmn} E_j E_k E_l^* E_m^* k_n \qquad (8.1)$$

where subscripts label Cartesian indices, ***E*** is the complex amplitude of the light electric field, i. e. $E_k E_l^*$ is proportional to the light intensity and is responsible for heating via the plasma absorption. The first and second term in the right-hand-side of Equation (8.1) describe the pressure created by the front of the pulse and the photon drag effect [131], respectively, η_{ijklmn} and $\zeta_{ijklmn} = \zeta_{ikjlmn} = \zeta_{ilmjkn}$ are sixth rank tensors, ***k*** is wave vector. When the light beam propagates along the Z axis of the lithium niobate crystal, the current along the X axis is identically zero by symmetry, while that along the Y axis is the symmetry allowed components of tensors η_{ijklmn} and ζ_{ijklmn}. For example, for the Y-polarized light beam, the thermal current along the Y-axis is given by the following equation:

$$J_y = \left(\eta_{yyyyyz} \frac{\partial |E_y|^2}{\partial z} + ik\zeta_{yyyyyz} |E_y|^2 \right) |E_y|^2 \qquad (8.2)$$

We will refer to this phenomenon as the photothermal effect in noncentrosymmetric media or the bulk photothermal effect in order to highlight that the light-induced heat current can be excited even under homogeneous illumination and in a homogeneous noncentrosymmetric medium [132].

However, the developed phenomenological description of the observed effect does not explain why the heat current produced by laser beam can manifest itself in the modification of a moving sample. The major difficulty here is that the timescales of these processes are very different. Specifically, the laser field, which drives the heat current, described by Eq. (8.1), is last for only about 150 fs. The created electrons in the laser-produced plasma thermally equalize with the lattice in a few picoseconds and finally recombine with nearby ions in a few nanoseconds or even faster. However, at the pulse repletion rate of 250 kHz, the time interval between laser pulses is at least one thousand times longer. The question to be answered is: what is there that "remembers" what direction the laser beam is being translated in 4 microseconds later, when the next laser pulse arrives?

The short answer is that the anisotropic energy distribution, created by the short lasting current described by Eq. (8.1), is finally imprinted in the anisotropy of lattice temperature across the irradiated area. This can been seen as more efficient heating of the material when subsequent pulses arrive in a region where the electric-field driven heat current has already pushed thermal energy from another part of the beam due to the crystal anisotropy. To clarify this, we recall that our experiments were performed in the so-called thermal accumulation regime [127]. In this regime, the material temperature is determined by the cumulative effect of many laser pulses. This is because, in our experimental conditions (beam diameter d = 2µm, thermal diffusivity $D=\kappa/\rho c_p \approx 10^{-2}$ cm^2/s, thermal conductivity $\kappa \approx 2$ W/mK, specific heat capacity $c_p \approx$ 714 J/kgK, volume mass density $\rho \approx 4640$ kg/m^3, pulse repetition rate f = 250 kHz, sample velocity v = 200 µm/s), the effective cooling time $\tau_c = d^2/D \approx 4$ µs coincides with $1/f$ and the thermal diffusion length $L_D = (4D/f)^{1/2} \approx 4$ µm is comparable with the beam diameter. The distance travelled by the sample between two consecutive pulses $h = v/f$ = 0.8 nm, i.e. the number of laser pulses overlapping within the beam diameter is $N = d/h$ = 2500. Such a small beam shift between two pulses implies that the beam movement can be considered to be continuous.

The absorption of the laser radiation results in the average heat production within the focus area with the rate

$$\overline{\left(\frac{\partial Q}{\partial t}\right)}_{\text{hom}} = a(\tau_p \times f)I \tag{8.3}$$

where I is the laser intensity, τ_p is the pulse duration, and a is determined by the absorption coefficient, volume of the irradiated area *etc*. This heating homogeneously increases the temperature within the whole focal area. However, in the focal area of $LiNbO_3$, there exists an average heat current along the Y-axis (Eq. 8.1):

$$\overline{J_y} = b(\tau_p \times f)I^2 \tag{8.4}$$

where b is determined by relevant non-zero components of the material tensors introduced in Eq.(8.1). When the light beam is propagated along the Z-axis of the crystal, this flow will push the heat along the Y-axis at the transfer rate

$$\overline{\left(\frac{\partial Q}{\partial t}\right)}_{anisotropic} = A\overline{J_y} \tag{8.5}$$

where A is the cross-section of the irradiated area in the XZ-plane. This heat transfer will produce the temperature difference between opposite sides of the beam:

$$\Delta T = \frac{d}{\kappa A}\overline{\left(\frac{\partial Q}{\partial t}\right)}_{anisotropic} = \frac{d}{\kappa}\overline{J_y} \tag{8.6}$$

The sign of ΔT depends on the parameter b, i.e. on the relevant component of the material tensor responsible for the observed effect. In particular, if the laser beam is Y-polarized and $Im(\zeta_{yyyyyz}) > 0$, then $J_y < 0$. Therefore, if the Y-axis is horizontal with the negative direction on the right, the temperature of the right-hand side of the irradiated area will be higher than that of the left-hand side (Fig. 8.8). In such a case *the direction of the beam movement along the Y-axis does matter*. Specifically, the temperature of the crystal when the beam is translated along the Y-axis in the negative direction will be always higher than that when the beam is translated along the Y-axis in the positive direction.

The mechanism of this direction-dependent writing can be visualized using the simplified model presented in Fig. 8.8. In this model, for the sake of simplicity we

assume that the beam movement is discontinuous, i.e. that the beam movement along Y-axis consists of jumps equal to the beam diameter in length. The conventional absorption described by Eq. (8.3) produces homogeneous heating of the irradiated area at a temperature T_0. If no other heating mechanisms are present, the temperature is the same for any position of the beam and does not depend on which direction the beam is moved. However, if the anisotropic heating mechanism, described by Eq. (8.4), is involved, the temperature at the right side of the beam is higher than that of the left-hand side by $\Delta T = dJ_y/\kappa$. When the beam jumps right (to the negative direction of the Y-axis) to its next placement, the temperature of the *left side* of the beam increases to $T+\Delta T$, while the temperature of the right side of the beam is T. The anisotropic heating mechanism is switched on and increases the temperature of the *right side* so that it will be ΔT higher than that of the left side of the beam. As a result, the temperature of the *right side* of the beam will be equal to $T + 2\Delta T$. The same temperature increase will happened after the next jump. After m jumps in the direction that coincides with the direction of the anisotropic heat flow, the temperature of the very right irradiated area will be equal to

$$T_{parallel}^{\max} = T_0 + \frac{md}{\kappa} \times \overline{J_y} \tag{8.7}$$

When the light beam moves in the positive direction along the Y-axis, the temperature of the left-side of the beam is the same after each jump. Therefore, although the anisotropic heating mechanism results in the increase of the temperature of the right-side of the beam, the temperature of the crystal does not increase (see Fig. 8.8):

$$T_{opposite}^{\max} = T_0 + \frac{d}{\kappa} \times \overline{J_y} \tag{8.8}$$

Therefore, the anisotropic heating may result in a drastically different scenario for the laser writing, which we refer to as *differential heating* of the sample. This increase of the temperature, described by Eq. (8.7), will eventually slow down due to thermal diffusion and melting of the sample. Moreover uneven heating of the sample when the beam moves opposite to the heat flow, which is described by Eq. (8.8) and illustrated in Fig. 8.8, may results in a shock-induced damage, which is evident for one of the writing directions (Fig. 8.3 and 8.4). Apparently in the real experimental

conditions, the situation is more complicated because we need to account for the interplay of the thermal diffusion and the accumulation; however the simplified model above well illustrates how anisotropic heating can manifest itself in crystal modification by a moving laser beam.

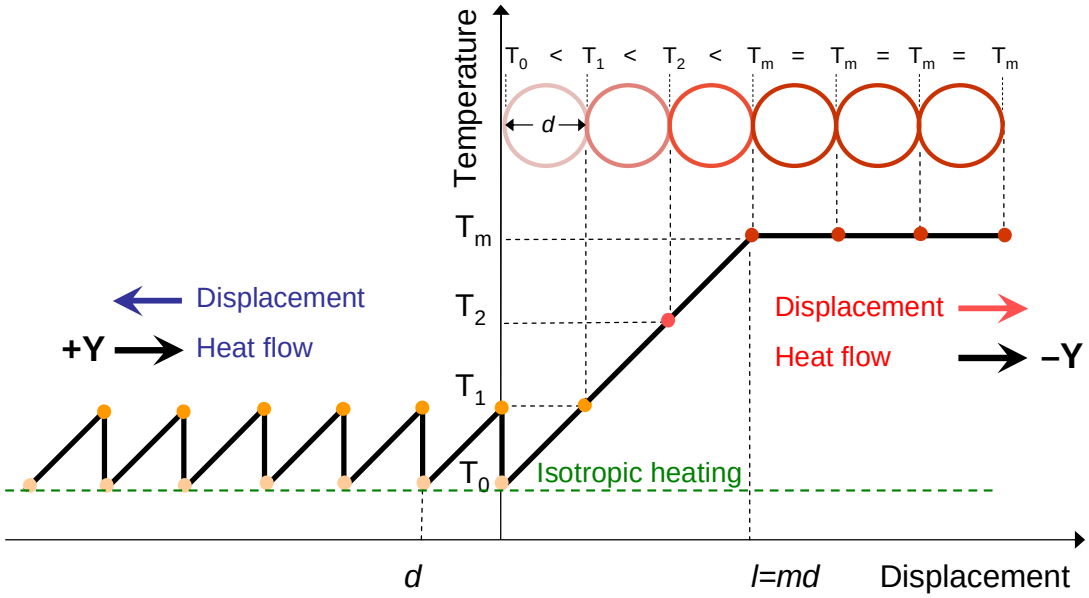

Figure 8.8: Illustration of the differential heating of a crystal as a result of the bulk photothermal effect. Heat flows in the –Y direction of the crystal (black arrow). Temperature of the crystal increases till saturation when the beam is displaced in the direction of heat flow (red arrow) and oscillates near the level defined by isotropic heating (green line) when displacement is opposite to the heat flow (blue arrow). Big circles illustrate the laser beam and darker colour corresponds to higher temperature of the sample in the position of the beam.

The restrictions imposed on the light-induced current by crystalline symmetry explain the observed directional dependence of writing. Specifically, since the light beam propagated along the Z axis does not produce thermal current along the X axis, the crystal modification is not sensitive to the translation of the light beam along the X axis. In contrast, when the beam is translated along the Y axis, the in-plane heat flow is either parallel or anti-parallel to the beam velocity. Since the heating of the crystal is stronger when the direction of the heat flow coincides with the direction of the beam movement, the modification of the non-centrosymmetric crystal shows a pronounced directional dependence independent of the tilt of the pulse front. It should also be noted that similar crystal modifications for the X- and Y-polarized beams. Such an experimental finding is also supported by crystal symmetry because, in the $LiNbO_3$ crystal, the thermal current along the Y-axis is not forbidden for X- and Y-polarized beams, however the current is described by different independent

components of the material tensor. The similarity of the crystal modifications just indicates that these components are of the same order of magnitude.

It can be observed from Eqs. (8.1, 8.2) that interplay of the crystal anisotropy and light-induced heat flow gives rise to a new non-reciprocal, nonlinear optical phenomenon - the nonreciprocal photosensitivity. In the $LiNbO_3$, the nonreciprocal photosensitivity manifests itself as changing the sign of the light-induced current when light propagation direction is reversed. This phenomenon is visualized when the modification of the crystal is performed by a moving light beam; in such a case the created pattern is mirrored when the light propagation direction is reversed.

8.4 Conclusions

In conclusion, non-reciprocal ultrafast laser writing in Z-cut lithium niobate crystal was first realized by a tightly focused ultrafast laser beam. It was discovered that when the direction of the laser beam is *reversed* from +Z to – Z directions, the structures written in the crystal when translating the beam along the +Y and –Y directions are *mirrored.* Therefore, a single light beam interacts with the crystal differently for opposite directions of light propagation. This new non-reciprocal nonlinear optical phenomenon is interpreted in terms of light pressure at the front of the ultrashort pulse, the photon drag effect, and associated light-induced thermal current in crystalline media. It should be noted that nonreciprocal phenomena are very rare in optics and are usually associated with breaking of the time-reversal symmetry due to the presence of the magnetic field. One may recall the conventional Faraday effect and magneto-chiral dichroism [133], when the interaction of a single light beam with a homogeneous material is different for two opposite directions similarly to the non-reciprocal photosensitivity reported here.

Chapter 9

Conclusions and future work

9.1 Summary and discussion

In summary, a structural modification with positive index change (type-I) has been demonstrated in high index bismuth borate glass by femtosecond laser direct writing. This type of modification was used to fabricate waveguides in this high index glass. Low loss, polarization insensitive, single mode waveguides with circular mode profiles and refractive index changes up to 4.5×10^{-3} were inscribed by ultrafast laser radiation in this glass. An insertion loss of only 1 dB and a propagation loss of 0.2 dB/cm at 1.55 μm were demonstrated. Y-splitters and directional couplers were also fabricated and their performance closely agreed with theoretical simulations based upon experimentally measurable quantities obtained from the waveguide characterization. Moreover, a 500 nm spectral broadening was obtained by launching less than 2.0 mW average power (53 kW peak-power) of 150 fs laser pulses at 1.46 μm through the waveguides. The supercontinuum is mainly caused by self-phase modulation allowing the estimation of a nonlinear refractive index, n_2, of ~ 6.6×10^{-15} cm^2/W, which is in agreement with published data [19]. Preliminary experiments on the uniformly poled waveguides show the same $\chi^{(2)}$ value as the bulk glass. Femtosecond laser written low loss waveguides with large n_2 are attractive for fabricating nonlinear glass based devices.

Type-II modification was induced inside the fused silica by femtosecond laser irradiation. Self-assembled, sub-wavelength periodic structures created in the focal volume were shown to account for this type of modification. Two different types of periodic structures, the main one with period (Λ_E) in the direction of the laser beam polarization and the second with period (Λ_k) in the direction of the light propagation, are identified from the cross-sectional images of the modified regions using scanning

electron microscopy. The range of effective pulse energy which could produce nanogratings narrows when the pulse repetition rate of the writing laser increases. The period, $\Lambda_{E,}$ is proportional to the wavelength of the writing laser and the period, $\Lambda_{k,}$ in the head of the modified region remains approximately the wavelength of light in fused silica.

A new phenomenon in ultrafast laser processing of transparent optical materials, in particular silica glass, manifested as a change in material modification by reversing the writing direction is observed. The effect resembles writing with a quill pen and is interpreted in terms of a new physical effect - anisotropic trapping of an electron plasma by a tilted front of the ultrashort laser pulse. Moreover, a change in structural modification was demonstrated in a silica glass sample by controlling the direction of pulse front tilt, achieving a calligraphic style of laser writing which is similar in appearance to that inked with the bygone quill pen. Furthurmore a new type of modification associated with anisotropic bubble formation, which could be controlled by the writing direction, was observed at high pulse energies. The phenomenon of modification transition in a continuous encryption process was observed. We anticipate that the possibility of achieving control of light-matter interactions, by adjusting the tilt of ultrashort pulse front, will open new opportunities in material processing, optical manipulation and data storage.

Strong birefringence was induced inside chalcogenide glass by femtosecond laser direct writing. Unlike the previously reported photoinduced anisotropy in chalcogenide glass and form birefringence in fused silica, the optical axes of the birefringent region are not determined by the polarization direction of the irradiating light. Instead, by varying the scanning direction of the laser irradiation, the optical axes of the birefringence can be changed. As a result, the information on the direction of writing could be recorded inside transparent materials. Moreover, this type of photoinduced anisotropy can be erased by annealing, and is reversible by repeatable scanning.

Photosensitivity is a material property that is relevant to many phenomena and applications, from photosynthesis and photography to optical data storage and ultrafast laser writing. It was commonly thought that, in a homogeneous medium,

photosensitivity and the corresponding light-induced material modification do not change on reversing the direction of light propagation. In this thesis it was demonstrated for the first time that when the direction of the femtosecond laser beam is reversed from +Z to – Z directions, the structures written in lithium niobate crystal when translating the beam along the +Y and –Y directions are mirrored. In a non-centrosymmetric medium modification of the material can therefore differ when light propagating in opposite directions. This is the first evidence of a new optical phenomenon of non-reciprocal photosensitivity.

9.2 Future work

As summarized above, this thesis has advanced the field of femtosecond laser direct writing in several respects, but several unanswered questions and open challenges remain.

With regards to physics, a complete model of the interaction of femtosecond laser pulses with transparent materials needs to be established, including the simulation of the focused ultrashort pulses in the focal region, with a particular emphasis on determining the effect of both the spatial and the temporal distortion on the laser intensity distribution, and subsequent laser induced plasma distribution. This data will provide a more realistic comparison with the experiment results.

With regards to application, femtosecond laser induced high density optical data storage in fused silica is one of the promising areas. Compared to traditional three dimensional data storage in optical materials, where the density is limited by the focal spot size, here another “dimension” could be available using the orientation of the self-assembled nanostructure (type-II) formed in the focal area, which is determined by the polarization direction of the writing laser. This work is presently underway in the collaboration set up between our group and the Hirao group in Kyoto (Fig. 9.1). Moreover, photonic devices based on the femtosecond laser inscribed waveguide structures (Type I) are also very attractive. Low loss waveguides with large optical

nonlinearities are attractive for fabricating frequency convertors and supercontinuum generators.

Figure 9.1: Type-II modification induced in fused silica by femtosecond laser direct writing. The different colour of each letter is corresponding to the different orientation of the slow axis of the birefringence.

Overall, the femtosecond laser direct writing technique is slowly becoming commercialized; however it is often limited by the low processing speed and high cost of the laser system. More affordable and easier to operate, commercially available, femtosecond fibre laser systems operating at MHz repetition rates, with uJ pulse energy, are very attractive. With the ability to realize three-dimensional multi-component devices, femtosecond laser micromachining shows tremendous potential in the laser material processing field.

Appendix A

Slit beam shaping method

In this appendix, the slit beam shaping method used for optimizing the waveguide cross-section is discussed.

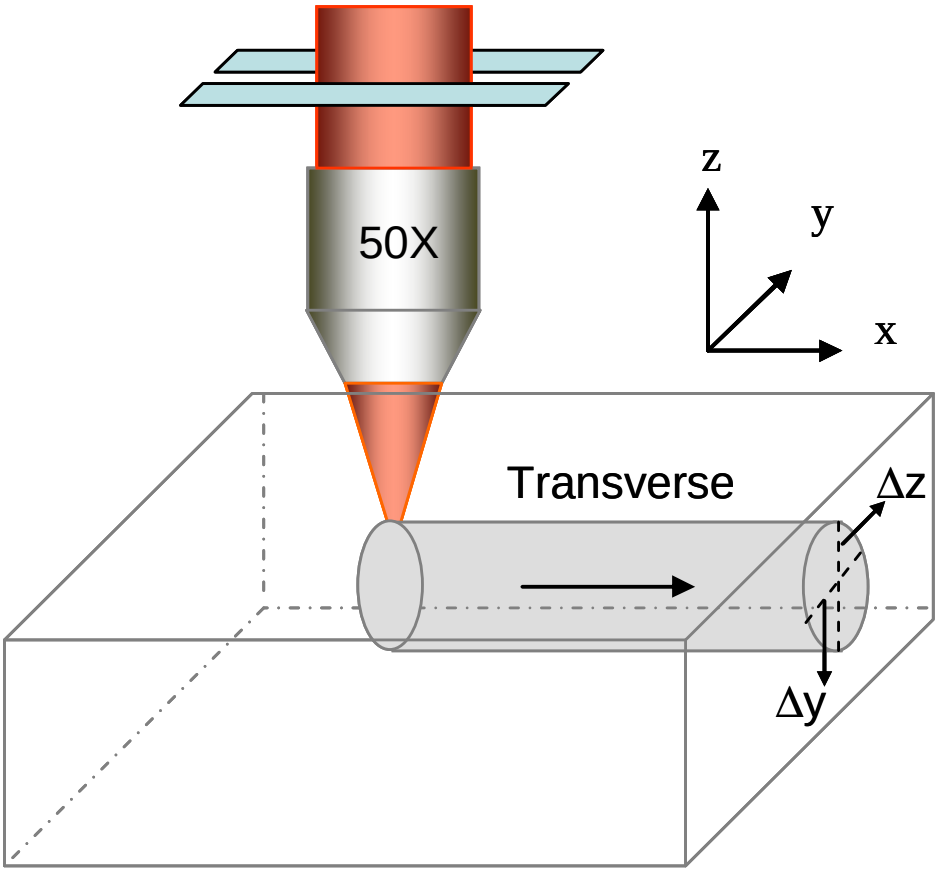

Figure A.1: Schematic drawing of the slit beam shaping method.

For a circular Gaussian beam with a beam waist in the input plane of the lens, the energy distribution near the focal point can be expressed as:

$$I = \frac{1}{[1+(z^2/z_0^2)]}\exp\left[\frac{-2(x^2+y^2)}{\omega_0^2(1+z^2/z_0^2)}\right] \qquad \text{(A.1)}$$

where ω_0 is the beam waist at the focal point, $z_0 = k\omega_0^2/2$ is the corresponding Rayleigh length and *k* is the wave vector.

As shown in Figure A.1, for an elliptical Gaussian beam exiting from the slit, with its major axis in the *x* direction and its minor axis in the *y* direction, the new intensity distribution near the focal point can be expressed as:

$$I = \frac{1}{\left[1+(z^2/z_{0x}^2)\right]^{\frac{1}{2}}}\frac{1}{\left[1+(z^2/z_{0y}^2)\right]^{\frac{1}{2}}}\exp\left[\frac{-2x^2}{\omega_{0x}^2(1+z^2/z_{0x}^2)}\right]\exp\left[\frac{-2y^2}{\omega_{0y}^2(1+z^2/z_{0y}^2)}\right] \quad \text{(A.2)}$$

where ω_{0x}, ω_{0y} is the beam waist at the focal point along the x and y direction; z_{0x}, z_{0y} is the corresponding Rayleigh length respectively. We assume that the effective full width of the elliptical beam along the x direction is the same size as the input aperture of the objective lens. As a result, ω_{0x} and z_{0x} are the same value as the ω_0 and z_0 in Equation (A.1). However, ω_{0y} is now equal to $(R_x/R_y)\omega_{0x}$, where R_x (R_y) is the radius along the major (minor) axis of the elliptical beam; and z_{0y} is equal to $k\omega_{0y}^2/2$. Thus, the intensity distribution in the *yz* plane (x = 0) near the focal spot can be expressed as:

$$I(y,z) = \frac{1}{\left[1+(z^2/z_{0x}^2)\right]^{\frac{1}{2}}}\frac{1}{\left[1+(z^2/z_{0y}^2)\right]^{\frac{1}{2}}}\exp\left[\frac{-2y^2}{\omega_{0y}^2(1+z^2/z_{0y}^2)}\right] \quad \text{(A.3)}$$

The intensity distribution in the *yz* plane with various R_x/R_y values is shown in Fig A.2. It is clear that the intensity distribution in the focal point can be more symmetrical if the R_x/R_y ratio is increased. This can be used to improve the aspect ratio of the waveguide cross-section.

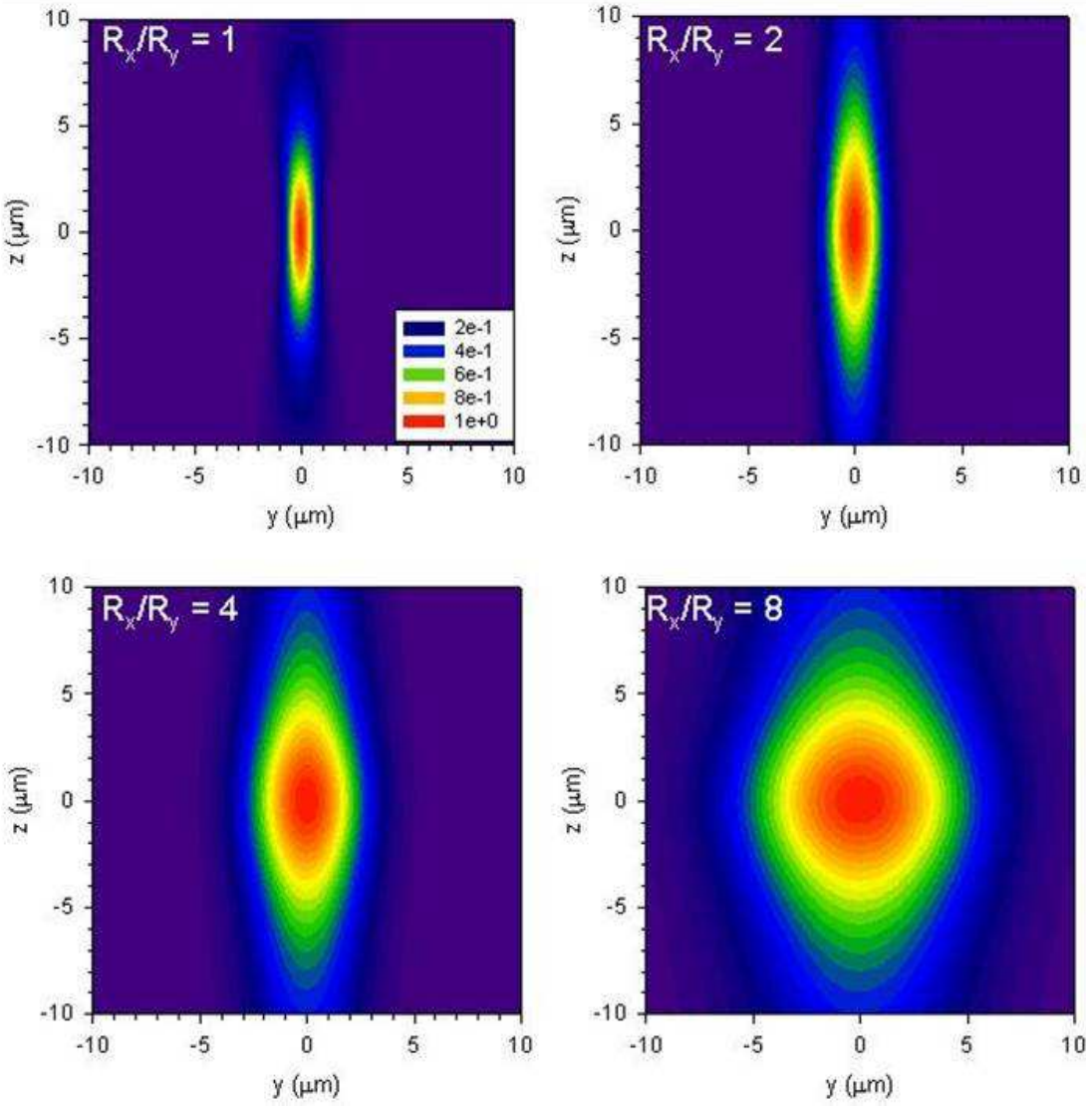

Figure A.2: Computer simulations of intensity distributions near the laser focal spot with various R_x/R_y ratios.

List of publications

Journal papers

Weijia Yang, Erica Bricchi, Peter G. Kazansky, James Bovatsek and Alan Y. Arai, "Self-assembled periodic sub-wavelength structures by femtosecond laser direct writing." Opt. Express **14**, 10117 (2006).

Mark Hughes, Weijia Yang and Dan Hewak, "Fabrication and characterisation of femtosecond laser written waveguides in chalcogenide glass." Appl. Phys. Lett. **30**, 131113 (2007).

Peter G. Kazansky, Weijia Yang, Erica Bricchi, James Bovatsek, Alan Y. Arai, Yasuhiko Shimotsuma, Kiyotaka Miura and Kazuyuki Hirao, "Quill writing with ultrashort light pulses in transparent optical materials." Appl. Phys. Lett.. **90**, 151120 (2007).
Accepted in Virtual Journal of Ultrafast Science Volume 6, Issue 5, May 2007
Highlighted in Photonics Spectra, Technology World, June 2007.
http://www.photonics.com/content/spectra/2007/June/tech/87793.aspx

Weijia Yang, Peter G. Kazansky and Yuri P. Svirko "Non-reciprocal ultrafast laser writing." Nature Photonics **2**, 99-104 (2008).
Highlighted in Laser Focus World 40, April 2008
http://www.laserfocusworld.com/display_article/325432/12/none/none/News/MATERIALS-SCIENCE:-Ultrafast-laser-reveals-nonreciprocal-photosensitivit
Highlighted in Optics.org
http://optics.org/cws/article/research/32639

Weijia Yang, Costantino Corbari, Peter G. Kazansky Koichi Sakaguchi and Isabel C.S. Carvalho, "Fabrication of photonic components in bismuth borate glass by femtosecond laser direct writing." Opt. Express **19**, 16215 (2008).

Weijia Yang, Peter G. Kazansky, Yasuhiko Shimotsuma and Kazuyuki Hirao, "Ultrashort-pulse laser calligraphy." Appl. Phys. Lett. **93**, 171109 (2008).

M. Lancry, N. Groothoff, S. Guizard, W. Yang, B. Poumellec, P.G. Kazansky and J. Canning, "Influence of pure silica OH content on femtosecond laser processing." submitted to J. Non-Cryst. Solids, 2008.

Weijia Yang, Peter G. Kazansky, Ryota Kitagawa and Hiromichi Takebe, "Stress birefringence induced in glass by femtosecond laser irradiation." To be submitted to Opt. Express, 2008.

Conference papers and invited talks:

M. Lancry, N. Groothoff, S. Guizard, W. Yang, B. Poumellec, P.G. Kazansky and J. Canning, “Influence of pure silica OH content on femtosecond laser processing.” The 7th symposium on "SiO_2 advanced dielectrics and related devices", June 30 – July 02, 2008, Saint-Etienne, France

Peter G. Kazansky, Weijia Yang, Yuri Svirko, Yasuhiko Shimotsuma and Kazuyuki Hirao, “Ultrashort-Pulse Laser Calligraphy.” THUIIIa.1, Conference on Ultrafast Phenomena 2008, Stresa, Italy.

Weijia Yang, Peter G. Kazansky, Yasuhiko Shimotsuma and Kazuyuki Hirao, “Ultrashort-pulse laser calligraphy.” CMF4, CLEO 2008, San Jose USA.

Peter G. Kazansky, Weijia Yang and Yuri P. Svirko, “Non-reciprocal ultrafast laser writing.” CMF2, CLEO 2008, San Jose USA.

Peter G. Kazansky, Weijia Yang, Erica Bricchi,, James Bovatsek, Alan Y. Arai, Yasuhiko Shimotsuma, Kiyotaka Miura and Kazuyuki Hirao, “Quill writing with ultrashort light pulses in transparent optical materials.” CThJ2, CLEO 2007, Baltimore.

Weijia Yang, Costantino Corbari, Peter G. Kazansky and Koichi Sakaguchi, “Fabrication of photonic devices in heavy metal oxide glass by femtosecond laser direct writing.” CF8-4-THU, CLEO/Europe-IQEC 2007, Munich Germany.

Peter G. Kazansky, Weijia Yang, Erica Bricchi, James Bovatsek and Alan Y. Arai, "Femtosecond laser nanostructuring of transparent materials: from bulk to fiber lasers" Novosibirsk, Russian Fiber Lasers 4-6 Apr 2007 2007 (**Invited**).

Peter G. Kazansky, Olivier Deparis, Isabel Carvalho, Erica Bricchi, Weijia Yang, Amin Abdolvand, Alexander Podlipensky, Gerhard Seifert Heinrich Graener, Yasuhiko Shimotsuma, Jiarong Qiu, Kazuyuki Hirao, James Bovatsek and Alan Arai. “Recent advances in nanostructuring of glass: from poling to femtosecond laser writing.” BGPP/NP 2007 Quebec Canada 2-6 Sep 2007 (**Invited**).

Peter G. Kazansky, Olivier Deparis, Isabel Carvalho, Erica Bricchi, Weijia Yang, Amin Abdolvand, Alexander Podlipensky, Gerhard Seifert Heinrich Graener, Yasuhiko Shimotsuma, Jiarong Qiu, Kazuyuki Hirao, James Bovatsek and Alan Arai. “Recent advances in poling and nanostructuring of glass.” 7th Pacific Rim Conference on Ceramic and Glass Technology Shanghai China 11-14 Nov 2007 (**Invited**).

Peter G. Kazansky, Olivier Deparis, Isabel Carvalho, Erica Bricchi, Weijia Yang, Amin Abdolvand, Alexander Podlipensky, Gerhard Seifert Heinrich Graener, Yasuhiko Shimotsuma, Jiarong Qiu, Kazuoki Hirao, James Bovatsek and Alan Arai. “Recent advances in nanostructuring of glass by strong fields: from poling assited bleaching to femtosecond laser nanostructuring.” Invited Talk: IV International

Symposium on Non-Crystalline Solids, VIII Brazilian Symposium on Glass and Related Materials, Brazil 21-28 Oct 2007 (**Invited**).

Peter G. Kazansky, Weijia Yang, Erica Bricchi, Ryota Kitagawa and Hiromichi Takebe, "Breaking symmetry in glass by femtosecond laser irradiation." CMX5, CLEO 2006, Long Beach, USA.

Erica Bricchi, Weijia Yang, Peter Horak, Costantino Corbari and Peter G. Kazansky, "Characterization of Nanoscale Structures Observed in Femtosecond Laser Micromachining." CMHH6, CLEO 2006, Long Beach, USA.

Peter G. Kazansky, Weijia Yang, Erica Bricchi, Yasuhiko Shimotsuma, Kazuyuki Hirao, Ryota Kitagawa and Hiromichi Takebe. "Unusual modifications of glass by femtosecond laser irradiation." 8th ESG Conference with the Annual Meetings of the ICG and SGT 2006 Sunderland, UK, 10-14 September 2006 (**Invited**).

Peter G. Kazansky, Weijia Yang, Erica Bricchi, Yasuhiko Shimotsuma, Kazuyuki Hirao, Ryota Kitagawa and Hiromichi Takebe. "Creating unusual structures by ultrashort light pulses in glass." 1st International Workshop on Multiphoton Process in Glass and Glassy Materials. Sydney Australia 11-12 Dec 2006 (**Invited**).

Erica Bricchi, Weijia Yang and Peter G. Kazansky, "Robustness of femtosecond direct written structures in silica glass" CThV4, CLEO 2005, Baltimore, USA.

Weijia Yang, Erica Bricchi and Peter G. Kazansky, "Symmetric waveguides written in Er^{3+}-doped Bi_2O_3-based using femtosecond laser pulses" CThV6, CLEO 2005, Baltimore, USA.

Weijia Yang, Erica Bricchi and Peter G. Kazansky, "Waveguide fabrication in bismuthate glasses using femtosecond laser pulses" POWAG 2004, Bath, U.K.

Bibliography

1. T. H. Maiman, "Stimulated optical radiation in ruby," Nature **187**, 493-494 (1960).

2. R. L. Fork, B. I. Greene, and C. V. Shank, "Generation of Optical Pulses Shorter Than 0.1 Psec by Colliding Pulse Mode-Locking," Appl. Phys. Lett. **38**, 671-672 (1981).

3. A. H. Zewail, "Laser Femtochemistry," Science **242**, 1645-1653 (1988).

4. L. Huang, J. P. Callan, E. N. Glezer, and E. Mazur, "GaAs under Intense Ultrafast Excitation: Response of the Dielectric Function," Phys. Rev. Lett. **80**, 185 (1998).

5. A. Rousse, P. Audebert, J. P. Geindre, F. Falliès, J. C. Gauthier, A. Mysyrowicz, G. Grillon, and A. Antonetti, "Efficient K alpha x-ray source from femtosecond laser-produced plasmas," Phys. Rev. E **50**, 2200 (1994).

6. A. Braun, G. Korn, X. Liu, D. Du, J. Squier, and G. Mourou, "Self-Channeling of High-Peak-Power Femtosecond Laser-Pulses in Air," Opt. Lett. **20**, 73-75 (1995).

7. T. A. Birks, W. J. Wadsworth, and P. S. Russell, "Supercontinuum generation in tapered fibers," Opt. Lett. **25**, 1415-1417 (2000).

8. K. M. Davis, K. Miura, N. Sugimoto, and K. Hirao, "Writing waveguides in glass with a femtosecond laser," Opt. Lett. **21**, 1729-1731 (1996).

9. E. N. Glezer, M. Milosavljevic, L. Huang, R. J. Finlay, T. H. Her, J. P. Callan, and E. Mazur, "Three-dimensional optical storage inside transparent materials," Opt. Lett. **21**, 2023-2025 (1996).

10. R. Birngruber, C. A. Puliafito, A. Gawande, W. Z. Lin, R. W. Schoenlein, and J. G. Fujimoto, "Femtosecond Laser Tissue Interactions - Retinal Injury Studies," IEEE J. Quantum Electron. **23**, 1836-1844 (1987).

11. C. B. Schaffer, A. Brodeur, J. F. Garcia, and E. Mazur, "Micromachining bulk glass by use of femtosecond laser pulses with nanojoule energy," Opt. Lett. **26**, 93-95 (2001).

12. G. Cerullo, R. Osellame, S. Taccheo, M. Marangoni, D. Polli, R. Ramponi, P. Laporta, and S. De Silvestri, "Femtosecond micromachining of symmetric waveguides at 1.5 mu m by astigmatic beam focusing," Opt. Lett. **27**, 1938-1940 (2002).

13. R. Osellame, S. Taccheo, G. Cerullo, M. Marangoni, D. Polli, R. Ramponi, P. Laporta, and S. De Silvestri, "Optical gain in Er-Yb doped waveguides fabricated by femtosecond laser pulses," Electron. Lett. **38**, 964-965 (2002).

14. S. Nolte, M. Will, J. Burghoff, and A. Tuennermann, "Femtosecond waveguide writing: a new avenue to three- dimensional integrated optics," Appl. Phys. A: Mater.Sci. Process. **77**, 109-111 (2003).

15. A. Saliminia, N. T. Nguyen, M. C. Nadeau, S. Petit, S. L. Chin, and R. Vallee, "Writing optical waveguides in fused silica using 1 kHz femtosecond infrared pulses," J. Appl. Phys. **93**, 3724-3728 (2003).

16. R. Osellame, "Femtosecond writing of active optical waveguides with astigmatically shaped beams," J. Opt. Soc. Am. B **20**, 1559-1567 (2003).

17. R. Osellame, N. Chiodo, G. Della Valle, S. Taccheo, R. Ramponi, G. Cerullo, A. Killi, U. Morgner, M. Lederer, and D. Kopf, "Optical waveguide writing with a diode-pumped femtosecond oscillator," Opt. Lett. **29**, 1900-1902 (2004).

18. J. Siegel, J. M. Fernandez-Navarro, A. Garcia-Navarro, V. Diez-Blanco, O. Sanz, J. Solis, F. Vega, and J. Armengol, "Waveguide structures in heavy metal oxide glass written with femtosecond laser pulses above the critical self-focusing threshold," Appl. Phys. Lett. **86**, 121109 (2005).

19. D. Grobnic, S. J. Mihailov, C. W. Smelser, F. Genereux, G. Baldenberger, and R. Vallee, "Bragg gratings made in reverse proton exchange lithium niobate waveguides with a femtosecond IR laser and a phase mask," IEEE Photon. Technol. Lett. **17**, 1453-1455 (2005).

20. A. H. Nejadmalayeri, P. R. Herman, J. Burghoff, M. Will, S. Nolte, and A. Tunnermann, "Inscription of optical waveguides in crystalline silicon by mid-infrared femtosecond laser pulses," Opt. Lett. **30**, 964-966 (2005).

21. M. Ams, G. D. Marshall, D. J. Spence, and M. J. Withford, "Slit beam shaping method for femtosecond laser direct-write fabrication of symmetric waveguides in bulk glasses," Opt. Express **13**, 5676-5681 (2005).

22. A. G. Okhrimchuk, A. V. Shestakov, I. Khrushchev, and J. Mitchell, "Depressed cladding, buried waveguide laser formed in a YAG:Nd3+ crystal by femtosecond laser writing," Opt. Lett. **30**, 2248-2250 (2005).

23. R. R. Thomson, S. Campbell, I. J. Blewett, A. K. Kar, D. T. Reid, S. Shen, and A. Jha, "Active waveguide fabrication in erbium-doped oxyfluoride silicate glass using femtosecond pulses," Appl. Phys. Lett. **87**, 121102 (2005).

24. G. Y. Li, K. A. Winick, A. A. Said, M. Dugan, and P. Bado, "Waveguide electro-optic modulator in fused silica fabricated by femtosecond laser direct writing and thermal poling," Opt. Lett. **31**, 739-741 (2006).

25. R. R. Thomson, S. Campbell, I. J. Blewett, A. K. Kar, and D. T. Reid, "Optical waveguide fabrication in z-cut lithium niobate (LiNbO3) using femtosecond pulses in the low repetition rate regime," Appl. Phys. Lett. **88**, 111109 (2006).

26. N. D. Psaila, R. R. Thomson, H. T. Bookey, A. K. Kar, N. Chiodo, R. Osellame, G. Cerullo, G. Brown, A. Jha, and S. Shen, "Femtosecond laser inscription of optical waveguides in bismuth ion doped glass," Opt. Express **14**, 10452-10459 (2006).

27. V. Diez-Blanco, J. Siegel, and J. Solis, "Femtosecond laser writing of optical waveguides with controllable core size in high refractive index glass," Appl. Phys. A: Mater.Sci. Process. **88**, 239-242 (2007).

28. R. R. Thomson, H. T. Bookey, N. D. Psaila, A. Fender, S. Campbell, W. N. MacPherson, J. S. Barton, D. T. Reid, and A. K. Kar, "Ultrafast-laser inscription of a three dimensional fan-out device for multicore fiber coupling applications," Opt. Express **15**, 11691-11697 (2007).

29. S. Campbell, R. R. Thomson, D. P. Hand, A. K. Kar, D. T. Reid, C. Canalias, V. Pasiskevicius, and F. Laurell, "Frequency-doubling in femtosecond laser inscribed periodically-poled potassium titanyl phosphate waveguides," Opt. Express **15**, 17146-17150 (2007).

30. H. T. Bookey, R. R. Thomson, N. D. Psaila, A. K. Kar, N. Chiodo, R. Osellame, and G. Cerullo, "Femtosecond laser inscription of low insertion loss waveguides in Z-cut lithium niobate," IEEE Photon. Technol. Lett. **19**, 892-894 (2007).

31. N. D. Psaila, R. R. Thomson, H. T. Bookey, N. Chiodo, S. Shen, R. Osellame, G. Cerullo, A. Jha, and A. K. Kar, "Er : Yb-doped oxyfluoride silicate glass waveguide laser fabricated using ultrafast laser inscription," IEEE Photonics Technol. Lett. **20**, 126-128 (2008).

32. Y. Li, W. Watanabe, K. Itoh, and X. D. Sun, "Holographic data storage on nonphotosensitive glass with a single femtosecond laser pulse," Appl. Phys. Lett. **81**, 1952-1954 (2002).

33. K. Itoh, W. Watanabe, S. Nolte, and C. B. Schaffer, "Ultrafast processes for bulk modification of transparent materials," Mrs Bulletin **31**, 620-625 (2006).

34. E. N. Glezer, and E. Mazur, "Ultrafast-laser driven micro-explosions in transparent materials," Appl. Phys. Lett. **71**, 882-884 (1997).

35. P. G. Kazansky, H. Inouye, T. Mitsuyu, K. Miura, J. Qiu, K. Hirao, and F. Starrost, "Anomalous anisotropic light scattering in Ge-doped silica glass," Phys. Rev. Lett. **82**, 2199-2202 (1999).

36. L. Sudrie, M. Franco, B. Prade, and A. Mysyrewicz, "Writing of permanent birefringent microlayers in bulk fused silica with femtosecond laser pulses," Opt. Commun. **171**, 279-284 (1999).

37. J. D. Mills, P. G. Kazansky, E. Bricchi, and J. J. Baumberg, "Embedded anisotropic microreflectors by femtosecond-laser nanomachining," Appl. Phys. Lett. **81**, 196-198 (2002).

38. E. Bricchi, J. D. Mills, P. G. Kazansky, B. G. Klappauf, and J. J. Baumberg, "Birefringent Fresnel zone plates in silica fabricated by femtosecond laser machining," Opt. Lett. **27**, 2200-2202 (2002).

39. Y. Shimotsuma, P. G. Kazansky, J. R. Qiu, and K. Hirao, "Self-organized nanogratings in glass irradiated by ultrashort light pulses," Phys. Rev. Lett. **91**, 247405 (2003).

40. E. Bricchi, B. G. Klappauf, and P. G. Kazansky, "Form birefringence and negative index change created by femtosecond direct writing in transparent materials," Opt. Lett. **29**, 119-121 (2004).

41. Y. Shimotsuma, K. Hirao, J. R. Qiu, and P. G. Kazansky, "Nano-modification inside transparent materials by femtosecond laser single beam," Mod. Phys. Lett. B **19**, 225-238 (2005).

42. Y. Shimotsuma, K. Hirao, P. G. Kazansky, and J. R. Qiu, "Three-dimensional micro- and nano-fabrication in transparent materials by femtosecond laser," Japanese Journal of Applied Physics Part 1-Regular Papers Brief Communications & Review Papers **44**, 4735-4748 (2005).

43. C. Hnatovsky, R. S. Taylor, E. Simova, V. R. Bhardwaj, D. M. Rayner, and P. B. Corkum, "High-resolution study of photoinduced modification in fused silica produced by a tightly focused femtosecond laser beam in the presence of aberrations," J. Appl. Phys. **98** (2005).

44. C. Hnatovsky, R. S. Taylor, E. Simova, V. R. Bhardwaj, D. M. Rayner, and P. B. Corkum, "Polarization-selective etching in femtosecond laser-assisted microfluidic channel fabrication in fused silica," Opt. Lett. **30**, 1867-1869 (2005).

45. C. Hnatovsky, R. S. Taylor, P. P. Rajeev, E. Simova, V. R. Bhardwaj, D. M. Rayner, and P. B. Corkum, "Pulse duration dependence of femtosecond-laser-fabricated nanogratings in fused silica," Appl. Phys. Lett. **87**, 014104 (2005).

46. V. R. Bhardwaj, E. Simova, P. B. Corkum, D. M. Rayner, C. Hnatovsky, R. S. Taylor, B. Schreder, M. Kluge, and J. Zimmer, "Femtosecond laser-induced refractive index modification in multicomponent glasses," J. Appl. Phys. **97**, 083102 (2005).

47. E. Bricchi, and P. G. Kazansky, "Extraordinary stability of anisotropic femtosecond direct-written structures embedded in silica glass," Appl. Phys. Lett. **88**, 111119 (2006).

48. W. J. Yang, E. Bricchi, P. G. Kazansky, J. Bovatsek, and A. Y. Arai, "Self-assembled periodic sub-wavelength structures by femtosecond laser direct writing," Opt. Express **14**, 10117-10124 (2006).

49. W. J. Yang, P. G. Kazansky, and Y. P. Svirko, "Non-reciprocal ultrafast laser writing," Nat. Photonics **2**, 99-104 (2008).

50. P. G. Kazansky, W. J. Yang, E. Bricchi, J. Bovatsek, A. Arai, Y. Shimotsuma, K. Miura, and K. Hirao, ""Quill" writing with ultrashort light pulses in transparent materials," Appl. Phys. Lett. **90**, 151120 (2007).

51. K. Yamasaki, S. Juodkazis, M. Watanabe, H. B. Sun, S. Matsuo, and H. Misawa, "Recording by microexplosion and two-photon reading of three-dimensional optical memory in polymethylmethacrylate films," Appl. Phys. Lett. **76**, 1000-1002 (2000).

52. H. B. Sun, Y. Xu, S. Juodkazis, K. Sun, M. Watanabe, S. Matsuo, H. Misawa, and J. Nishii, "Arbitrary-lattice photonic crystals created by multiphoton microfabrication," Opt. Lett. **26**, 325-327 (2001).

53. V. R. Bhardwaj, E. Simova, P. P. Rajeev, C. Hnatovsky, R. S. Taylor, D. M. Rayner, and P. B. Corkum, "Optically produced arrays of planar nanostructures inside fused silica," Phys. Rev. Lett. **96**, 16486984 (2006).

54. C. Hnatovsky, R. S. Taylor, E. Simova, P. P. Rajeev, D. M. Rayner, V. R. Bhardwaj, and P. B. Corkum, "Fabrication of microchannels in glass using focused femtosecond laser radiation and selective chemical etching," Appl. Phys. A: Mater.Sci. Process. **84**, 47-61 (2006).

55. R. S. Taylor, C. Hnatovsky, E. Simova, P. P. Rajeev, D. M. Rayner, and P. B. Corkurn, "Femtosecond laser erasing and rewriting of self-organized planar nanocracks in fused silica glass," Opt. Lett. **32**, 2888-2890 (2007).

56. M. Watanabe, S. Juodkazis, J. Nishii, S. Matsuo, and H. Misawa, "Microfabrication by a high fluence femtosecond exposure: Mechanism and applications," in *SPIE*(2002), pp. 159-168.

57. V. Mizeikis, K. K. Seet, S. Juodkazis, and H. Misawa, "Three-dimensional woodpile photonic crystal templates for the infrared spectral range," Opt. Lett. **29**, 2061-2063 (2004).

58. S. Matsuo, S. Juodkazis, and H. Misawa, "Femtosecond laser microfabrication of periodic structures using a microlens array," Appl. Phys. A: Mater.Sci. Process. **80**, 683-685 (2005).

59. K. K. Seet, V. Mizeikis, S. Matsuo, S. Juodkazis, and H. Misawa, "Three-dimensional spiral-architecture photonic crystals obtained by direct laser writing," Adv. Mater. **17**, 541-545 (2005).

60. S. Juodkazis, H. Misawa, O. A. Louchev, and K. Kitamura, "Femtosecond laser ablation of chalcogenide glass: explosive formation of nano-fibres against thermo-capillary growth of micro-spheres," Nanotechnology **17**, 4802-4805 (2006).

61. T. Kondo, S. Juodkazis, V. Mizeikis, S. Matsuo, and H. Misawa, "Fabrication of three-dimensional periodic microstructures in photoresist SU-8 by phase-controlled holographic lithography," New J. Phys. **8**, 250 (2006).

62. S. Juodkazis, M. Sudzius, V. Mizeikis, H. Misawa, E. G. Gamaly, Y. W. Liu, O. A. Louchev, and K. Kitamura, "Three-dimensional recording by tightly focused femtosecond pulses in LiNbO3," Appl. Phys. Lett. **89**, 062903 (2006).

63. E. G. Gamaly, S. Juodkazis, K. Nishimura, H. Misawa, and B. Luther-Davies, "Laser-matter interaction in the bulk of a transparent solid: Confined microexplosion and void formation," Phys. Rev. B. **73**, 214101 (2006).

64. S. Juodkazis, H. Misawa, T. Hashimoto, E. G. Gamaly, and B. Luther-Davies, "Laser-induced microexplosion confined in a bulk of silica: Formation of nanovoids," Appl. Phys. Lett. **88**, 201909 (2006).

65. T. Hashimoto, S. Juodkazis, and H. Misawa, "Void recording in silica," Appl. Phys. A: Mater.Sci. Process. **83**, 337-340 (2006).

66. S. Juodkazis, K. Nishimura, S. Tanaka, H. Misawa, E. G. Gamaly, B. Luther-Davies, L. Hallo, P. Nicolai, and V. T. Tikhonchuk, "Laser-induced microexplosion confined in the bulk of a sapphire crystal: Evidence of multimegabar pressures," Phys. Rev. Lett. **96**, 166101 (2006).

67. N. D. Psaila, R. R. Thomson, H. T. Bookey, S. X. Shen, N. Chiodo, R. Osellame, G. Cerullo, A. Jha, and A. K. Kar, "Supercontinuum generation in an ultrafast laser inscribed chalcogenide glass waveguide," Opt. Express **15**, 15776-15781 (2007).

68. A. S. L. Gomes, E. L. Falcao, C. B. de Araujo, D. Rativa, R. E. de Araujo, K. Sakaguchi, F. P. Mezzapesa, I. C. S. Carvalho, and P. G. Kazansky, "Third-order nonlinear optical properties of bismuth-borate glasses measured by conventional and thermally managed eclipse Z scan," J. Appl. Phys. **101**, 033115 (2007).

69. O. Deparis, F. P. Mezzapesa, C. Corbari, P. G. Kazansky, and K. Sakaguchi, "Origin and enhancement of the second-order non-linear optical susceptibility induced in bismuth borate glasses by thermal poling," J. Non-Cryst. Solids **351**, 2166-2177 (2005).

70. K. Tanaka, M. Notani, and H. Hisakuni, "Optical Anisotropy in As2s3 Glass Induced with Sub-Bandgap Illumination," Solid State Commun. **95**, 461-464 (1995).

71. P. Krecmer, A. M. Moulin, R. J. Stephenson, T. Rayment, M. E. Welland, and S. R. Elliott, "Reversible nanocontraction and dilatation in a solid induced by polarized light," Science **277**, 1799-1802 (1997).

72. R. W. Boyd, *Nonlinear Optics* (Academic Press, 2003).

73. A. L. Gaeta, "Catastrophic collapse of ultrashort pulses," Phys. Rev. Lett. **84**, 3582-3585 (2000).

74. C. B. Schaffer, A. Brodeur, and E. Mazur, "Laser-induced breakdown and damage in bulk transparent materials induced by tightly focused femtosecond laser pulses," Meas. Sci. Technol. **12**, 1784-1794 (2001).

75. L.V.Keldysh, "Quantum transport equations for high electric fields," SOV. PHYS. JETP **20**, 1307 (1965).

76. Yablonov.E, and Bloember.N, "Avalanche Ionization and Limiting Diameter of Filaments Induced by Light-Pulses in Transparent Media," Phys. Rev. Lett. **29**, 907-& (1972).

77. R. Osellame, S. Taccheo, M. Marangoni, R. Ramponi, P. Laporta, D. Polli, S. De Silvestri, and G. Cerullo, "Femtosecond writing of active optical waveguides with astigmatically shaped beams," J. Opt. Soc. Am. B-Opt. Phys. **20**, 1559-1567 (2003).

78. R. R. Thomson, A. S. Bockelt, E. Ramsay, S. Beecher, A. H. Greenaway, A. K. Kar, and D. T. Reid, "Shaping ultrafast laser inscribed optical waveguides using a deformable mirror," Opt. Express **16**, 12786-12793 (2008).

79. P. Oberson, B. Gisin, B. Huttner, and N. Gisin, "Refracted near-field measurements of refractive index and geometry of silica-on-silicon integrated optical waveguides," Appl. Opt. **37**, 7268-7272 (1998).

80. C. Joenathan, "Phase-Measuring Interferometry - New Methods and Error Analysis," Appl. Opt. **33**, 4147-4155 (1994).

81. F. Charriere, J. Kuhn, T. Colomb, F. Montfort, E. Cuche, Y. Emery, K. Weible, P. Marquet, and C. Depeursinge, "Characterization of microlenses by digital holographic microscopy," Appl. Opt. **45**, 829-835 (2006).

82. N. Axelrod, A. Radko, A. Lewis, and N. Ben-Yosef, "Topographic profiling and refractive-index analysis by use of differential interference contrast with bright-field intensity and atomic force imaging," Appl. Opt. **43**, 2272-2284 (2004).

83. A. Barty, K. A. Nugent, D. Paganin, and A. Roberts, "Quantitative optical phase microscopy," Opt. Lett. **23**, 817-819 (1998).

84. D. Paganin, and K. A. Nugent, "Noninterferometric phase imaging with partially coherent light," Phys. Rev. Lett. **80**, 2586-2589 (1998).

85. R. Oldenbourg, E. D. Salmon, and P. T. Tran, "Birefringence of single and bundled microtubules," Biophys. J. **74**, 645-654 (1998).

86. M. Shribak, and R. Oldenbourg, "Techniques for fast and sensitive measurements of two-dimensional birefringence distributions," Appl. Opt. **42**, 3009-3017 (2003).

87. Y. Sikorski, A. A. Said, P. Bado, R. Maynard, C. Florea, and K. A. Winick, "Optical waveguide amplifier in Nd-doped glass written with near-IR femtosecond laser pulses," Electron. Lett. **36**, 226-227 (2000).

88. J. W. Chan, T. R. Huser, S. H. Risbud, and D. M. Krol, "Modification of the fused silica glass network associated with waveguide fabrication using femtosecond laser pulses," Appl. Phys. A **76**, 367-372 (2003).

89. S. M. Eaton, H. B. Zhang, and P. R. Herman, "Heat accumulation effects in femtosecond laser-written waveguides with variable repetition rate," Opt. Express **13**, 4708-4716 (2005).

90. R. R. Thomson, H. T. Bookey, N. Psaila, S. Campbell, D. T. Reid, S. X. Shen, A. Jha, and A. K. Kar, "Internal gain from an erbium-doped oxyfluoride-silicate glass waveguide fabricated using femtosecond waveguide inscription," IEEE Photonics Technol. Lett. **18**, 1515-1517 (2006).

91. N. D. Psaila, R. R. Thomson, H. T. Bookey, A. K. Kar, N. Chiodo, R. Osellame, G. Cerullo, A. Jha, and S. Shen, "Er:Yb-doped oxyfluoride silicate glass waveguide amplifier fabricated using femtosecond laser inscription," Appl. Phys. Lett. **90**, 131102 (2007).

92. G. Tittelbach, B. Richter, and W. karthe, "Comparison of three transmission methods for integrated optical waveguide propagation loss measurement," Pure Appl. Opt. **2**, 683-706 (1993).

93. G. Agrawal, "Nonlinear Fiber Optics," (Third edition, Academic Press, 2001).

94. F. P. Mezzapesa, I. C. S. Carvalho, C. Corbari, P. G. Kazansky, J. S. Wilkinson, and G. Chen, "Voltage-assisted cooling: a new route to enhance Chi((2)) during thermal poling," CLEO (2005).

95. C. J. Marckmann, Y. T. Ren, G. Genty, and M. Kristensen, "Strength and symmetry of the third-order nonlinearity during poling of glass waveguides," IEEE Photon. Technol. Lett. **14**, 1294-1296 (2002).

96. S. M. Eaton, H. Zhang, M. L. Ng, J. Z. Li, W. J. Chen, S. Ho, and P. R. Herman, "Transition from thermal diffusion to heat accumulation in high repetition rate femtosecond laser writing of buried optical waveguides," Opt. Express **16**, 9443-9458 (2008).

97. C. B. Schaffer, J. F. Garcia, and E. Mazur, "Bulk heating of transparent materials using a high-repetition-rate femtosecond laser," Appl. Phys. A: Mater.Sci. Process. **76**, 351-354 (2003).

98. S. Akturk, M. Kimmel, P. O'Shea, and R. Trebino, "Measuring pulse-front tilt in ultrashort pulses using GRENOUILLE," Opt. Express **11**, 491-501 (2003).

99. W. L. Kruer, "The Physics of Laser Plasma Interactions," (Addison-Wesley, 1988).

100. W. Yu, V. Bychenkov, Y. Sentoku, M. Y. Yu, Z. M. Sheng, and K. Mima, "Electron acceleration by a short relativistic laser pulse at the front of solid targets," Phys. Rev. Lett. **85**, 570-573 (2000).

101. M. Ashourabdalla, J. N. Leboeuf, T. Tajima, J. M. Dawson, and C. F. Kennel, "Ultra-Relativistic Electromagnetic Pulses in Plasmas," Phys. Rev. A **23**, 1906-1914 (1981).

102. F. V. Bunkin, and M. V. Fedorov, "Bremsstrahlung in a Strong Radiation Field," Soviet Physics JETP **22**, 844 (1966).

103. W. Watanabe, and K. Itoh, "Motion of bubble in solid by femtosecond laser pulses," Opt. Express **10**, 603-608 (2002).

104. A. Vogel, J. Noack, G. Huttman, and G. Paltauf, "Mechanisms of femtosecond laser nanosurgery of cells and tissues," Appl. Phys. B: Lasers Opt. **81**, 1015-1047 (2005).

105. D. W. Hewak, J. A. M. Neto, B. Samson, R. S. Brown, K. P. Jedrzejewski, J. Wang, E. Taylor, R. I. Laming, G. Wylangowski, and D. N. Payne, "Quantum-Efficiency of Praseodymium Doped Galas Glass for 1.3 Mu-M Optical-Fiber Amplifiers," IEEE Photon. Technol. Lett. **6**, 609-612 (1994).

106. M. Asobe, T. Ohara, I. Yokohama, and T. Kaino, "Low power all-optical switching in a nonlinear optical loop mirror using chalcogenide glass fibre," Electron. Lett. **32**, 1396-1397 (1996).

107. J. S. Sanghera, and I. D. Aggarwal, "Active and passive chalcogenide glass optical fibers for IR applications: a review," J. Non-Cryst. Solids **257**, 6-16 (1999).

108. H. Takebe, R. Kitagawa, and D. W. Hewak, "Non-toxic sulfide glasses and thin films for optical applications," J. Ceram. Soc. Jpn. **113**, 37-43 (2005).

109. S. R. Elliott, *Chalcogenide glasses* (VCH: New York, 1991).

110. A. Zakery, and S. R. Elliott, "Optical properties and applications of chalcogenide glasses: a review," J. Non-Cryst. Solids **330**, 1-12 (2003).

111. V. K. Tikhomirov, and S. R. Elliott, "Model for Photoinduced Anisotropy and Its Dark Relaxation in Chalcogenide Glasses," Phys. Rev. B. **51**, 5538-5541 (1995).

112. S. R. Elliott, and V. K. Tikhomirov, "Vectoral and scalar photoinduced effects in chalcogenide glasses," J. Non-Cryst. Solids **200**, 669-674 (1996).

113. V. Lyubin, M. Klebanov, M. Mitkova, and T. Petkova, "Polarization-dependent, laser-induced anisotropic photocrystallization of some amorphous chalcogenide films," Appl. Phys. Lett. **71**, 2118-2120 (1997).

114. V. Lyubin, and M. Klebanov, "Interaction of polarized light with chalcogenide glasses," Journal of Optoelectronics and Advanced Materials **3**, 265-277 (2001).

115. V. M. Kryshenik, and V. I. Mikla, "Anisotropic phenomena in as-evaporated amorphous chalcogenide thin films," Materials Science and Engineering B-Solid State Materials for Advanced Technology **100**, 292-296 (2003).

116. www.moebius.physik.tu-berlin.de/lc/lcd.html.

117. R. S. Weis, and T. K. Gaylord, "Lithium niobate: summary of physical properties and crystal structure," Appl. Phys. A **37**, 191-203 (1985).

118. A. M. Prokhorov, and Y. S. Kuzminov, "Physics and Chemistry of Crystalline Lithium Niobate," (Nature Publishing Group, 1990).

119. V. Y. Shur, "Nanoscale backswitched domain patterning in lithium niobate," Appl. Phys. Lett. **76**, 143-145 (2000).

120. K. Gallo, G. Assanto, K. R. Parameswaran, and M. M. Fejer, "All-optical diode in a periodically poled lithium niobate waveguide," Appl. Phys. Lett. **79**, 314-316 (2001).

121. L. Gui, B. X. Xu, and T. C. Chong, "Microstructure in lithium niobate by use of focused femtosecond laser pulses," IEEE Photon. Technol. Lett. **16**, 1337-1339 (2004).

122. H. T. Hsieh, D. Psaltis, O. Beyer, D. Maxein, C. von Korff Schmising, K. Buse, and B. Sturman, "Femtosecond holography in lithium niobate crystals," Opt. Lett. **30**, 2233-2235 (2005).

123. G. Y. Zhou, and M. Gu, "Anisotropic properties of ultrafast laser-driven microexplosions in lithium niobate crystal," Appl. Phys. Lett. **87**, 241107 (2005).

124. O. Beyer, I. Breunig, F. Kalkum, and K. Buse, "Photorefractive effect in iron-doped lithium niobate crystals induced by femtosecond pulses of 1.5 um wavelength," Appl. Phys. Lett. **88**, 051120 (2006).

125. G. Y. Zhou, and M. Gu, "Direct optical fabrication of three-dimensional photonic crystals in a high refractive index LiNbO3 crystal," Opt. Lett. **31**, 2783-2785 (2006).

126. J. Burghoff, C. Grebing, S. Nolte, and A. Tunnermann, "Waveguides in lithium niobate fabricated by focused ultrashort laser pulses," Appl. Surf. Sci. **253**, 7899-7902 (2007).

127. A. H. Nejadmalayeri, and P. R. Herman, "Rapid thermal annealing in high repetition rate ultrafast laser waveguide writing in lithium niobate," Opt. Express **15**, 10842-10854 (2007).

128. R. Osellame, M. Lobino, N. Chiodo, M. Marangoni, G. Cerullo, R. Ramponi, H. T. Bookey, R. R. Thomson, N. D. Psaila, and A. K. Kar, "Femtosecond laser writing of waveguides in periodically poled lithium niobate preserving the nonlinear coefficient," Appl. Phys. Lett. **90**, 241107 (2007).

129. A. Yuse, and M. Sano, "Transition between Crack Patterns in Quenched Glass Plates," Nature **362**, 329-331 (1993).

130. R. D. Deegan, P. J. Petersan, M. Marder, and H. L. Swinney, "Oscillating fracture paths in rubber," Phys. Rev. Lett. **88**, 016152 (2002).

131. B. Sturman, and V. M. Fridkin, "The Photovoltaic and Photorefractive Effects in Noncentrosymmetric Materials," (Nature Publishing Group, 1992).

132. E. L. Ivchenko, and G. E. Pikus, "Superlattices and Other Heterostructures: Symmetry and Optical Phenomena," (Nature Publishing Group, 1995).

133. G. Rikken, and E. Raupach, "Observation of magneto-chiral dichroism," Nature **390**, 493-494 (1997).